IMPERIAL COLLEGE LONDON
UNIVERSITY OF LONDON

RAIL INSPECTION USING ULTRASONIC SURFACE WAVES

by

Daniel Hesse

A thesis submitted to the University of London for the degree of
Doctor of Philosophy

Department of Mechanical Engineering
Imperial College London
London SW7 2AZ

March 2007

Abstract

The detection of critical surface cracks in the railhead is a major challenge for the railway industry. Conventional inspection methods have proven not to be reliable enough in this context, therefore the aim of this work was to develop an alternative or complementary screening method. The approach was to scan a pulse-echo probe along the rail which deploys low frequency surface waves.

The results of an initial study on plates with about the thickness of a railhead were encouraging, even though the interference of multiple guided wave modes complicated the signal interpretation.

The properties of the dominant surface wave modes of rails were determined and a mode suitable for inspection purposes was identified. However, it was found that there was a number of similar unwanted modes which would be easily excitable from the railhead surface as well.

In order to ensure correct and reliable signal interpretation it was necessary to suppress such unwanted modes. Two signal processing methods were developed, one involving focussing of a phased array across the railhead, the second mimicking an increased probe length along the rail by a spatial averaging method. The latter was found to be highly effective and robust, rendering the phased array obsolete and thus reducing both system complexity and data acquisition time.

The performance of this method was studied on rail specimens containing artificial and real defects. Areas with defects were reliably distinguished from areas without defects or with tolerable surface damage. Furthermore, deep defects were detected even with multiple smaller ones in front. However, due the complex geometry of real cracks and the interference of reflections from multiple defects, accurate sizing appeared to be very difficult. Nevertheless, the inspection method developed appears suitable for defect detection and could be used to complement existing methods and thus enhance their reliability.

Acknowledgements

I would like to sincerely thank my supervisors Prof. Peter Cawley and Dr. Mike Lowe for their excellent guidance, helpful discussions and support. I am very grateful for having been given the opportunity to work in their NDT research group and have enjoyed the truly stimulating environment.

A special thanks to all my colleagues (and former colleagues) which have contributed with their help and advice, for example Dr. Francesco Simonetti, Dr. Frédéric Cegla, Dr. Jimmy Fong, Dr. Thomas Vogt, Dr. Mark Evans (thanks also for the specimens) and many others. I also would like to thank Dr. Andreas Kronenburg for introducing me to the NDT group in March 2002.

Furthermore, I am grateful to the people at Corus, for providing me with rail specimens, and at ESR Ltd. as well as the Health & Safety Executive for helping me with measurements on their rail samples.

Finally, I would like to thank my parents and my sister Inga for their encouragement and reassuring support.

Contents

Appendices

List of Figures

Nomenclature

A	amplitude
B	transmitter sensitivity
c	bulk velocity
c_g	group velocity
c_p	phase velocity
C	contact function
C_r	spectral reflection coefficient
$\tilde{C}_r$	finite bandwidth reflection ratio
$\mathbf{c}$	stiffness tensor
d	defect depth
D	function combining mode excitability and interaction with features
E	Young's modulus
$\tilde{E}$	excitability
f	frequency
G	send-receive sensitivity
H	term in send-receive sensitivity containing DSFT of the contact function
k	wavenumber
l	distance
L	transducer length
n, N	index, counter
p	pressure (spatial domain)
P	pressure (wavenumber domain)
P_{AV}	average power in waveguide
R	received signal
$\bar{R}$	spatially averaged received signal
S	transducer surface
$\mathbf{S}$	strain tensor
t	time

continue on next page

continue from previous page

u	displacement
$\mathbf{u}$	displacement distribution/mode shape
u_S	average strain energy density
U	voltage
$\bar{U}$	spatially averaged voltage
w	window/weighting function
Δx	probe spacing
x, y, z	cartesian coordinates

Greek letters:

λ	wavelength
ν	Poisson's ratio
ρ	density
φ	angle of wedge probe
Φ	phase shift
Θ	angle of inclined defect
ω	angular frequency

Subscripts:

$_l$	refers to longitudinal waves
$_n$	probe position index
$_{PA}$	refers to full phased array
$_{rn}$	probe receive position, index n
$_R$	refers to Rayleigh waves
$_s$	refers to shear waves
$_{sn}$	probe send position, index n
$_w$	denotes water

Chapter 1

Introduction

1.1 Defects in rails

Fatigue defects in rails can lead to rail breaks and are therefore a potential hazard for railway safety. According to their initiation, they can be divided into three broad groups [1]:

- Cracks caused by manufacturing defects, e.g. *tache ovales* (mainly in bad welds due to hydrogen inclusions [2]).
- Defects due to inappropriate handling and use, e.g. surface spalling caused by *wheelburn* (spinning wheels).
- Rolling contact fatigue (RCF) defects, like sub-surface initiated *shells* or surface-initiated *squats* and *head checking.*

Depending on the mechanical loading conditions and the fatigue life of the rail, flaws may develop into transverse cracks which can lead to rail breaks [3]. In the US during 1993-95, rail head and transverse defects in the rail represented about 40% of the causes of train derailments (transverse defects alone 29%) and 51% of the total costs [4]; in the UK 39.5% of rail breaks were caused by vertical/transverse defects [5].

Improved manufacturing technology has reduced the number of fatigue crack initiation sites inside the rail, i.e. the number of defects in the first group above has decreased. However, changing service demands like increased average load, higher train speeds, shorter inspection windows [4] and higher wear resistance have resulted in new problems; new rail steels are of such high quality and are so resistant to abrasion that material wear is no longer sufficient to prevent the growth of cracks in the rail surface [6]. Therefore, over the last 20 years, the number of rail failures due to RCF defects has been increasing (e.g. the Hatfield accident in the UK in 2000) and is now a major concern of the railroad industry [1]. In the late 1990s, RCF defects accounted for about 60% of defects found by East Japan Railways, 25% in France (SNCF) and 15% in the UK [1]. Due to inconsistencies in the categorisation and reporting of defects for a number of years, these statistics are likely to underestimate the real figures in the UK [7]. RCF is likely to be a major future concern as speed, axle load, traffic density and tractive forces will continue to increase [2].

RCF defects are caused by high normal and tangential stresses which lead to severe shearing of the surface layer of the rail. The crack produced propagates through the heavily deformed surface layer at a shallow angle to the running surface until it reaches a depth of approximately 5 mm [3, 7–10] where the material has remained undeformed [1]. From there, it can develop branches that either turn up and cause spalling at the rail surface or turn downwards. The exact reasons for the branching are still not clearly understood [1, 11], but may include the action of longitudinal stresses in the rail head. These stresses, whilst compressive at the surface, change to tensile towards the centre of the rail head [11]. If the downward branches remain undetected they can eventually grow in the zone of influence of the gross longitudinal bending and residual stresses in the body of the rail and propagate to cause complete rail fracture [11].

RCF defects can be further distinguished into subcategories, the two most important of which are *squats* and *head checks*. *Squats* are defects which occur in straight or slightly curved track on relatively high speed passenger lines. They are visible as dark areas on the rail surface because of subsurface cracking which causes surface

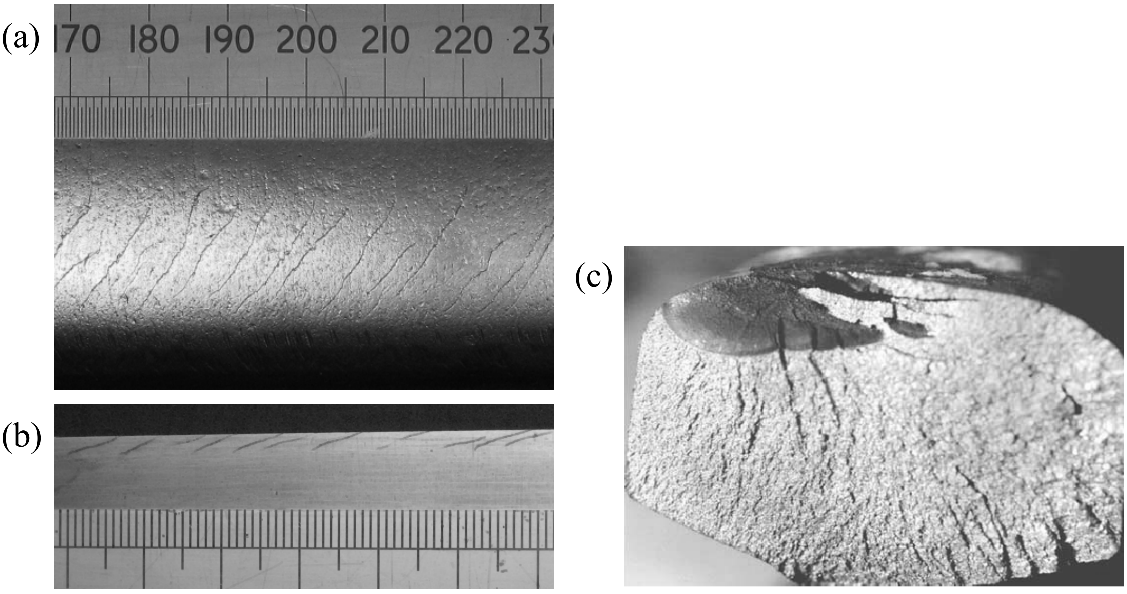

Figure 1.1: *(a) Gauge corner cracking or head checks (scale in mm). (b) Longitudinal section of rail specimen in Figure 1.1a on same scale. (c) Rail failure resulting from gauge corner cracking [11].*

depression and accumulation of wear debris. Each squat typically consists of two cracks growing at inclined angles: a leading one which propagates in the direction of travel and a trailing crack which propagates faster in the opposite direction. Authors of publications on this subject disagree about the angles; cited values are between 10-15° [3] and 30° [2]). The trailing crack is typically several times longer than the leading crack (20 to 50 mm) and contains numerous minute branches, one of which may propagate transversely across the rail head and lead to rail failure [2].

The terms *head checks* and *gauge corner cracking* (GCC) are commonly used interchangeably and refer to clusters of fine cracks between the crown and the gauge corner of the rail with a spacing between 0.5 and 7 mm [3, 6]. (Note that the term GCC is occasionally used specifically for RCF within 10 mm from the gauge face and head checks for RCF further towards the crown [7].) These defects grow at an acute angle into the rail following the dominant traffic direction. The angles given in the literature vary, typically cited values are 10 to 15° [3] and 15 to 20° [10]. Figure 1.1a shows a top view of a rail head containing GCC. The longitudinal section in Figure 1.1b of the same specimen shows the typical crack orientation; the traffic direction in this case would have been from the right to the left. There may be thousands of such fine surface head checks on the high rail of some curves, and deep transverse defects may extend from a few of them [1]. An example of a rail break caused by GCC is shown in Figure 1.1c. Head checks are the dominant type of RCF defects in the British rail network [7] and were for example the cause of the Hatfield rail accident [12].

The early stages of rolling contact fatigue can be managed to some extent by regular track grinding which removes defects at the initiation stage. On the other hand, small cracks are unlikely to cause rail failure in the short term and are therefore considered to be tolerable if their depth is less than approximately 5 mm [12, 13]. The railway industry is interested in a cost effective balance between rail grinding, defect monitoring and rail replacement while still ensuring track safety. In order to achieve this, reliable and efficient non-destructive methods are needed to assess the severity of defects.

1.2 Rail inspection

1.2.1 Standard methods

The first inspection cars for non-destructive testing of railroads were introduced in 1923 by Sperry and utilised a magnetic flux leakage technique to detect defects [4, 14]. Its basic principle is that a high current is injected into the rail via contact brushes, thus making the rail effectively part of an electric circuit. Defects will distort the current flow and the magnetic field induced by it, and the flux leakage can be picked up with search coils. This method has many shortcomings, e.g. in detecting defects which are not transverse to flux lines and close to the search coils, but it is still used in Russia and in the USA as a complementary testing technique [14].

Ultrasonic testing was first implemented in inspection cars in the 1950s and has become the most commonly used rail inspection method [14]. Nowadays, ultrasonic

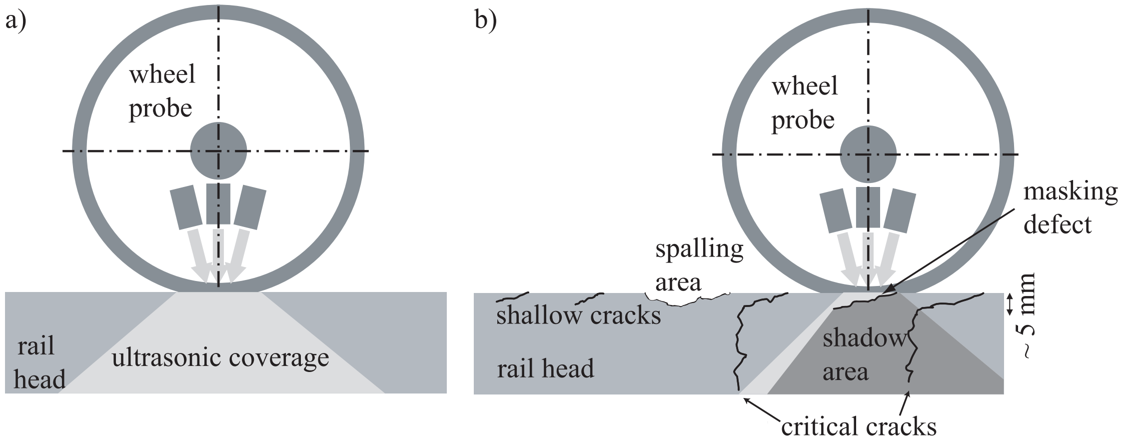

Figure 1.2: *Conventional ultrasonic wheel probe: a) Theoretical coverage from a single inspection position, b) Masking of critical transverse cracks by shallow surface cracks.*

inspection units can be mounted on trains, road-rail vehicles ('hi-rail vehicles') or manual 'walking sticks'. They send a number of ultrasonic beams into the rail and measure amplitude and arrival time of reflected signals to assess the integrity of the rail. Wheel probes have proven to be more reliable than slider probes, since they are robust and able to conform to the rail. For both types of probe an oil- or water-based coupling fluid is necessary. The probes contain up to nine transducers (normally run in pulse-echo mode [4] at a typical centre frequency of 2.25 MHz [14]) and send bulk waves at different angles into the rail. A typical configuration involves transmission at 0°, 45° (forward and reverse) and 70° (forward and reverse) as well as a "side looker" transducer to cover the gauge corner [4].

Theoretically, ultrasonic testing cars can operate at relatively high speeds in the range of 40-70 km/h [4,8], new generation vehicles even up to 100 km/h [1]. However, a high percentage of defect indications (70% to 80%), is proven false after hand-test verifications [4]. The vehicle is therefore usually stopped at each indication for manual confirmation which can reduce the average speed to 6 to 8 mph [4]. Furthermore, conventional ultrasonic methods cannot reliably detect critical defects masked by spalled rail or shallow defects [4]. Figure 1.2a illustrates the volume of rail theoretically covered by a conventional ultrasonic probe. Surface damage preventing ultrasound from propagating into the railhead and shallow defects reflecting the signals can cause 'shadow zones' in which downward branches of critical defects cannot be detected [1, 2], see Figure 1.2b. There have been many cases where such defects remained completely undetected by ultrasonic inspection and eventually caused rail breaks and derailments [4]. Considering the increasing significance of RCF defects, this lack of reliability is a major issue.

Eddy current systems are very sensitive to surface defects and therefore appear more suitable in the context of RCF defects. These train mounted units use coils to induce eddy currents in the surface of the rail and measure impedance changes caused by surface cracks like head checks. However, eddy current measurements give an indication for the length of a defect rather than its depth. This means that consistent crack growth at a fixed angle has to be assumed (e.g. 23° for head checks in [6]) to estimate the crack depth. Another issue is that eddy currents have a very limited penetration depth. This means that it might be difficult to correctly determine the full depth of a defect, especially if the density of features at the surface, such as small RCF cracks or other damage, is very high. Such a system appears therefore to be useful for assessing whether a rail grinding operation has removed cracks in the rail surface [6], but it appears to be less suitable as a quick screening tool to pick up critical defects.

Some railway companies use radiography for examining alumino-thermic welds and defects with orientations unsuitable for ultrasonic inspection [1]. Other very basic inspection methods include dye penetrant and magnetic particle methods as well as visual inspection [1, 8].

On the British rail network visual inspection is still the main method to assess the severity of gauge corner cracking [15]. Even though there exists an ultrasonic procedure U14 "Detection and Sizing of Gauge Corner Cracking", this is only applied to quantify the extent of the cracking when GCC has been detected visually [12]. That procedure uses the standard ultrasonic testing equipment, but with the probe being offset towards the gauge corner of the rail, which means that a location could still be "untestable" due to masking as discussed above. To classify defect severity entirely by visual inspection the longest visible defect path on the surface is measured. It was found that there is a very rough correlation between the length of an

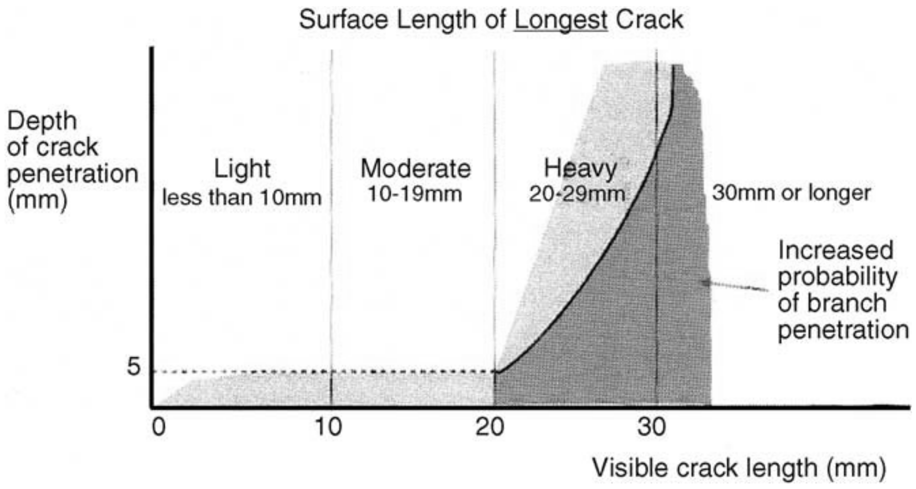

Figure 1.3: *Correlation of crack penetration with visible crack length (from Reference [7]).*

individual crack on the rail surface and its depth of penetration into the rail. If a defect is longer than about 20 mm, there is a significant possibility that the crack has turned down and reached a critical depth, see the chart in Figure 1.3 [7]. Since this approach is crude and time consuming, there is clearly a need for an improved automated testing method.

1.2.2 Recent developments and research

The shortcomings of the existing rail inspection methods have led to a variety of research projects which address specific issues and are aimed at complementing the existing techniques.

In order to improve for example the detection of vertical defects propagating in the longitudinal direction (along the rail) several ultrasonic transmission techniques that are applied across the railhead have been investigated [16–20]. Vertical longitudinal as well as transverse defects are addressed by a method utilising laser sources to excite bulk waves on the side of the rail head to detect defects by ultrasonic shadowing [21, 22]. All these approaches need access from the side of the railhead which in reality is often obscured by switch blades, fasteners etc. For this reason their integration into an inspection train would be difficult.

In recent years there has been a lot of research into long range guided waves applied to rail inspection, see for example [23–26]. Utilising the wave guide characteristics of the rail, these methods are well suited to detect critical transverse defects which obscure the wave path. A difficult issue is wave mode control which is why most approaches rely on transducers which are fixed on the rail. A portable system has been developed in the UK which has to be clamped onto the rail and is able to inspect the whole cross section of the rail (including the foot) for a length of many tens of metres [23]. The system delivers very promising results in critical locations such as level crossings or tunnels. However, since it cannot be train mounted, it would not be suitable for the quick inspection of long distances in order to cover the full rail network.

A very promising candidate to overcome the issues of conventional ultrasonic systems regarding the detection of RCF defects in the railhead is the use of surface waves propagating along the rail. They combine some advantages of guided waves, such as a larger coverage from a single inspection position, with the potential of integration into a moving hand-held or train mounted inspection system. The work presented in this thesis and the arising publications focus on this approach, as does research elsewhere [18–20, 27–30].

1.3 Project aim

The aim of this work was to develop an inspection method that could reliably detect critical transverse defects in the railhead. The method should be a very robust screening tool and perform well even on surfaces containing RCF or other surface damage. Precise sizing was considered less important as long as critical defects could be picked up. Furthermore, it should be easy to integrate into existing inspection setups to simplify field testing and further development stages. Since the concept of using surface waves appeared to be most promising it was decided to focus on this. A crucial part of the overall aim was therefore to gain a better understanding of the characteristics of surface waves in rails and what implications they have for the detection and sizing of defects.

1.4 Outline of thesis

The structure of this thesis broadly follows the actual order of research undertaken for this project.

Chapter 2 provides background information on surface waves applied to non-destructive testing in general and rail testing in particular. Based on this, some basic considerations regarding probe requirements are made. The approach taken in this work is defined and put into context.

An initial investigation applying surface wave inspection to steel plates with the thickness of a railhead is presented in Chapter 3. This study served as a trial for the chosen approach on a less complex wave guide geometry. Experimental results as well as simulations using the finite element method (FEM) are discussed and potential problem areas are identified.

Dispersion curves and mode shapes of surface waves modes in rails are determined in Chapter 4. A mode suitable for inspection purposes is identified and the problem of the concurrent presence of multiple modes is discussed.

In Chapter 5, two approaches are examined for an efficient excitation of the selected surface wave mode in rails. The first makes use of a transducer array across the width of the rail and utilises array focussing to match the mode shape in the area of the probe contact patch. The second approach is a spatial averaging technique which exploits the signal redundancy of the data obtained from scanning the probe along the rail. The potential and limitations of both methods is discussed in detail and a procedure for experiments is derived.

Experimental results from a number of rail specimens containing both artificial defects and real RCF cracks are presented in Chapter 6. The feasibility of detecting and sizing of critical defects is discussed.

Chapter 7 summarises the findings in this thesis and draws conclusions, which lead to suggestions for future work.

Chapter 2

Literature review and initial considerations

2.1 Background on surface waves

An extensive amount of literature has been published on surface waves in solids. This section will only give an overview of selected references relevant for the use of surface waves in non-destructive testing (NDT) applications and more specifically in the context of rail testing.

2.1.1 Surface waves for NDT applications

In 1885, Lord Rayleigh showed that waves can be propagated over the free surface of an elastic half-space [31]. He found that these surface waves ("Rayleigh waves") are confined to a superficial region of a thickness comparable with the wavelength and that they decay exponentially with depth. Figure 2.1 shows the associated displacement profiles in the in-plane and out-of-plane directions. Rayleigh described these surface waves as analogous to deep-water waves and already suggested their importance during earthquakes: since they diverge only in two dimensions, they are less attenuated than bulk waves and propagate over a longer distance.

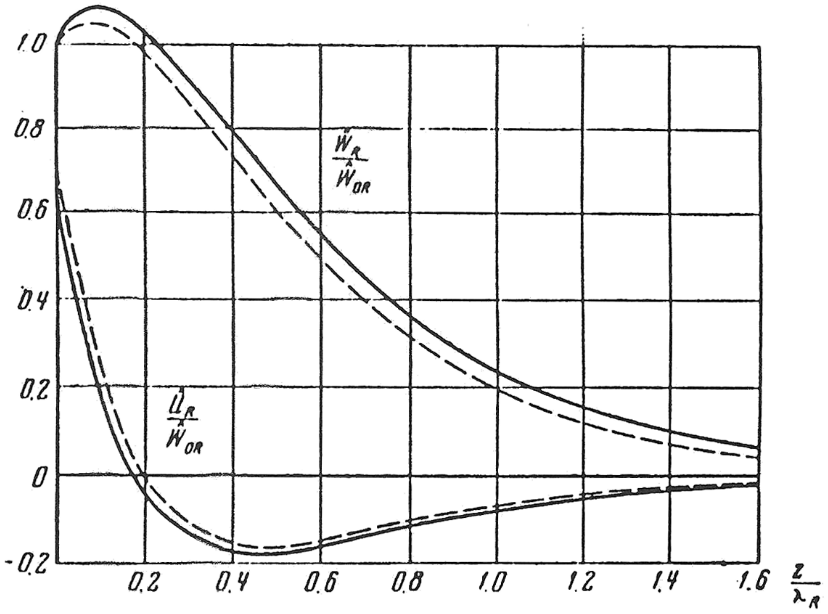

Figure 2.1: *Normalised displacement amplitudes in-plane (U_R) and out-of-plane (W_R) of a Rayleigh wave as a function of depth z from the surface (normalised to wavelength λ_R). Solid curves: $\nu = 0.34$, dashed curves: $\nu = 0.25$. Figure taken from Reference [32].*

After the second world war, when ultrasonic inspection methods emerged, the characteristics of surface waves made them an interesting candidate for non-destructive testing applications. In 1967, Viktorov [32] published a very extensive study of Rayleigh and Lamb waves. Apart from basic properties and the relationship between these two types of guided waves he also discussed issues of their excitation using wedge and comb transducers. Furthermore, he experimentally investigated the scattering of surface waves from isolated surface defects such as straight slots and semicircular grooves in dural bars. He found the reflection coefficient changed in an oscillating manner as a function of the defect depth due to resonances in the defect. He suggested that the period of the oscillation in the frequency domain could be used to determine the defect depth. Many researchers proposed this method for defect sizing, see for example Domarkas *et al.* [33], who also considered defects of finite length (as opposed to an infinitely long crack modelled with plain strain conditions). The method requires wideband signals with wavelengths smaller than the crack dimensions and assumes isolated defects with a simple geometry.

Another method makes use of the fact that the extended wave path caused by a defect compared to the undamaged specimen causes a phase delay for the transmitted signal. The condition for this is again that defects are isolated, simple and large compared to the length of the Rayleigh wave pulse. It is then possible to calculate the defect length from the time of flight of the pulse measured with a pitch-catch configuration. Hall [34] reported the use of such a method in 1976 to monitor the crack depth during fatigue testing of rails. The lack of accurate theoretical models and computer simulations made it necessary to use glass models and photoelastic visualisation to understand the complex scattering behaviour. The approach of measuring phase delay of transmitted signals is also proposed in more recent publications, see for example Masserey et al. [35].

In the 1970s, a lot of theoretical modelling was done for the development of surface acoustic wave (SAW) signal processing devices. The propagation of surface waves on various types of wave guides was of special interest, see for example Lagasse [36], Oliner [37,38] and Krylov [39,40]. Surface wave modes were investigated for example on wedges, grooves, curved surfaces etc. and were found to have slightly different properties compared to Rayleigh waves, for example in terms of group and phase velocity. In the context of SAW devices, Tuan and Li [41] determined the reflection of Rayleigh waves from a shallow rectangular groove or low step in an elastic half space using a boundary-pertubation technique. This was extended by Simons [42] to scattering by strips and periodic arrays of strips and grooves.

More analytical modelling for NDE applications of Rayleigh waves started in the 1980s. Achenbach and co-workers published exact analytical formulations based on integral equations for Rayleigh waves scattered from a transverse infinitely long surface-breaking crack, for both normal [43] and oblique incidence [44]. These theoretical predictions were confirmed experimentally by Adler and co-workers [45,46]. Vu and Kinra measured the diffraction of Rayleigh waves by an edge-crack both normal [47] and inclined [48] to a free surface. Zharylkapov and Krylov [49] also investigated experimentally the scattering of Rayleigh waves from transverse notches as well as measuring the resulting scattered fields of bulk longitudinal and shear waves.

Klein and Salzburger [50] developed an analytical approximation based on the work of Tuan and Li [41] which allows for a finite crack length and oblique incidence and verified it experimentally.

Auld *et al.* [51] and Tittmann *et al.* investigated the sizing of small semielliptical cracks by analysis of the scattered radiation pattern produced by incident short-wavelength surface waves. This requires measurements for a range of backscatter angles around an isolated defect.

For very high ratios of crack depth to wavelength, a body with an inclined crack can essentially be considered to be a wedge corner. Scattering from such wedge corners has been investigated for example by Fujii et al. [52, 53], Krylov et al. [54] and Babich et al. [55].

Parallel to developments of analytical models, the improved capabilities of computers facilitated the use of numerical simulations and allowed the visualisation of propagation and diffraction behaviour of waves. Hirao *et al.* [56], for example, investigated the scattering of Rayleigh waves by surface edge cracks using a finite-difference method (FDM). Bond and co-workers studied the scattering of Rayleigh waves from various geometries, first using FDM [57–59], later they applied an explicit finite element method (FEM) [60, 61]. In [61], Blake and Bond review the available techniques for defect characterisation using surface waves and discuss them critically. According to them, comparing the *amplitude* of the scattered wave field to that from reference features is a very simple method, but the scattered signal varies with the shape of the defect and the bandwidth of the transducer. *Time-of-flight* and *spectroscopic methods* only give information on the length of a surface feature (not on its orientation), and only work at high frequencies where the defect is large compared to the wavelength. Blake and Bond also point out that research until that point had concentrated only on isolated simple defects without considering, e.g., curved crack geometries, surface roughness, crack closure.

There have been first attempts to address these issues in recent years. As an example for more complex defect geometry, Hassan and Veronesi [62] investigated surface wave scattering from semicircular notches experimentally and using 3-dimensional FE simulations. Also the problem of crack closure has been dealt with: Pecorari, for example, modelled the scattering from a crack with faces in partial contact and also performed experiments [63].

Kim and Rokhlin [64] presented a low frequency scattering model for corner cracks initiated from a pit-type surface flaw. They measured changes of the reflection coefficient due to crack closure during fatigue testing of the test specimen. Another example for an application using Rayleigh waves for crack detection for low crack-depth-to-wavelength ratios was presented by Cook *et al.* [65]. They monitored the growth of small fatigue cracks in a sample under cyclic tensile loading and found that the amplitude of the scattered signal was proportional to the square of the crack radius.

An issue of interest with respect to RCF defects in rails is the influence of distributions of small surface-breaking cracks on the propagation of surface waves. Analytical models for this which predict attenuation and dispersion of surface waves transmitted through simplified cases of crack fields have been developed by Zhang and Achenbach [66] as well as Pecorari [67, 68]. Pecorari also presented a model which showed that compressional residual stress would reduce the dispersion effect caused by the crack field [69].

2.1.2 Surface waves for rail inspection

Early publications on surface waves used on rails date back to the 1970s and focussed on the high frequency regime. As already mentioned above, Hall [34] measured phase changes of transmitted signals in pitch-catch measurements to monitor crack growth during fatigue testing. Relatively high frequencies (4.2 MHz) were utilised to achieve short wavelengths and good signal separation, but signal interpretation was very difficult.

Bray *et al.* [70, 71] and Hirao *et al.* [72] investigated the propagation of Rayleigh waves in rails between about 0.4 to 3 MHz. Apart from the fundamental mode they also observed higher order Rayleigh (also called M_{21} or Sezawa) waves which they explained by the presence of a cold worked top layer in the rail head of about 3-6 mm thickness. These higher order waves were found to exist above frequencies of about 1 MHz and were proposed to be used for estimating the thickness and properties of the cold worked layer as well as for rail stress measurements. Grewal [73] suggested to utilise these waves for the detection of sub-surface defects, since they would be less susceptible to surface roughness or imperfections.

Recent publications tend to use surface waves at lower frequencies since these have a higher penetration depth and therefore can detect deeper defects. Armitage [27] used a pitch-catch setup of gel-coupled piezoelectric transducers at 140 kHz and measured the transmission of surface waves on a rail specimen containing gauge corner cracking. He observed notches in the frequency spectrum in comparison to that of an undamaged specimen which he claimed could be linked to the size of the defects.

Kenderian *et al.* utilised broadband laser generation and air coupled detection of Rayleigh waves for the detection of defects in the rail head [18] and the rail base [19, 28]. The frequency bandwidth of the signal was between 0.3 and 2 MHz and both transmitted and reflected signals were measured. Some problems they encountered were e.g. the sensitivity of the air coupled transducer to stand-off changes and the fact that the laser had to be used in the ablative regime in order to achieve a sufficient signal-to-noise-ratio. Such a high power regime might damage the rail surface, however, according to the authors the effect was found to be negligible.

Lanza di Scalea *et al.* deployed a probe setup similar to that of Kenderian *et al.* for the sizing of defects in the railhead, the signal frequency being between 100 kHz and 900 kHz [29]. They investigated both reflection and transmission from isolated artificial straight cuts across the railhead and in the gauge corner. A statistical approach using feature extraction and automatic pattern recognition algorithms was utilised to analyse the data.

Dixon and co-workers used electromagnetic acoustic transducers (EMATs) for sur-

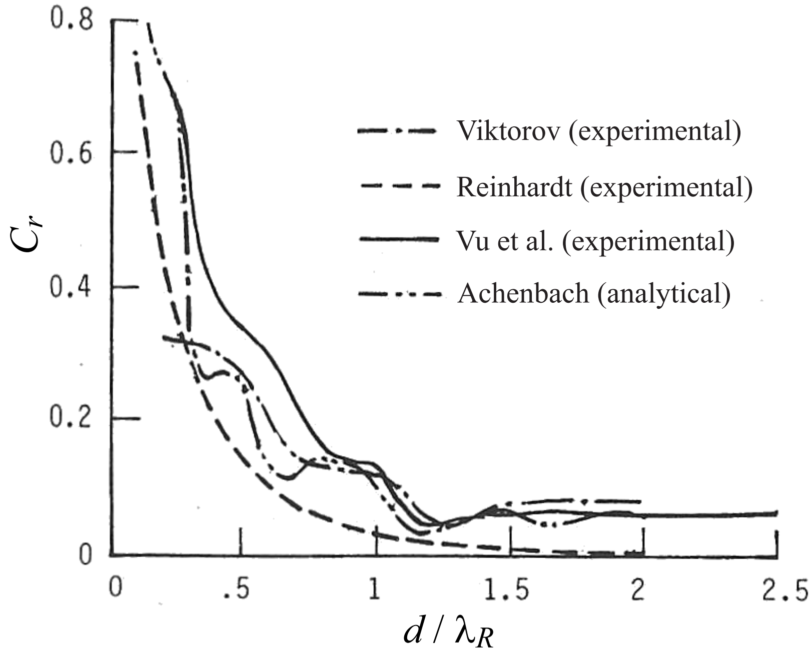

Figure 2.2: *Transmission coefficient of a Rayleigh wave incident at a transverse defect. Comparison of results of different authors, from Reference [47]. Dash-dot line: Viktorov [32]; dashed line: Reinhardt; solid line: Vu* et al. *[47], dash-dot-dot line: Achenbach* et al.

face wave excitation in rails at frequencies between 150 and 500 kHz [20, 30, 74, 75]. They used a pitch catch set up and tested three specimens (one with an artificial transverse notch across the railhead, one GCC specimen and another one containing a vertical longitudinal defect). They utilised the frequency content of the transmitted signals for defect sizing and report good agreement with an alternative test using an alternating current potential drop (ACPD) method [20].

It is noteworthy that results obtained from real GCC specimens have apparently not been verified by sectioning of specimens in any of these publications.

2.2 Approach in this work

The aim of this work was to develop a quick screening method to reliably detect critical defects in the rail head, in particular cracks that have turned transversely

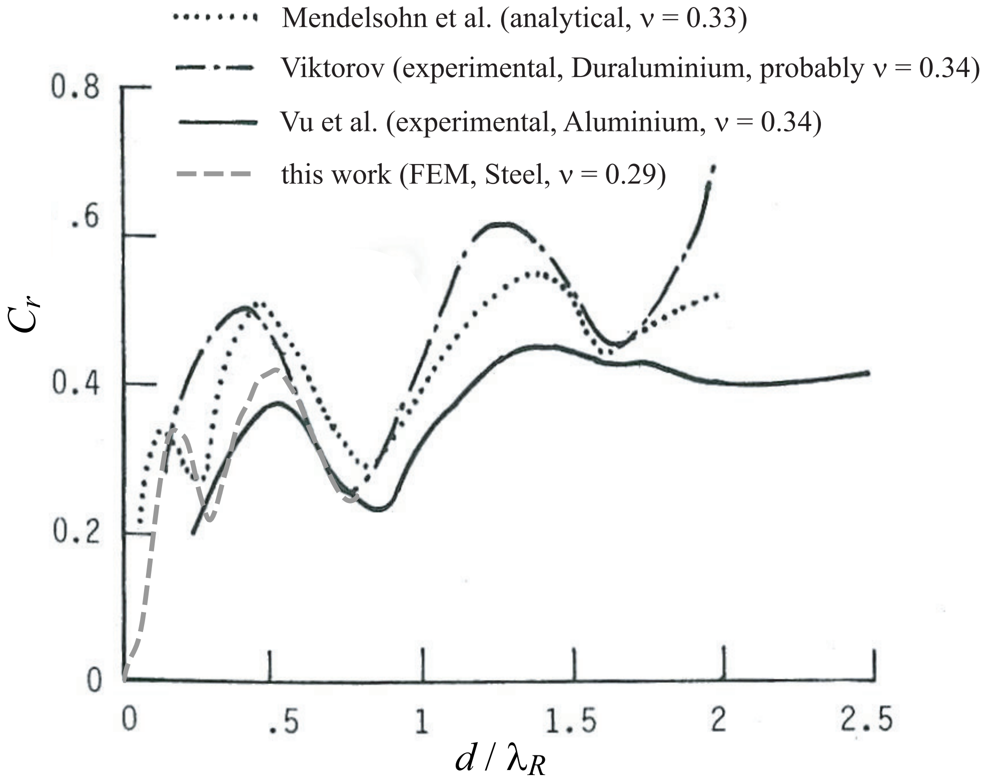

Figure 2.3: *Reflection coefficient of a Rayleigh wave incident at a transverse defect. Result from FEM simulations in this work (grey dashed line, see Appendix A) overlayed on Figure 8 in Vu* et al. *[47] comparing experimental data in that paper (black solid line) with analytical results by Mendelsohn* et al. *[43] (black dotted line) and experimental data by Viktorov [32] (black dash-dot line).*

downwards. Based on the preceding literature review on surface waves, there were the following general options to approach the problem:

- Transmission coefficient measurements
  - at low frequencies/large wavelengths: For small crack-depth-to-wavelength-ratios d/λ_R, the transmission coefficient decreases monotonically with d/λ_R, see Figure 2.2 taken from [47]. Amplitude measurements of the transmitted wave packet or, using broadband excitation, the frequency dependence of the transmission coefficient could be used for defect detection. Inclined defects with complementary angles Θ and $(180° - \Theta)$ cannot be distinguished [48], which could also be considered an advantage

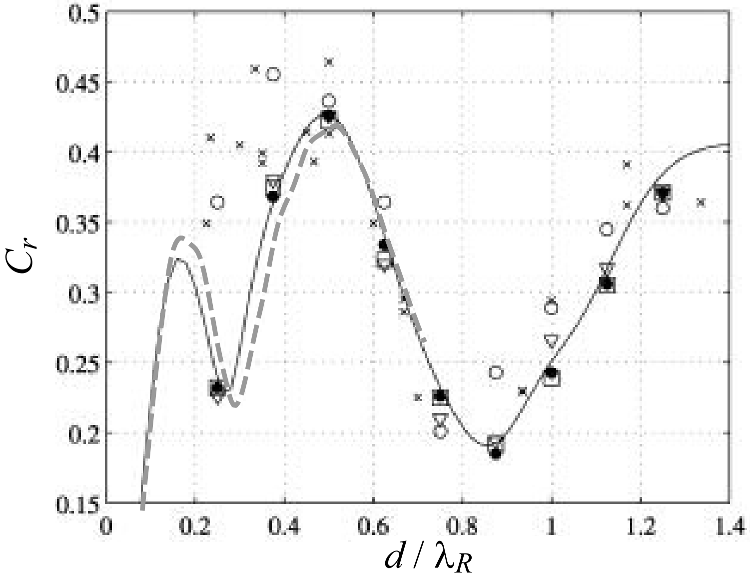

Figure 2.4: *Reflection coefficient of a Rayleigh wave incident at a transverse defect in steel. Result from FEM simulations in this work (grey dashed line, see Appendix A) overlayed on Figure 6 in Masserey* et al. *[35]. Analytical solution (based on Mendelsohn* et al. *[43]) in the far field (solid line), analytical solution in the near field (solid points), simulation with a slot (open points), simulation with crack model type 1 (triangles) and type 2 (squares), and experimental data (crosses).*

because of the simplified signal interpretation.

- at high frequencies/short wavelengths: The extended wave path and the resulting phase delay caused by transmission through a defect for small d/λ_R is proportional to the depth of a single defect. However, this method is not suitable for multiple and branching defects and on rough surfaces.

A problem with transmission coefficient measurements in general is that a pitch-catch signal itself does not contain any information on the number of detected defects and their location. It is the distance between the probes which defines the spatial resolution. Another issue is that variations of the signal amplitude due to inconsistent excitation or reception, for example due to changed surface conditions, may be falsely interpreted as defect indications.

- Reflection coefficient measurements
  - at low frequencies/large wavelengths: The reflection coefficient has the

tendency to increase with increasing d/λ_R up to $d/\lambda_R \approx 0.5$, see the comparison of some published data in Figure 2.3. As indicated by the analytical model by Mendelsohn *et al.* [43] (see the dotted line in Figure 2.3), there appears to be a local minimum around $d/\lambda_R \approx 0.2$. Finite element simulations were carried out at the start of this project to verify this behaviour for steel (see Appendix A) and the result was overlayed (grey dashed line) on the comparison published in Reference [47], see Figure 2.3. The results qualitatively agree with the curves, however, note that these are based on different material properties. Another comparison with a figure published by Masserey *et al.* [35] who used the analytical model of Mendelsohn *et al.* [43] and FD models for steel shows nearly perfect agreement, see Figure 2.4. This non-monotonic behaviour of the reflection coefficient could make precise sizing difficult, however it appears still feasible to differentiate shallow from deep defects. Furthermore, the reflection coefficient varies for different defect angles; complementary angles do not have the same reflection coefficient [48].

- at high frequencies/short wavelengths: At high d/λ_R ratios the reflection coefficient oscillates with d/λ_R due to crack resonances. Again this method does not appear suitable for multiple defects with complex shapes.

In spite of the fact that these considerations are essentially based on the simplified case of Rayleigh waves in plane strain conditions, they certainly helped to identify the most promising approach for this project.

It became clear that any approach using high frequencies would not be suitable in an environment with multiple defects and rough surfaces. At low frequencies (and low d/λ_R), the transmission coefficient appears generally to be less complex than the reflection coefficient, and it seems likely that a deep defect would affect the frequency content of the received signal similarly to a low pass filter. On the other hand the separation of gauge corner cracks in rails is very small and multiple scattering would lead to interference within the transmitted signal and an elongated signal tail. This would certainly complicate the frequency analysis and might lead to wrong interpretation if signal gates are chosen incorrectly. Furthermore, the number of defects would be unclear as well as their distribution between the transmitting and receiving probes. In order to have a good spatial resolution, the probe spacing would need to be small. This means that only small sections of rail would be screened with one measurement with little overlap between these sections. A large number of measurements would be necessary to cover the rail and only little signal redundancy would be available to compensate for coupling changes. Signal transmission measurements at low frequencies appeared therefore to be not well suited for this project either.

The measurement of the reflection coefficient in turn does provide information on position, extent and number of defective areas. Furthermore, variations of the signal amplitude (for example due to coupling changes) would only affect the ability to correctly size a defect, but it would not cause a false defect indication for a detected defect. Another advantage of measuring reflected signals is that the probe setup itself does not limit the range covered from one inspection position. Since surface waves can propagate several metres, it would be possible to gather redundant data while scanning along the rail. If the surface condition did affect for example the excitation of waves at certain measurement positions, then these sections would be covered from other positions as well and hence no section would remain untested. For all these reasons, amplitude measurements of reflected signals at low frequencies were chosen as the approach to fulfill the aims of this project.

The penetration depth and therefore the wavelength of these surface waves had to be chosen such that the reflection coefficient would be in the discussed range of $d/\lambda_R \leq 0.5$. In order to distinguish defects deeper than the critical depth of 5 mm from shallow surface cracks, a penetration depth of at least 10 mm is needed. This means that the frequency range has to be relatively low, i.e. around 250 kHz or less. In this frequency range, there are several options for transduction and reception of surface waves on rails:

- *Laser generation combined with another non-contact method for detection (e.g. air-coupled transducers [18, 19, 28, 29]).* This wide-band non-contact method avoids the need of couplant, however standoff changes of the detectors can affect the signal. Further problems are a low signal-to-noise ratio and the need to use high power for generation which might damage the rail.

- *EMATs.* Another non-contact method which avoids the need for couplant at the expense of low signal-to-noise ratio and sensitivity to standoff changes.
- *Local immersion probe.* This is an ultrasonic wedge method which can be implemented into a wheel probe. Due to the use of piezo-electric transducers, the signal-to-noise-ratio is very high and both narrow and wide-band signals are possible. Since it is a contact method it might be affected by surface damage. This problem would be overcome by gathering redundant data as mentioned above. The measurement of the reflected signals can be performed with a single probe in pulse-echo mode. Furthermore, the concept is very similar to currently utilised ultrasonic inspection equipment which is why it could be easily integrated into an existing system.

For the approach chosen in this work, i.e. measurement of reflected signal amplitudes, the use of a local immersion probe was therefore selected as the best solution.

2.3 Summary

A brief literature review has been presented on surface waves utilised in the context of NDT applications. The number of publications on this topic is vast, therefore only a limited number of references with relevance for the work undertaken in this thesis has been selected. Additionally, research carried out elsewhere regarding the use of surface waves for rail inspection has been presented. Based on these two overviews, the options available to approach the problem have been discussed. It was decided to utilise a local immersion wheel probe and to measure the signals reflected from defects, rather than performing transmission measurements. The signals would need to be at fairly low frequencies around 250 kHz or lower to achieve the required penetration depth of more than 10 mm. There are a few potential drawbacks of this approach:

- The probe requires contact with the rail surface.
- The behaviour of the reflection coefficient appears to be more complex than that of the transmission coefficient.

However, these are outweighed by the following main benefits:

- The location of defects can be determined from the measured signal itself.
- Amplitude changes due to changed surface condition cannot falsely be interpreted as defects.
- The signals cover long sections of rail (several metres) from each measurement position. Redundant data would ensure full coverage and could be used to compensate coupling changes.
- A wheel probe could easily be integrated into existing inspection systems and does not damage the rail surface.

The chosen approach appeared therefore to be the most promising for developing a robust screening tool which could reliably detect critical defects in the railhead.

Chapter 3

Surface waves in plates

3.1 Background

The chosen approach for surface wave inspection of railheads aimed at using low frequency waves with wavelengths greater than 10 mm (see Section 2.2). This means that the geometric dimensions of the rail head such as width, thickness and curvature radii are of the same order of magnitude as the wavelength. It was therefore anticipated that the complex geometry would affect the properties of the surface waves. The finite thickness of the railhead appeared to be an especially important parameter since Rayleigh waves strictly speaking are defined on an infinite half space. The first step in this work was therefore to verify whether the chosen approach of utilising low frequency surface waves could be used for defect sizing in plates with the thickness of a railhead. Once the issues associated with the finite thickness were sufficiently understood in plates, it would be much easier to move on to the more complex structure which is the railhead.

Following a very brief review on guided waves and the associated terminology, the properties of quasi-Rayleigh waves in plates will be briefly presented in this chapter, as well as the implications for the applicability of the Rayleigh wave reflection coefficient. The subsequent sections deal with experiments performed for the verification of these predictions and FEM simulations to investigate the encountered problems.

Lastly, the findings are summarised and conclusions for the project are drawn.

3.2 Surface waves and guided wave modes

In this thesis the term *surface waves* will be used as the general term to describe waves in a body confined to a region close to the surface. *Rayleigh waves* will only be used in the strict sense, i.e. for surface waves on an infinite half space. Surface waves on waveguide structures (such as plates, pipes, rails) can be analysed using modal analysis, see for example References [32, 76–78]. This approach is an advantageous alternative to a field decomposition in terms of bulk waves and provides a natural basis for analysing waveguide excitation and scattering problems. The total field in a waveguide is thereby interpreted as a superposition of all guided wave modes supported by the structure. These guided wave solutions are assumed to be proportional to a propagation factor e^{ikz}, where the waveguide is aligned along the z axis and k is the propagation constant or wavenumber. For real values of k (assuming a non-lossy waveguide), the solutions are called *propagating modes.* Since these modes are not attenuated and carry energy along the structure (theoretically over an infinite distance), they are of special interest for inspection purposes. For purely imaginary or complex values of k, the modal solutions are called *non-propagating* or *evanescent modes.* Such modes form the near field around features and loads and decay exponentially with distance. Wave modes which are confined to a region close to the surface of the waveguide will be called *surface (wave) modes* in this thesis.

3.3 Quasi-Rayleigh waves

Lamb modes are propagating guided wave modes in free isotropic plates. In plates with a sufficient thickness (at least twice the Rayleigh wavelength according to Viktorov [32]) the combined excitation of the fundamental symmetrical and anti-symmetrical Lamb modes A_0 and S_0 approximates to some extent a Rayleigh wave. This is because each of the two modes has an either symmetric or anti-symmetric

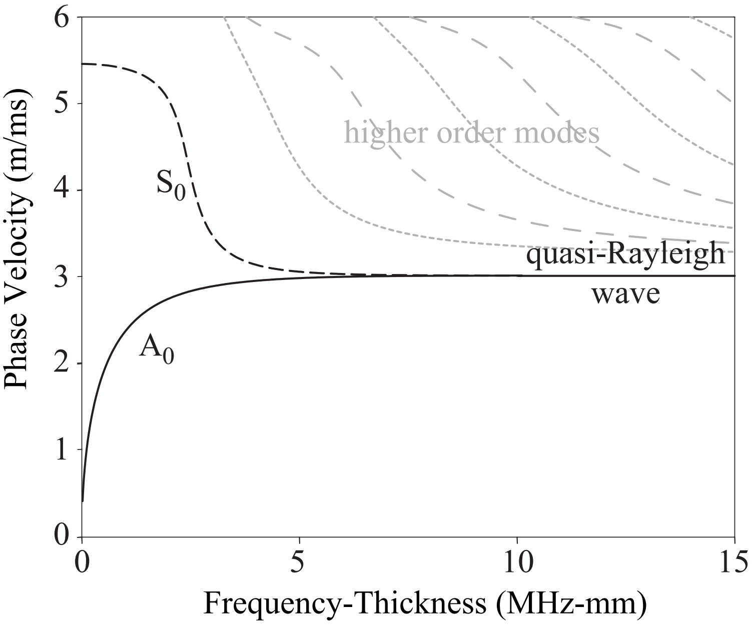

Figure 3.1: *Phase velocity of A_0 and S_0 Lamb modes and quasi-Rayleigh wave in a steel plate.*

mode shape which essentially consists of a surface wave on each plate surface. In the limit, as the frequency-thickness-product approaches infinity, the added fields of A_0 and S_0 will cancel on side of the plate and add on the other, thus generating a true Rayleigh wave on one surface of the plate [76].

For plates with finite thickness, the combined wave of A_0 and S_0 is called the quasi-Rayleigh wave [32], coupled Rayleigh wave [79] or coupled surface wave [76,80]. The last two names result from the fact that the field pattern of such a wave on one surface of a plate has a residual amplitude on the opposite surface and therefore is weakly coupled to it. Since the two modes have different wave numbers k_{A_0} and k_{S_0}, they shift in relative phase as they travel. After a propagation distance l, such that

$$(k_{S_0} - k_{A_0})l = \pi, \tag{3.1}$$

the two modes will be in phase opposition and the field will correspond to a surface wave on the opposite surface. Because of this beating of the two Lamb modes energy will be transferred continually between the two surfaces with a transfer period of $2l$.

While some authors suggest making use of this 'surface wave transfer' for special

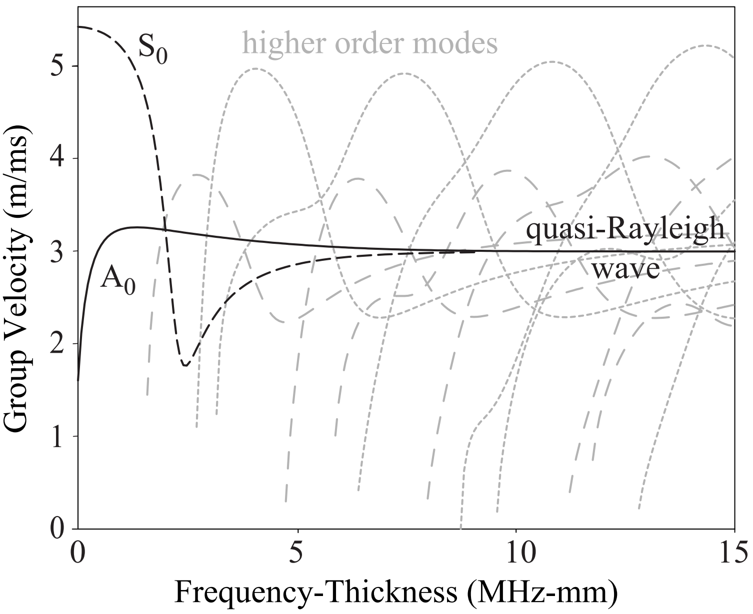

Figure 3.2: *Group velocity of A_0 and S_0 Lamb modes and quasi-Rayleigh wave in a steel plate.*

NDT applications (see e.g. [79,80]), the phenomenon had to be avoided in this work. It was crucial that A_0 and S_0 would have nearly identical mode shapes across one half of the plate thickness and the same phase velocity such that they would appear as one single surface wave. If their velocities differed slightly but not enough to separate the signals, then their interference would lead to varying signal amplitudes depending on the distance between defect and probe. If, in addition to this, their mode shapes were slightly different, then the reflected and transmitted signal components of A_0 and S_0 would not be identical. The unknown contribution of each of the two modes would make it very difficult to correctly interpret the varying signal amplitudes for defect sizing.

As explained in Section 2.2, the aim was to achieve a surface wave penetration depth into the material of at least 10 mm. The head thickness of standard rail types such as UIC 60 and BS 113A is about 40 mm [8]. The frequency of the quasi-Rayleigh wave had to be chosen to be as low as possible to achieve sufficient penetration, but high enough to ensure very similar properties of A_0 and S_0. Phase and group velocity dispersion curves obtained with the DISPERSE software [81] indicated the

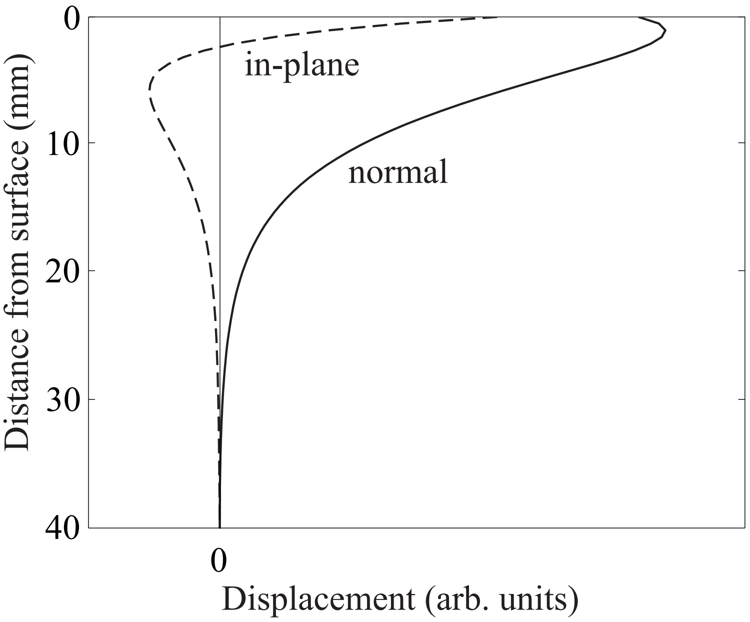

Figure 3.3: *Displacement field in normal and in-plane direction of a quasi-Rayleigh wave (combination of* A_0 *and* S_0*) in a 40 mm thick steel plate at 250 kHz.*

frequency-thickness range around 10 MHzmm to be a reasonable choice for steel plates, i.e. around 250 kHz for a 40 mm thick plate. At this frequency, A_0 and S_0 have nearly identical phase and group velocities, see Figures 3.1 and 3.2. Note also that the distance l of a surface wave transfer to the opposite plate surface according to (3.1) would be about 70 m in this case and therefore is not critical at all. In this frequency-thickness range, the quasi-Rayleigh wave can be expected to be sensitive to defects in a depth of up to approximately a third of the plate thickness. This can be seen in Figure 3.3, which shows the combined in-plane and normal displacement fields of the A_0 and S_0 modes in a 40 mm thick steel plate at a frequency of 250 kHz. The combined displacement field of the two modes is practically identical to that of a true Rayleigh wave at the same frequency, as confirmed by the DISPERSE software. Therefore the reflection coefficient curve determined for a true Rayleigh wave (see Figures 2.3 and 2.4) is applicable for quasi-Rayleigh waves in this frequency range. In terms of the scattering behaviour it therefore seemed feasible to ignore the effect of the finite plate thickness on the surface waves.

3.4 Experimental study of reflection from transverse defects

The experimental study in this section was performed in order to investigate whether detection and sizing of transverse defects was feasible with low frequency surface waves in plates. It was necessary to verify that the scattering behaviour in the chosen frequency range was the same as that of a true Rayleigh wave as suggested in the previous section and to assess whether the finite thickness of the plates would cause any other issues.

At this stage only isolated transverse defects were considered. It was decided to perform the experiments with a robust method which could directly be applied to multiple defects as well. Since spectral analysis is not reliable when the reflected Rayleigh wave fields can not be separated from additional reflections due to edges or multiple defects (see Blake and Bond [61]), the best option was to measure the peak envelope of the incident and reflected signals. Provided the peak amplitude of the incident wave is known and kept constant, then it would only be necessary to measure the reflected signals, for example in a pulse-echo setup with a single probe.

3.4.1 Prediction of reflection ratio

Due to the finite bandwidth of the excitation the reflection ratio $\tilde{C}_r$, i.e. the ratio of the measured peak incident and reflected signal envelopes, would be slightly different from the true reflection coefficient C_r. The dashed grey line in Figure 3.4 (see also Figures 2.3 and 2.4) shows the reflection coefficient C_r as a function of the normalised defect depth (d/λ_R) for a true Rayleigh wave. It was determined using FEM simulations, see Appendix A. The prediction of the reflection ratio $\tilde{C}_r$ for the finite bandwidth signal (solid line in Figure 3.4) was generated in the following way: first, the true reflection coefficient curve in Figure 3.4 was transformed into a function of frequency by utilising the Rayleigh wave velocity and setting a fixed notch depth. This was then used to weight the amplitude spectrum of the excitation

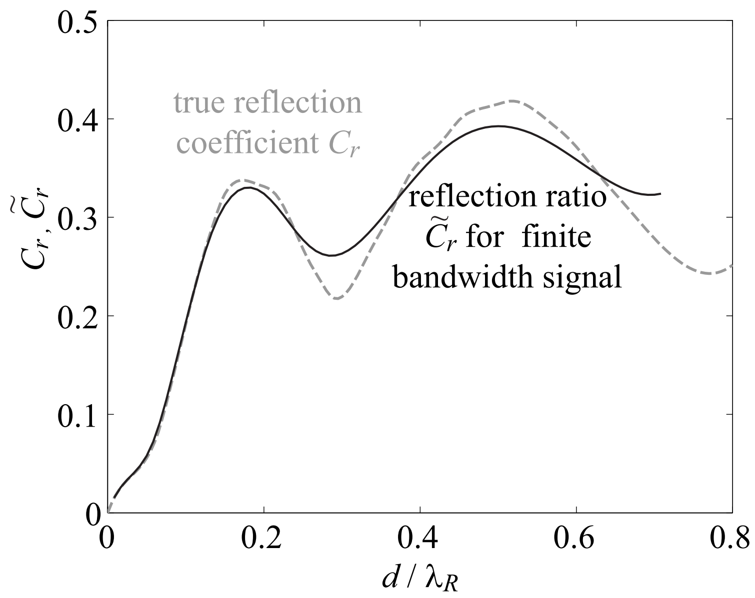

Figure 3.4: *Grey dashed line: reflection coefficient of a true Rayleigh wave for transverse defects of depth* d *normalised to wavelength* λ_R *(from FEM simulations in Appendix A, see also Figures 2.3 and 2.4). Solid line: prediction of the reflection ratio that would be measured with a finite bandwidth signal (250 kHz, 5 cycle tone burst), defect depth* d *normalised to* λ_R *at the centre frequency.*

signal (a 5 cycle Hanning windowed toneburst at 250 kHz). Note that, for simplicity, the phase of the spectral reflection coefficient was assumed to be constant rather than frequency dependent; the true phase spectrum of the reflection coefficient can be found e.g. in [56]. Subsequently, the inverse Fourier transform of the product gave an approximation of the reflected wave in the time domain. The predicted reflection ratio was calculated as the ratio of the signal envelope peaks of the reflected and the incident wave. Sweeping through a number of different defect depths and normalising them to the wavelength of the toneburst centre frequency finally led to the solid curve for $\tilde{C}_r$ in Figure 3.4. This could then be used for the immediate interpretation of experimental results. A second curve was generated for a centre frequency of 300 kHz, but found to be nearly identical with that at 250 kHz. Thus, only one curve was used for both frequencies for comparison with the experimental results.

3.4.2 Experimental Method

Seven mild steel plates served as test specimens and were chosen to have a thickness of 38 mm (1.5”), thus approximating the thickness of a railhead. They were 300 mm long and 140 mm wide, the width being the limit that could be processed by the spark erosion machine used for machining a transverse EDM-notch (Electrical Discharge Machining) of depth d (1 mm to 7 mm) into each specimen over the whole plate width. Each of these notches had a width of about 0.3 mm and a round tip with a diameter of the same value. The density of the mild steel was measured to be $\rho = 7760$ kg/m^3. Young's modulus ($E = 210$ GPa) and Poisson's ratio ($\nu = 0.287$) were calculated from measurements of the longitudinal and the shear wave velocity ($c_l = 5.93$ m/ms, $c_s = 3.24$ m/ms).

The excitation of quasi-Rayleigh waves on the surface of the specimens was realised by using a local immersion method (see e.g. [82]). It is an implementation of the coincidence principle which applies a load distribution on the surface of a solid through impingement of bulk waves at a certain angle φ such that waves with a corresponding wavelength are excited in the solid. According to Snell's Law, the angle φ is given by

$$\sin\varphi = \frac{\lambda_w}{\lambda_R} = \frac{c_w}{c_R} \quad , \tag{3.2}$$

where λ_w is the wavelength and c_w the bulk velocity in the coupling material (here: water), λ_R is the wavelength and c_R the velocity of the wave to be excited (here: the quasi-Rayleigh wave). In this case, for the coupling medium water with $c_w =$ 1.5 m/ms and a Rayleigh wave velocity c_R in steel of approximately $c_R = 3$ m/ms, this results in $\varphi = 30°$.

A schematic of the local immersion probe used for the experiments is shown in Figure 3.5. It consisted of a broadband immersion transducer (Imasonic 4052 A 101) with a centre frequency of 250 kHz, placed in a water-filled angled aluminium casing. In order to damp internal signal reflections that reverberate in the water column, the casing was coated with 10 mm thick sheets of ultrasonically absorbent rubber (NPL Aptflex F28). The latter matches the acoustic impedance of water

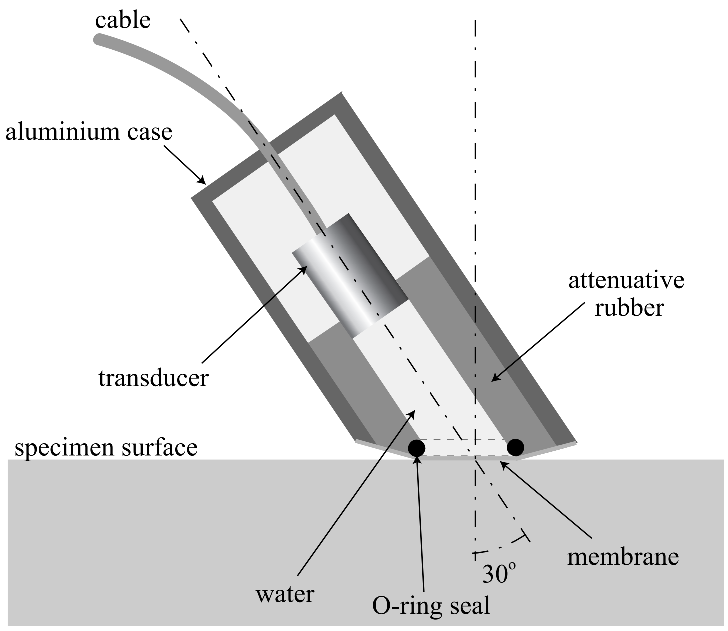

Figure 3.5: *Angled local immersion probe (cross-section).*

and features a transmission loss of approximately 3 dB mm^{-1} MHz^{-1} [83]. The problem of leakage or even the need to drain and refill the probe when changing its position (e.g. for scanning) was overcome by using a closed casing with a contact patch at the bottom. This consisted of a cellophane membrane and an O-ring seal with a diameter of 25 mm that defined the contact area and therefore ensured reproducible results. The O-ring seal also limited the contact area in order to avoid energy leakage of the excited surface wave into the water column. The effect of the cellophane membrane on acoustic signals at the frequencies used here (150-350 kHz) is negligible. However, the contact area had to be slightly wetted to provide good coupling between the membrane and the specimen surface.

During the experiments the local immersion probe was placed in the centre of the specimen width at a distance of 140 mm from each notch respectively, see Figure 3.6. An additional mass was fixed to the probe to ensure an upright and stable position. The excitation signal sent to the transducer was a 5 cycle Hanning windowed tone burst generated by a "Macro Design WaveMaker-Duet". Two sets of measurements were performed on each specimen: one at a centre frequency of 250 kHz and a second at 300 kHz. Using two different frequencies was advantageous to obtain more points

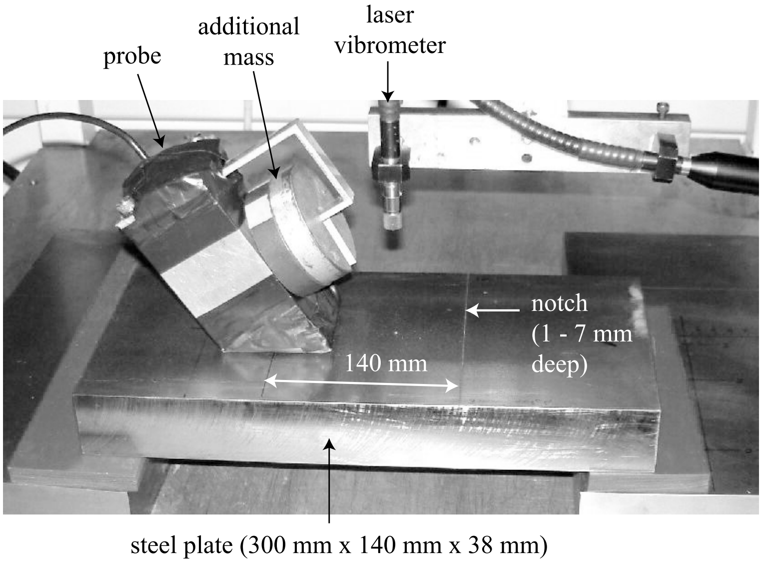

Figure 3.6: *Experimental setup.*

for the reflection ratio curves at different normalised defect depths. Instead of using the pulse-echo method, the out-of-plane velocity fields of waves incident on and reflected back from the notch were measured with a laser vibrometer (Polytech OVF 512). Each set of measurements consisted of 21 laser signals captured at equidistant points along a line between the probe and the notch, the distance from the notch being 45-105 mm (3 mm spacing). By measuring with this non-contact method at several positions between transducer and notch it was possible to determine the beam spreading of the probe and eliminate its effect on the results. This was necessary to compare the experimental results with the prediction in Section 3.4.1 which assumed plane wave propagation. The reason for measuring velocities instead of displacements was the better signal-to-noise-ratio of the velocity decoder at the frequencies used here. The received signals were captured in a digital oscilloscope and passed to a PC for processing.

3.4.3 Results

Figure 3.7 shows a typical example of a signal measured with the laser vibrometer. By applying the Hilbert transform and taking the modulus of the so-called analytic

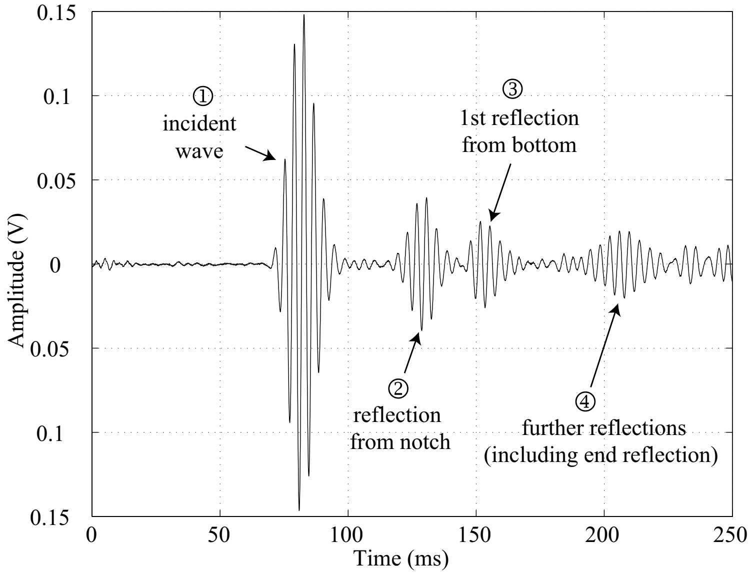

Figure 3.7: *Measured signal at 69 mm from the probe on a 38 mm thick plate with a 6 mm deep notch, centre frequency 250 kHz (frequency-thickness about 10 MHzmm).*

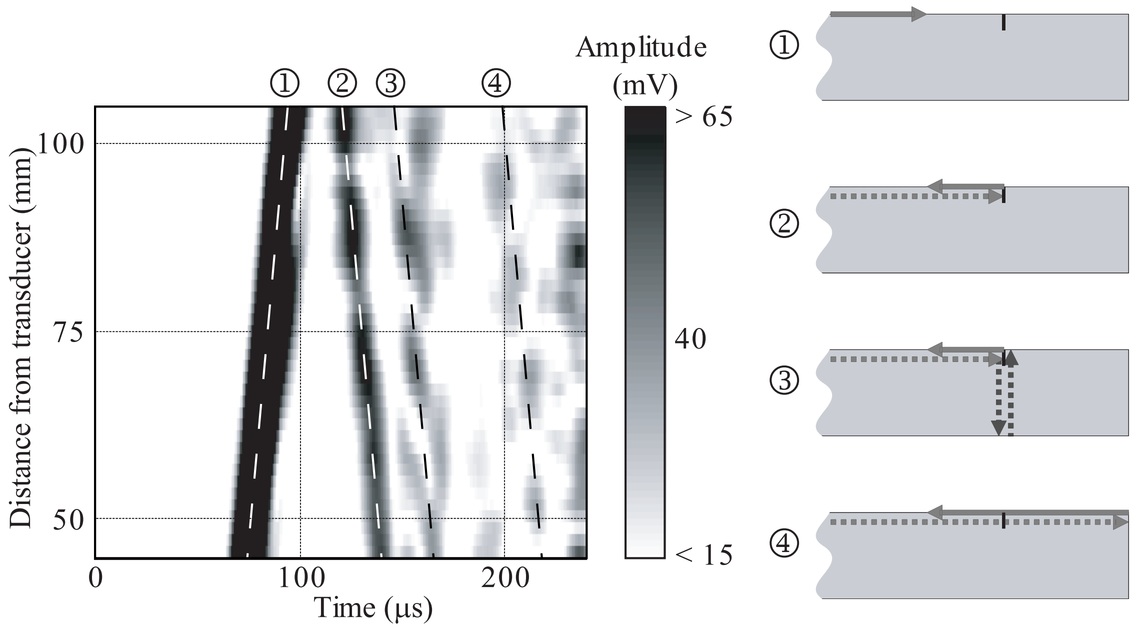

Figure 3.8: *B scan of experimental data on a 38 mm thick plate with a 6 mm deep notch and wave paths for different signals (frequency-thickness about 10 MHzmm).*

signal [84], the envelope of the measured signal was generated. In Figure 3.8, the signal envelopes of all laser positions measured on one specimen are shown as a single B-scan type plot. Note that the linear greyscale does not represent the full dynamic range, i.e. the incident wave signal (labelled "1") appears to be "clipped". In all measurements not only the incident wave signal and the reflection from the notch were observed, but also distinct signals following the reflection from the notch, see Figures 3.7 and 3.8. The wave paths of these signals are illustrated in Figure 3.8: Signal number "1" corresponds to the incident wave, number "2" is the notch reflection and the arrival labelled "4" is the reflection from the end of the plate. The unexpected signal "3" was identified as a mode conversion that the transmitted part of the surface wave exhibits when reaching the tip of the notch: the surface wave is converted into a shear bulk wave which propagates to the bottom of the specimen. From there, it is reflected back to the notch, is partially converted into a surface wave again and finally propagates back along the specimen surface (see Figure 3.8). Another part of the signal may be reflected as a shear wave to the bottom of the plate and from there back to the notch again etc. Further repetition of this conversion and scattering process leads to further surface wave echoes with decaying amplitudes which might wrongly be interpreted as reflections from several defects. The phenomenon of the bottom reflection is also mentioned by Blake and Bond [61] and Kim and Rokhlin [64]. However, this appears to be a particular issue in plates with transverse defects because of the parallel plate surfaces and the right angles formed with the notch. In order to avoid overlapping of the direct reflection from the notch and the first bottom reflection for a given plate thickness, the wave packet has to be sufficiently short, i.e. the centre frequency has to be chosen to be high enough with a small number of cycles. In this case, for a plate thickness of 38 mm and a 5 cycle Hanning windowed tone burst at centre frequencies of 250 and 300 kHz, the separation was sufficient.

In order to determine the reflection ratio $\tilde{C}_r$ for a given notch depth and signal centre frequency, the envelope peaks nearest to the expected arrival times of the incident and reflected waves were plotted for a set of measurements against their respective propagated distance x from the local immersion probe, see the example in

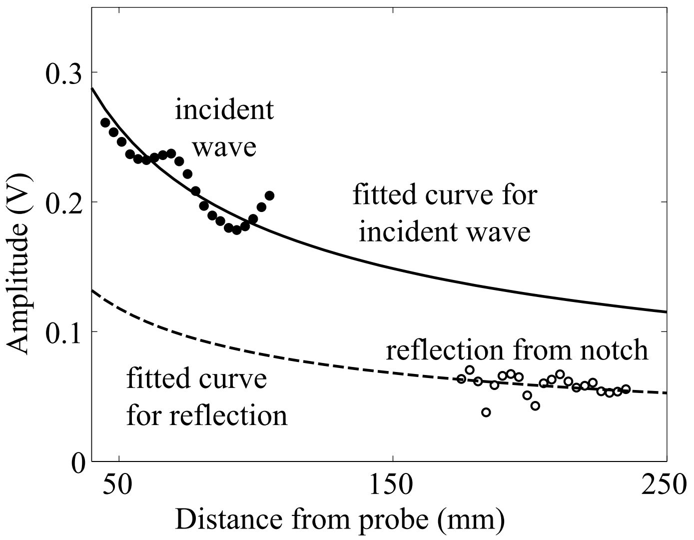

Figure 3.9: *Comparison of incident and reflected wave amplitudes at different positions between probe and notch.*

Figure 3.9. In the case of the reflection from the notch this distance is the sum of the distances between probe and notch and between notch and measurement position of the laser interferometer. Due to the divergence of the beam emitted by the source, the Rayleigh wave amplitude A_R decays with distance

$$A_R = \frac{A_0}{\sqrt{k_R x}} \quad , \tag{3.3}$$

where A_0 is a constant factor, k_R the wave number of the Rayleigh wave and x the distance from the source [32]. Curves assuming this relation were fitted to the incident and the reflected wave data respectively using the least squares method and show good agreement, see Figure 3.9. The signal attenuation due to beam spreading was therefore compensated by multiplying each incident and reflected envelope peak with the corresponding factor $1/\sqrt{x}$ before calculating the reflection ratio $\tilde{C}_r$.

An important observation in all experiments was that the amplitudes of both incident and reflected waves exhibited modulation in space. This can clearly be seen for the incident wave in the example in Figure 3.9. For the case of the reflection from the notch this is more obvious in Figure 3.8. Since the amplitude variation was not random but followed a consistent pattern, it appeared to be an interference phenomenon rather than random noise. Apparently not only quasi-Rayleigh waves, but

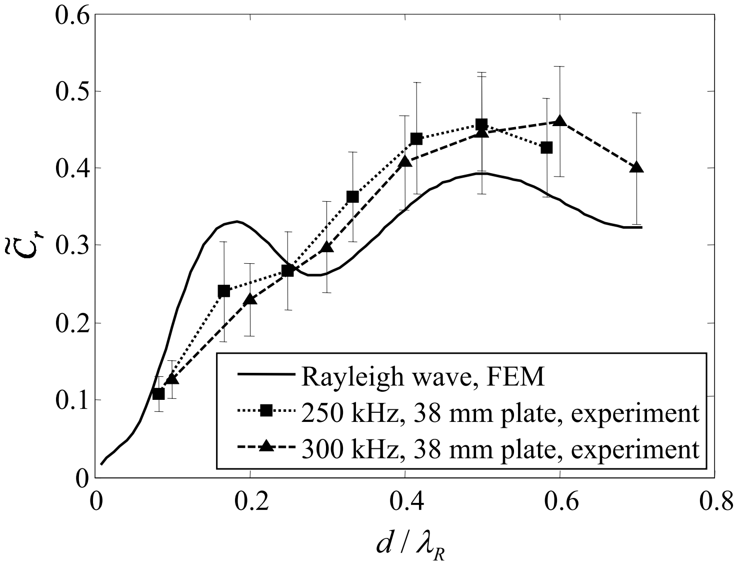

Figure 3.10: *Comparison of predicted and experimentally measured reflection ratios for transverse defects. Markers denote average reflection ratio, error bars indicate standard deviation.*

additional guided wave modes with similar propagation velocities were present in the measured signals. (When utilising the approach of decomposition into bulk waves rather than modal analysis, then this phenomenon can alternatively explained with the unwanted excitation of bulk waves and their reflections from the boundaries. However, that approach can be very cumbersome for complex waveguides.) In order to reduce the effect of coherent noise, the average reflection ratio was determined for each set of vibrometer measurements.

The results for the reflection ratios as a function of the notch depth normalised to the wavelength are displayed in Figure 3.10. The average reflection ratios from measurements taken with a centre frequency of 250 kHz are indicated with squares, and values for 300 kHz are marked with triangles. The error bars shown represent the standard deviation for a set of measurements and illustrate the substantial variation of both incident and reflected wave amplitudes. The average reflection ratio obtained experimentally increases more or less monotonically with increasing defect depth for a notch depth to wavelength ratio smaller than 0.5. This was a promising result for inspection purposes. However, when comparing these measurements to the predicted reflection ratio $\tilde{C}_r$ from section 3.4.1 (shown as the solid curve, found to be applicable for both 250 and 300 kHz), it turns out that the experimental values only broadly follow the trend of the prediction. The experimental values are consistently higher than the prediction for d/λ_R greater than 0.25. Furthermore, the measured results for a normalised notch depth d/λ_R below 0.25 are lower than the prediction and do not exhibit a distinct local maximum. These discrepancies appeared to be related to the problem of coherent noise and were investigated further using FEM simulations.

3.5 Finite Element Simulations

3.5.1 Models

The Finite Element Simulations presented in this section were performed to understand the discrepancy between predicted and measured reflection ratio as well as the amplitude variations of the quasi-Rayleigh waves encountered during the experiments, see section 3.4.3. As these variations were found not only for reflected but also for incident waves, it was assumed that they were caused by the chosen excitation method.

The FEM simulations to address these issues were performed with the software package ABAQUS using its time marching *Explicit* solver. The finite element models were 2-dimensional, i.e. plane wave propagation was assumed and the effect of beam spreading was therefore not considered. The mesh of all models consisted of square elements with 0.5 mm side length to ensure a sufficient spatial resolution. The following three types of models were investigated:

(a) *Exact mode shape method and transverse defects.* Seven models of plates with transverse defects of varying depth d (1-7 mm) were generated matching all properties and dimensions of the experimental specimens (see Figure 3.11a). The defects were modelled by disconnecting elements. Quasi-Rayleigh waves were excited at one end of the specimen using the "exact mode shape method"

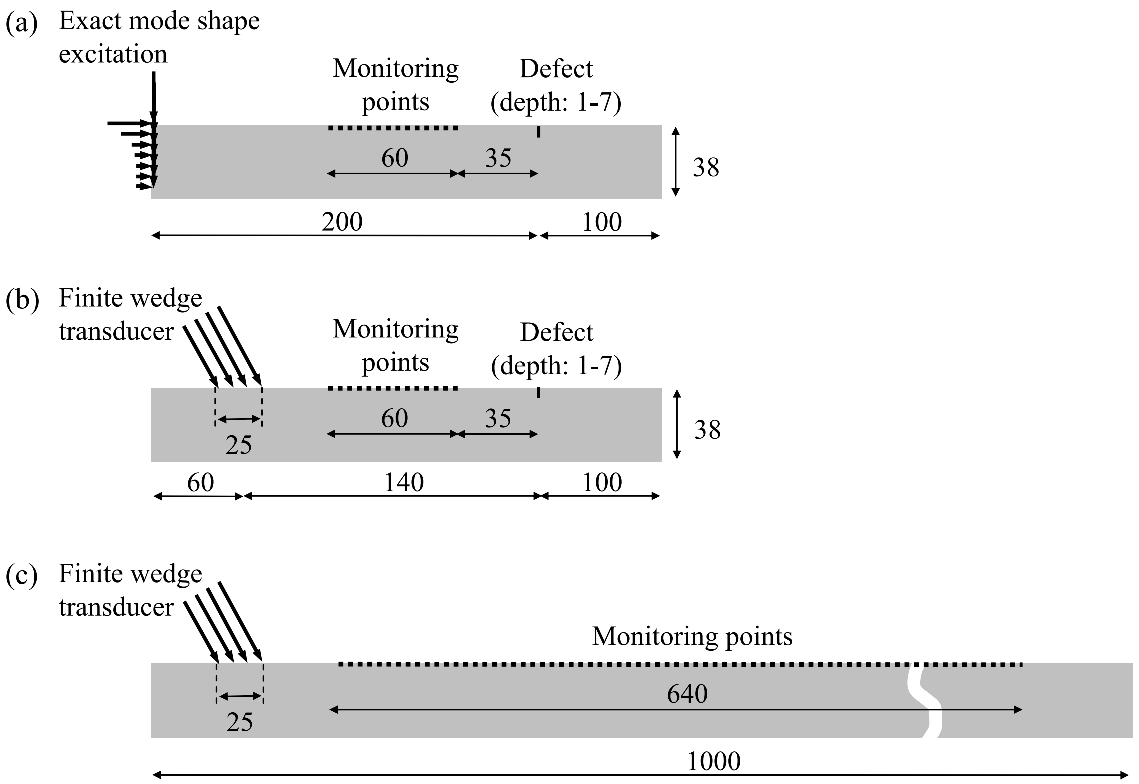

Figure 3.11: *Sketches of utilised FEM models: (a) exact mode shape method and transverse defects, (b) finite wedge transducer and transverse defects, (c) finite wedge transducer on long plate without defects. All dimensions in mm.*

(see e.g. Reference [85]). Firstly, for all frequencies of the finite bandwidth excitation (5 cycle Hanning windowed toneburst at 250 kHz) with significant amplitudes, the power normalised displacement profiles of the Lamb modes A_0 and S_0 were determined using DISPERSE [81] and summed to form a quasi-Rayleigh wave. Secondly, the discrete frequency components of the signal were multiplied by the appropriate displacement profiles and finally summed up, thus generating a frequency spectrum for both spatial directions at each node of the plate end face (or rather end line in this 2-dimensional model). Thirdly, an inverse Fourier transform was performed on all spectra to obtain time domain signals for each excitation node which could be applied as input displacement-time functions in the FE model. The advantage of this method was that only the desired quasi-Rayleigh wave was excited and unwanted modes could therefore only occur in the reflected signal. The incident and reflected signals were monitored in the FE models at locations corresponding to the laser vibrometer measurements in the experiments. From the monitored signals the reflection ratios were calculated in exactly the same way as for the experiments (except for the beam spreading compensation).

(b) *Finite wedge transducer and transverse defects.* Apart from the excitation, these models and the signal processing of the results were identical to the previous ones (see Figure 3.11b). However, the excitation was realised using a distributed load on a 25 mm long region of the plate. The excitation force at each node was phase shifted such that the effect was the same as that of a plane incident wave in water impinging at an angle of 30° on the plate surface (note: since the water was not modelled, leakage into the fluid was not taken into account). By doing this, the probe was modelled as a plane wave weighted with a rectangular spatial window with the dimensions of the probe used in the experiments. It was therefore possible to study the effect of unwanted modes excited by the finite length transducer. The excitation signal was again a 5 cycle Hanning windowed toneburst at 250 kHz.

(c) *Finite wedge transducer on long plate without defects.* In this model, a 1 m long steel plate with the same thickness as the models before (38 mm) but without defects was considered (see Figure 3.11c). The excitation was again the same finite wedge transducer as for model type "b". This model was used to determine the modal content of the excited signal using a 2-dimensional Fourier transform (2D-FFT) [86, 87]. The latter was applied to the out-of-plane-displacement of the signals which were monitored along the surface at 256 points with 2.5 mm spacing. The significantly greater length of the plate model compared to those discussed before was necessary to achieve sufficient separation of the modes in the 2D-FFT. This requirement was also the reason why such a measurement was not performed experimentally: the available specimens would have been too short.

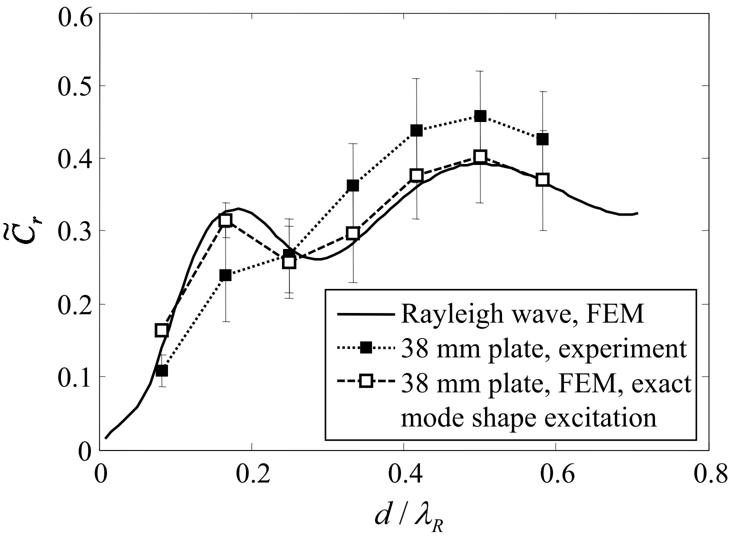

Figure 3.12: *Comparison of predicted and experimentally measured reflection ratios with model type "a" FE simulations (exact mode shape excitation). Markers denote average reflection ratio, error bars indicate standard deviation.*

3.5.2 Results

Figure 3.12 compares the quasi-Rayleigh reflection ratios obtained from the FEM simulations of model type "a" using exact mode shape excitation (white squares) with the experimental results (black squares) and the prediction for a Rayleigh wave (solid line), see also Figure 3.10. As discussed above, the exact mode shape excitation method ensured that only quasi-Rayleigh waves were excited and the incident wave signal was therefore found to be constant for all monitoring points. The reflected signal, however, exhibited amplitude variations indicating the presence of several modes due to mode conversion at the defect. The reflection ratio therefore varied for different monitoring points in one model. The standard deviation of this variation is similar to that of the experimental results as indicated by the error bars in Figure 3.12. Nevertheless, the average reflection ratios of the type "a" FE model agree very well with the theoretical Rayleigh wave prediction and less well with the experimental results. Apparently, the simple averaging of the reflection ratios obtained for different monitoring positions in that FE model was sufficient to remove the effect of unwanted modes in the reflected signal. The divergence of the

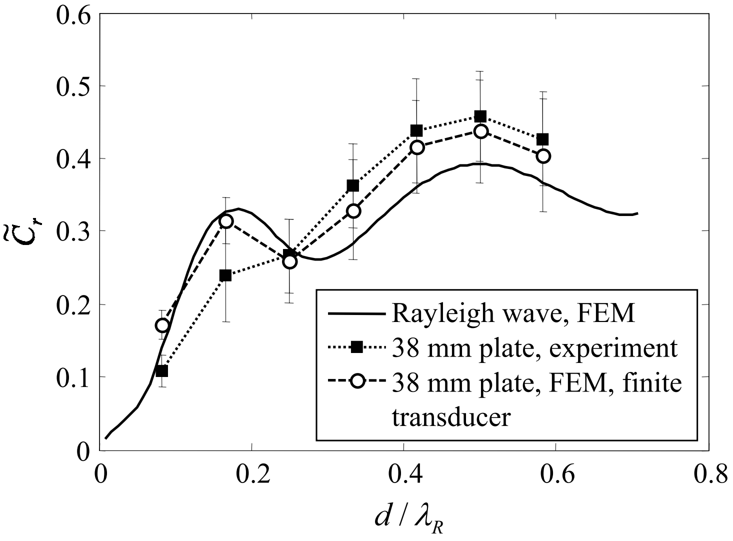

Figure 3.13: *Comparison of predicted and experimentally measured reflection ratios with model type "b" FE simulations (finite wedge transducer). Markers denote average reflection ratio, error bars indicate standard deviation.*

experimental results was therefore unlikely to be caused only by multiple modes in the reflected signals.

In Figure 3.13, the results from the FEM simulations with model type "b" (white circles) are compared to experimental results (black squares) and the prediction for a Rayleigh wave (solid line). The excitation in these models was realised with a finite length wedge transducer which would not necessarily only excite quasi-Rayleigh waves. This explains why both incident and reflected waves were found to exhibit amplitude variations along the monitoring positions, very similar to those observed experimentally. In fact, the average reflection ratios of the FEM simulations with model type "b" agree well with the experimental results for normalised notch-depths d/λ_R larger than 0.25. The standard deviation indicated by the error bars is similar, too. Therefore the validity of the model within that range of defect depths was confirmed. The discrepancy for smaller notch depths is likely to be caused by the finite width of the notch with respect to its depth in the experimental specimens as opposed to the sharp cut used in the simulations (see for example Blake and Bond [60, 61] for a discussion on the influence of the notch depth and width on the

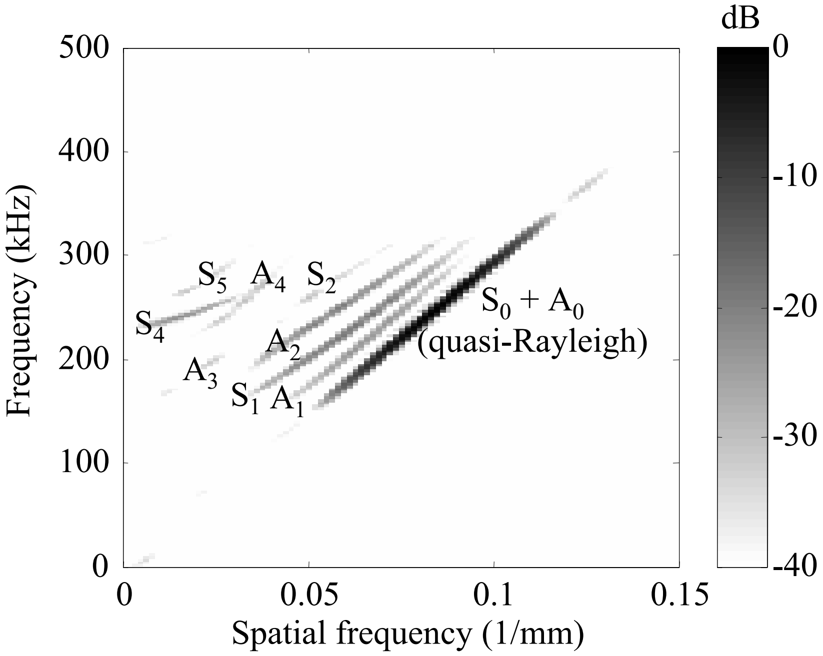

Figure 3.14: *Normalised modulus of 2D-FFT of simulation data from FE model type "c". The excited Lamb modes are labelled.*

reflection coefficient). The important thing to note is that for the case of the finite wedge transducer, the averaging of the measured reflection ratios did not sufficiently remove the effect of unwanted modes.

The third type of FEM simulation was performed to establish which unwanted types of modes were present in the signals excited by the finite length transducer. For this purpose, a 2D-FFT was applied to the monitored signals. Figure 3.14 shows the normalised modulus of the 2D-FFT in greyscale versus the temporal and spatial frequency. (Note that the term spatial frequency is used in this thesis for the term $\frac{k}{2\pi}$). The excited modes were identified by overlaying dispersion curves of Lamb modes and are labelled accordingly. It can clearly be seen that most of the energy is carried by the modes A_0 and S_0, which form the quasi-Rayleigh wave. However, even higher order modes, such as A_1, S_1, A_2 and S_4, are excited at significant amplitudes. This explains the amplitude modulation which was encountered in the simulations as well as in the experimental data. Furthermore, this proves that the modulation was caused by the excitation of propagating modes and that it was not a nearfield

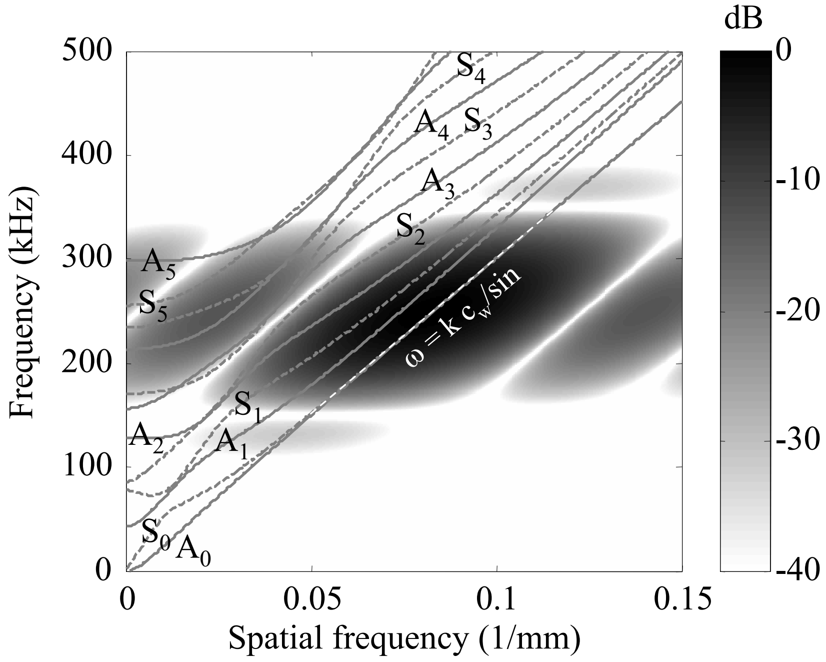

Figure 3.15: *Transmitter sensitivity $B(\omega)$ of a plane wave incident at 30° weighted with a 25 mm long rectangular spatial window in order to model a finite wedge transducer. The sensitivity is additionally weighted with the amplitude $A(\omega)$ of a 5 cycle Hanning windowed toneburst at 250 kHz. Overlaid dispersion curves of a 38 mm thick steel plate.*

artefact.

The reason for the relatively inefficient excitation of the quasi-Rayleigh wave becomes clear when determining the transmitter sensitivity of the utilised source. For the model of the finite wedge transducer used in the FE simulation (represented by a plane wave weighted with a rectangular spatial window), this can be done analytically. In this thesis a simplified approach is utilised, which only considers the effect of the surface loading as a spatial window, see Appendix B. (For a more rigorous analytical approach to directly compute the vibration field excited by a finite stress load on the surface of a solid refer for example to Miller and Pursey [88].) Based on the simple considerations in Appendix B, the transmitter sensitivity $B(\omega, k)$ for such a source of length L (here $L = 25$ mm) can then be expressed as

$$B(\omega, k) = \operatorname{sinc}\left[\frac{L}{2}\left(\frac{\sin\varphi}{c_w}\omega - k\right)\right] \cdot L. \tag{3.4}$$

The normalised modulus of B for this case weighted with the amplitude $A(\omega)$ of the utilised narrow-band signal is displayed in Figure 3.15 as a greyscale plot in the 2-dimensional frequency domain. It shows the presence of a main excitation region in the centre and a number of side lobes around it, the latter being due to a Hanning window in the time and rectangular window in the spatial domain. The regions are tilted depending on the wedge angle φ, see (3.4). The overlaid dispersion curves of the relevant Lamb modes for a 38 mm thick steel illustrate the lack of selectivity of the probe and explain the observed modes in Figure 3.14. However, the extent to which a guided wave mode is actually excited in these regions depends additionally on its excitability (see [89]). For the plate thickness in this case, most of the modes located in the excited range appear to be easily excitable in the frequency range of interest, see Figure 3.14. Only a larger transducer with a significantly longer contact patch of about 200 mm would lead to a sufficiently narrow wave number bandwidth and hence less excitation of higher order modes. Note that this is not only an issue of the probe type utilised here; this issue is independent from the type of excitation, i.e. it also applies to laser, EMATs etc. Since it was planned to use a wheel probe for the excitation at a later stage of the project with a limited contact area, this issue of mode selectivity would need further consideration.

3.6 Summary

In this chapter, the scattering of quasi-Rayleigh waves in plates with transverse notches at a frequency-thickness of 10 Mhzmm was investigated. This was a first step to test the viability of low frequency surface wave testing on structures with finite thickness. In order to develop an experimental method which could be used on specimens with multiple defects, it was decided to analyse the peak amplitude of the reflected signal rather than utilising spectral methods. A local immersion probe was built for the excitation that could be used also for reception in pulse-echo mode at a later stage. In order to verify the FEM based prediction for the reflection ratio, it was necessary to eliminate the effect of beam spreading. For this reason a laser vibrometer was used to measure both the incident and the reflected wave signals.

One issue observed in the measured signals was the occurrence of multiple signals caused by plate bottom reflections which might wrongly be interpreted as reflections from several defects. However, this appears to be a particular issue in plates with transverse defects because of the parallel plate surfaces and the right angles formed with the notch. In more complex structures (like for example rails) with curved surfaces and angled defects this might be less of an issue.

The average reflection ratio obtained experimentally was found to increase more or less monotonically with increasing defect depth for a notch depth to wavelength ratio smaller than 0.5. This was a promising result for inspection purposes. However, the finite length of the probe severely limited its mode selectivity. This led to the excitation of multiple modes which complicated the signal interpretation and resulted in discrepancies between predictions and measurements. It was shown that calculating the mean of several reflection ratios measured at different locations on the specimen would not sufficiently remove the effect of unwanted modes. The danger of unknown modal content of the signals is wrong interpretation and therefore potentially under- or overestimation of defect severity. One way of overcoming this issue would be to utilise a very long probe, i.e. with a large dimension in the direction of wave propagation. However, the required length for a sufficient selectivity in thick plates would be around 200 mm which would be challenging for any type of excitation method. At a later stage of this project it was planned to use a wheel probe for the surface wave excitation which can of course only provide a limited contact patch, comparable to the size used in the experiments and simulations in this chapter. It appeared therefore that the large wave number bandwidth and the resulting excitation of higher modes had to be accepted at this stage. The next step in the project was to investigate to what extent the excitation of multiple modes would also be an issue on rails.

Chapter 4

Surface wave modes in rails

4.1 Background

In order to detect critical defects in the railhead and distinguish them from shallow, tolerable ones, it is advantageous to utilise low frequency surface waves with a penetration depth of at least 10 mm. Maximising the penetration depth also reduces the sensitivity to non-critical features at the rail surface which otherwise might complicate signal interpretation. The wavelength of such low frequency surface waves is of the same order of magnitude as the width, the thickness and some radii of the rail cross section so that the influence of the wave guide geometry cannot be neglected. Surface waves on various other types of wave guides have been extensively investigated in the context of Surface Acoustic Wave (SAW) devices, see for example Lagasse [36], Oliner [37, 38] and Krylov [39, 40]. However, these studies cannot be directly applied to establish a frequency range for low frequency surface wave inspection of rails. Furthermore, knowledge about similar wave modes is vital to understand problems arising from multiple-mode excitation such as those encountered in Chapter 3 for the case of surface waves in thick plates. Complex signals caused by interference can lead to wrong interpretation when considered as a single Rayleigh wave arrival rather than a superposition of multiple surface wave modes. This issue has not been addressed in other publications on surface waves in rails such as References [18–20, 27–30, 74, 75]. Finally, it was necessary to determine how the propagation and the mode shapes are affected by cross-section changes due to wear.

In this chapter, the characteristics of surface modes in rails are therefore investigated in detail and the implications for rail inspection are discussed. First, experimental results which demonstrated the presence of multiple surface modes are presented. The subsequent section explains how the different modes were identified using FE simulations. There then follows a discussion of the properties of surface wave modes such as strain energy distributions and group velocities and their implications for rail inspection. Finally, a FE technique is presented which was used to verify the surface wave mode shapes.

4.2 The problem of multiple mode excitation

The concurrent existence of multiple surface wave modes in rails and their interfering behaviour was demonstrated with a very simple experiment. The idea was to excite surface waves using a standard setup and monitor the wave amplitude during propagation along the rail.

In the experimental setup used here, a local immersion probe angled at the Rayleigh wave angle (30°) was located centrally on the top surface of a BS113A type rail (see Figure 4.1). The probe was very similar to that used in Chapter 3, the only difference being that it was sealed at the bottom with a rectangular 5 mm thick rubber contact patch which matched the impedance of water. This was an improvement on the previous version in terms of robustness. Again, a few drops of water were sufficient to ensure good coupling between the 20 mm wide, 25 mm long contact patch and the rail surface. All measurements were carried out using a 5 cycle Hanning windowed tone burst with a centre frequency of 250 kHz. The excited and scattered wave fields in the rail were determined by moving a single-point laser vibrometer to 205 positions with 3 mm spacing along the centreline of the rail and measuring the velocity component normal to the rail surface.

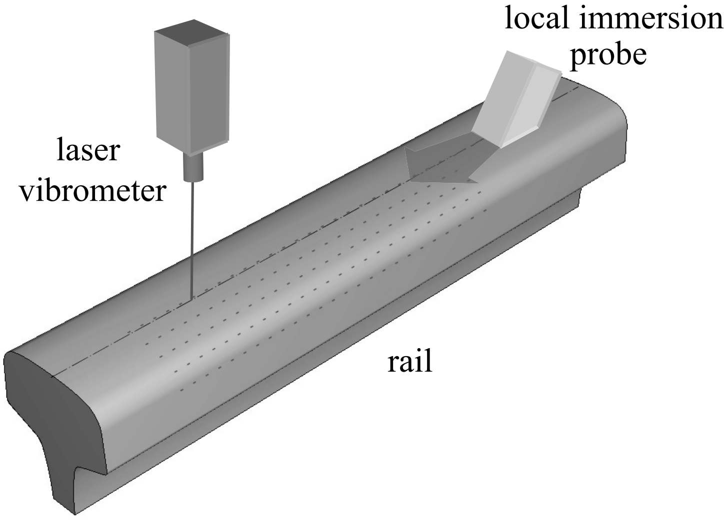

Figure 4.1: *Experimental setup for studying surface wave propagation in rail (only rail head and top of web shown).*

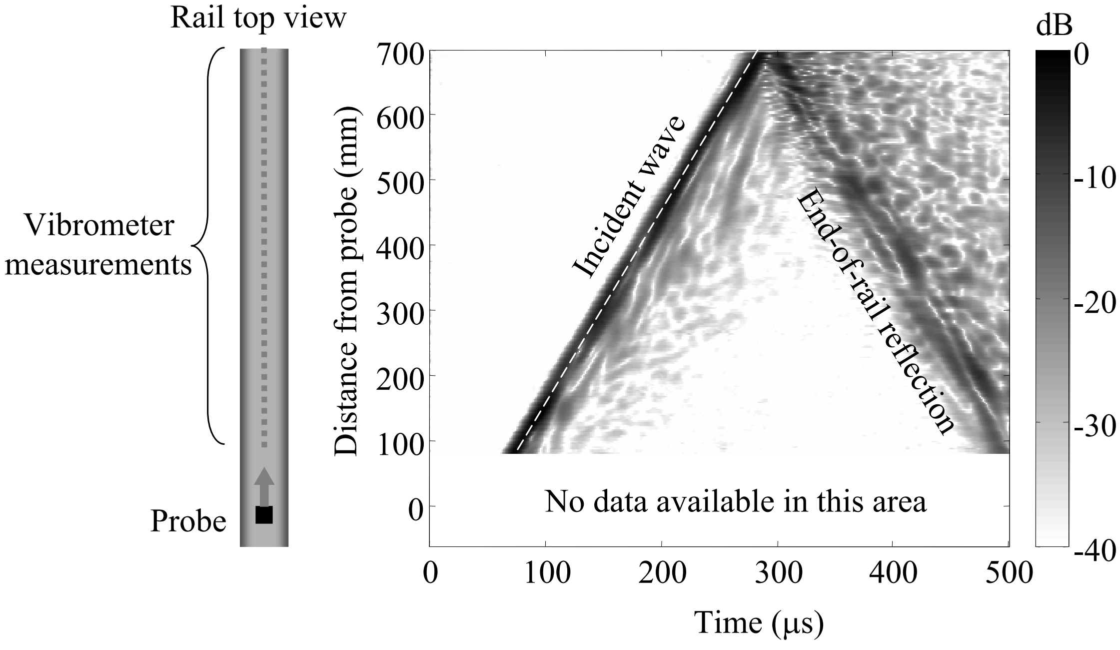

Figure 4.2: *B-scan plot of signal envelopes from vibrometer scan on rail.*

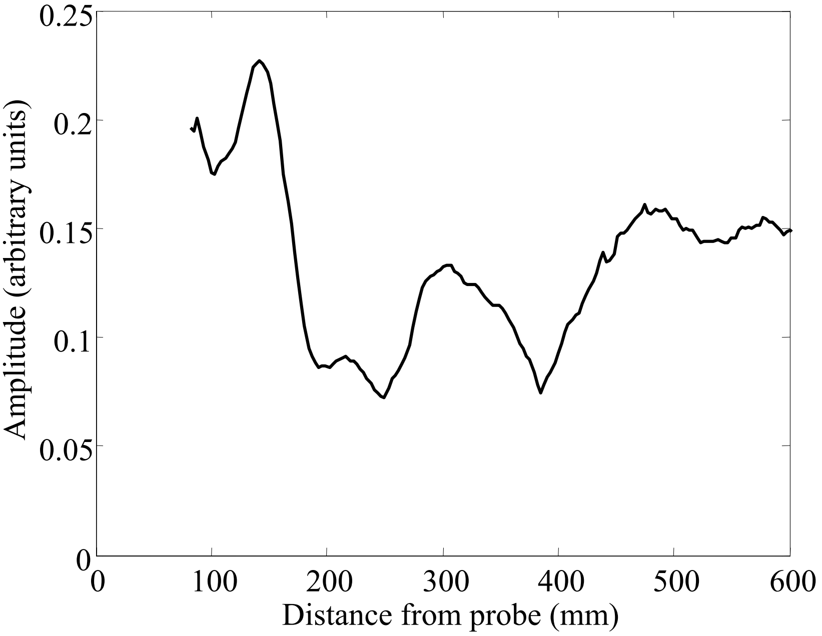

Figure 4.3: *Maximum of surface wave envelope as a function of the distance between probe and vibrometer.*

Figure 4.2 shows the envelopes of the acquired signals in a B-scan type plot. Both the incident signal and the reflection from the end of the rail are indicated. Unsurprisingly, the latter appears to be very complex due to scattering and mode conversion at the end of the rail and obviously contains a multitude of different interfering signals which result in varying amplitudes along the rail. However, it can also be seen that even the incident wave is not a clearly defined wave packet. The amplitude of the incident wave is heavily modulated in space and does not decay gradually like a single pure Rayleigh wave would due to beam spreading. This is shown clearly in Figure 4.3, in which the signal envelope peaks nearest to the expected arrival time of the incident wave are presented as a function of the distance between the probe and the vibrometer position. This plot is essentially a section of the B-scan in Figure 4.2 along the white dashed line (note that values closer than 100 mm to the end of the rail are not shown to avoid near field effects). Since the number of measurement points was very large (about 180) and the modulation was very consistent, the latter had to be caused by the interference of multiple wave modes rather than random noise. Different modes will have slightly different wavelengths

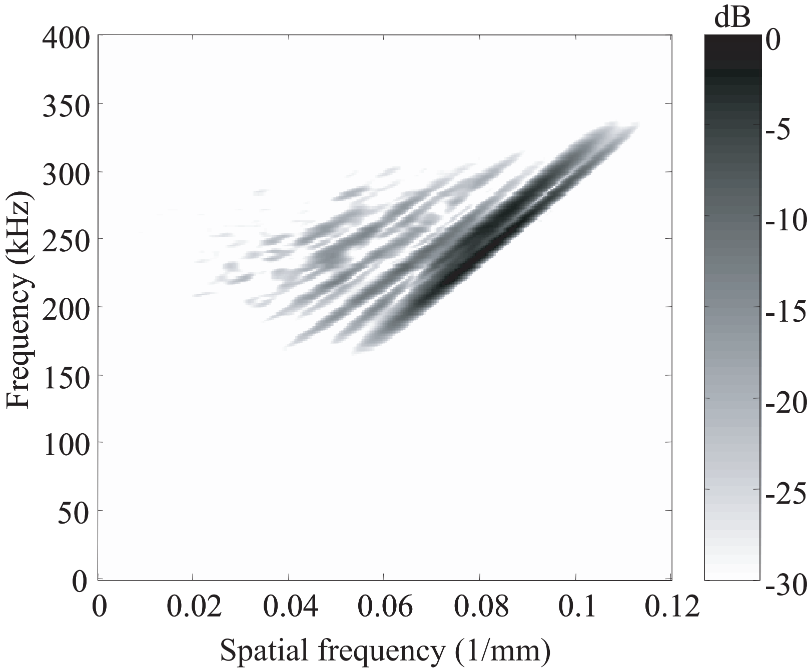

Figure 4.4: *Normalised modulus of 2D-FFT performed on centerline scan.*

and velocities and therefore cause the observed irregular pattern of constructive and destructive interference.

This was confirmed further by applying a two-dimensional fast Fourier transform (2D-FFT) to the data obtained from the vibrometer scan (The 2D-FFT was carried out on the raw RF data, rather than the envelope shown in Figure 4.2). The normalised modulus of the result is plotted as a greyscale against the spatial and temporal frequency in Figure 4.4. The grey patches correspond to different modes which are present in the signal and exhibit different dispersion relations between wave number and frequency. Due to resolution limits the regions overlap, so that it is not clear exactly how many modes are present.

The results clearly illustrate that the Rayleigh wave probe excited a large number of modes in the rail with different phase and group velocities, which explains the interference phenomenon of the incident wave in Figures 4.2 and 4.3. Thus, any surface wave arrival at such low frequencies can potentially be an interfering group of guided wave modes in the rail cross section, rather than a single Rayleigh wave.

4.3 Identification of surface wave modes

Having established the fact of multiple mode excitation, it was necessary to identify the mode shapes and dispersion curves of the relevant surface wave modes. These characteristics provide crucial information for choosing guided wave modes suitable for inspection purposes and optimising their excitation.

4.3.1 Dispersion curves of guided wave modes in rails

The exact analytical analysis of wave propagation characteristics is only possible for wave guides with simple cross-sections such as cylinders [90], ellipses [91] and rectangles with certain ratios of width to depth [92]. Under certain conditions it is possible to develop asymptotic analytical solutions for rods of arbitrary cross-section, for example for short wavelength high frequency surface waves [39,40,93–96] and long wavelength low frequency waves [93]. However, in order to obtain dispersion curves over a wide range of frequencies and wave numbers it is necessary to use numerical methods. Nigro [97] utilised the variational method of Ritz for bars with rectangular cross-section. Fraser [98, 99] obtained dispersion curves for bars with rectangular and elliptical cross-section using the method of collocation. Elliptical and truncated elliptical cross-sections were investigated by Nagaya [100] using a Fourier expansion collocation method. Lagasse [36] developed a semi-analytical finite element (FE) technique to calculate dispersion curves for topographic wave guides of arbitrary cross-section used for SAW devices. Recently, an alternative approach for guided wave modes in bars using boundary element analysis was presented by Gunawan and Hirose [101].

Gavrić was the first to employ a FE method to calculate dispersion curves and mode shapes for rails (up to a frequency of 6 kHz) [102]. This method was adapted by Wilcox *et al.* for the use of standard FE software [89] and applied to rails for frequencies up to 50 kHz [23]. Similar FE methods were proposed for example by Gry [103], Hayashi *et al.* [104, 105] and Damljanović and Weaver [106], the latter

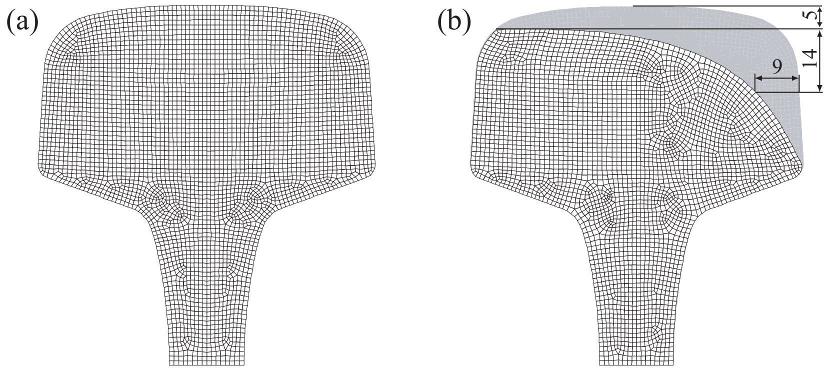

Figure 4.5: *Finite element meshes for generation of dispersion curves and mode shapes: (a) new rail, (b) extremely worn rail (grey area indicates removed part of cross section, dimensions in mm).*

even allowing for non-propagating modes. Bartoli *et al.* [107] extended the semi-analytical FE technique to allow for viscoelastic material damping and applied it to rails. In all these publications, guided wave propagation in rails has been analysed at relatively low frequencies ($\leq$ 100 kHz) and surface wave modes have not been discussed.

In this work, the method described by Wilcox *et al.* [89] was applied. Its basic concept is to consider a ring with very large diameter instead of a straight waveguide. This can be modelled using only a 2-dimensional (2D) mesh and boundary conditions for cyclic symmetry which are often provided by standard FE software (in this case FINEL/FE77 [108]). For a given cyclic order, the code generates a chosen number of eigenfrequencies and eigenvectors, i.e. the vibration solutions of standing waves in the ring. Each of these can then be decomposed into two identical propagating waves travelling in opposite directions. The cyclic order of the standing wave corresponds therefore to the number of wavelengths of a guided wave mode around the ring, with the eigenvector being its displacement distribution or mode shape at the corresponding (eigen-)frequency.

Cross-sections of both new and extremely worn UIC60/CEN60E1 rails were considered, see Figure 4.5. The material properties for steel were assumed to be Young's modulus $E = 210$ GPa, Poisson's ratio $\nu = 0.287$ and density $\rho = 7760$ kg/m^3 (see

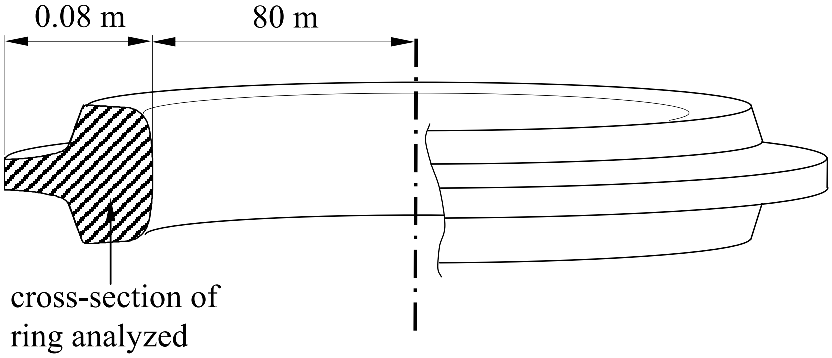

Figure 4.6: *Modelling of the rail waveguide as a ring with large radius (dimensions not to scale).*

Section 3.4.2). The worn rail was assumed to have 5 mm vertical head loss and 9 mm lateral head loss at the gauge corner (measured 14 mm below the top of the worn railhead), which is close to the tolerated limits in the UK [109]. For the correct computation of mode shapes at higher frequencies it was necessary to set up fairly fine FE meshes. They consisted of about 4100 (3300 for the worn rail) linear 4-node elements with a side length of approximately 1 mm. In order to overcome computer memory limitations, reduce computation time and avoid solutions which are not relevant for railhead inspection (e.g. modes that are confined to the rail foot) only the upper half of the rail cross section was modelled (see Figure 4.5). As long as the strain energy density of a mode is negligibly low at this artificially introduced free boundary, the mode shape and propagation characteristics can be considered to be identical to those of the full rail section.

In order to avoid slightly asymmetric mode shapes at low frequencies due to curvature effects, the symmetry axis of the ring was chosen to be perpendicular to the symmetry axis of the rail section, see Figure 4.6. Restrictions in the FE software limited the model radius to 80 m which is 100 times larger than the width of the ring cross section. Concerns regarding unwanted effects of curvature on the mode shapes are addressed in Section 4.5, where it is shown that the results are not affected at all above 120 kHz.

Figure 4.7 shows the dispersion curves for the first 100 propagating modes of the

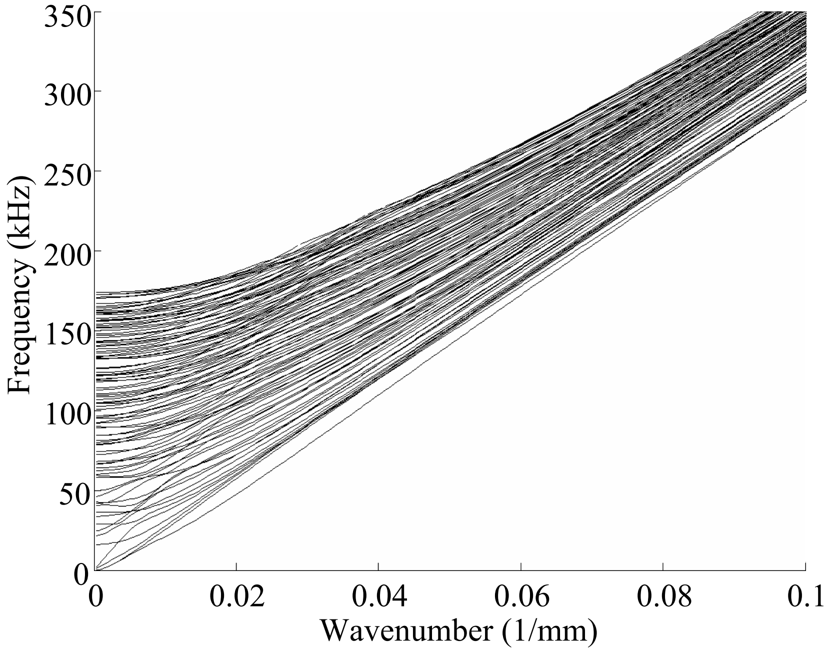

Figure 4.7: *Dispersion curves of the first 100 propagating modes of the FE model for the new rail.*

new rail model (Figure 4.5a), the highest cutoff frequency being at about 180 kHz. Not all these modes are relevant in the context of railhead inspection, therefore the extraction of relevant surface wave modes is discussed in the following section.

4.3.2 Extraction of relevant surface wave modes

Surface wave modes can be identified within the large number of possible guided wave modes by comparing how efficiently they are excited by a probe located on the surface. Since the local immersion probe described in Section 4.2 applies a symmetric stress field normal to the rail surface, a reasonable first approximation for such a source is a single point force normal to the centre of the rail surface. In that case, the normal displacement at the excitation point is proportional to the applied force. According to Wilcox *et al.* [89, 110], the proportionality factor can be defined as the excitability $\tilde{E}$:

$$\tilde{E} \propto u^2 f \ , \tag{4.1}$$

where f is the frequency and u is the displacement in the power normalised displacement mode shape at the location and direction of the applied force.

By calculating excitability values for all modes over a range of frequencies (here between 190 kHz and 300 kHz) and comparing their maximum values, the seven most significant symmetric surface wave modes of the new rail section (Figure 4.5a) were identified (”Symmetric” refers to the vertical displacement field being symmetric with respect to the plane of symmetry of the cross-section). For simplicity they will be referred to in the following as SS_n $(n = 1, ..., 7)$.

The same procedure was applied to identify antisymmetric surface modes (AS_n) of the new rail, based on excitability values for a single point force 10 mm off the centre line, and the surface modes WS_n of the worn rail (cross-section shown in Figure 4.5b).

4.3.3 Comparison of dispersion curves with experiment

To verify the modelling and surface wave mode extraction procedure, the dispersion curves of SS_n (n=1,...,7) were superimposed on the experimental data presented before (see Figure 4.4). As Figure 4.8 shows, the dispersion curves match very well the grey areas of the 2D-FFT, thus confirming the validity of the model and the identified modes. The dispersion curves of SS_1 to SS_4 are located closely together within the dominant region in the 2D-FFT plot. Their influence cannot be separated due to resolution limits but they all seem to be significantly present in the excited signal. SS_5 appears to be present at frequencies above about 220 kHz, SS_6 mainly below that frequency, whereas SS_7 contributes over the whole bandwidth of the excitation signal. The additional grey areas in the 2D-FFT plot correspond to higher order modes. Since standard material properties have been assumed in the FE model, there is a slight mismatch to the rail steel properties in the experiment. For this reason, the group velocity of all surface modes shown, i.e. the slope of their dispersion curves in Figure 4.8, appears to be marginally (about 1%) different from the experimental 2D-FFT data.

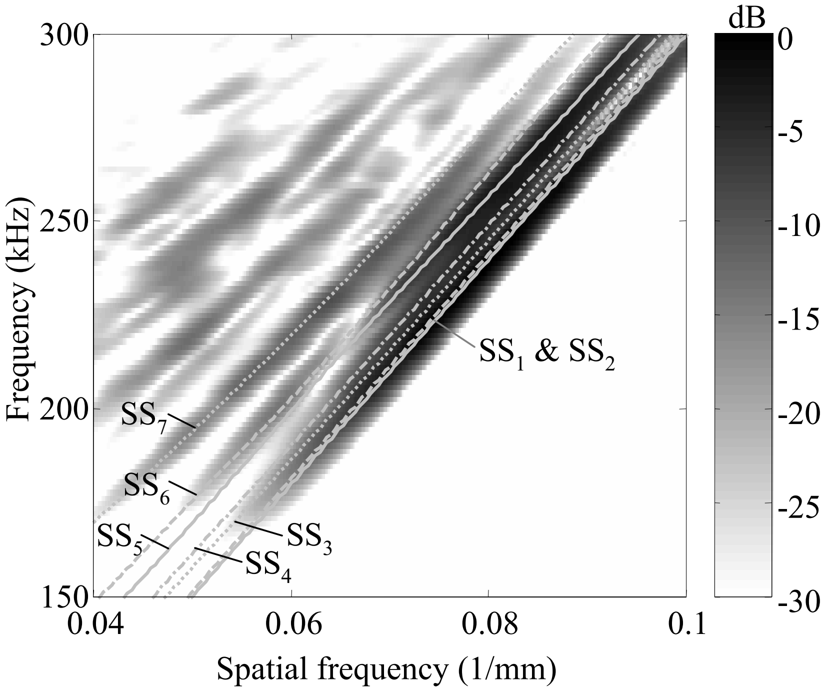

Figure 4.8: *Dispersion curves of the 7 most significant symmetric surface modes superimposed on 2D-FFT of experimental data (magnified section of Figure 4.4).*

4.4 Strain energy distributions and group velocities of surface wave modes

In order to assess the suitability of the identified surface wave modes for inspection purposes, it was necessary to analyse their strain energy densities and group velocity dispersion curves. The average strain energy density u_S allows us to determine in which areas of the cross-section a mode is likely to have a high sensitivity to defects. It is defined as

$$u_S = \frac{1}{4}\mathbf{S}^*:\mathbf{c}:\mathbf{S}\ , \tag{4.2}$$

where $\mathbf{S}$ is the strain tensor and $\mathbf{c}$ the stiffness tensor [77, 111].

The group velocity c_g is defined as

$$c_g = \frac{\partial\omega}{\partial k}. \tag{4.3}$$

One way to determine c_g from the numerically obtained dispersion curves is by

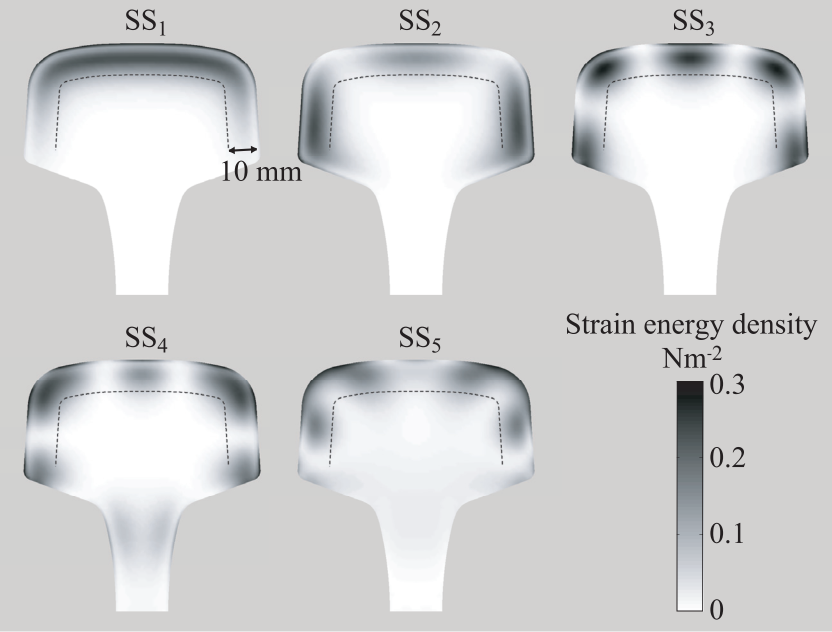

Figure 4.9: *Strain energy density of selected symmetric modes at 200 kHz.*

approximating the partial derivative with a difference quotient. However, the result can be very noisy which is why a different approach was chosen. The dispersion curve at each given frequency was approximated by a second order polynomial which was fitted to three adjacent points. The derivative of this, i.e. the approximation of the group velocity, could then be determined analytically.

Having determined the group velocity c_g, the average waveguide power P_{AV} of a mode can be calculated just from the mode shape without determining the stress field:

$$P_{AV} = c_g \int_{CS} \frac{\rho}{2} \omega^2 \mathbf{u} \cdot \mathbf{u}^* dxdy, \tag{4.4}$$

where CS is the cross-section of the waveguide (in the $x - y$ plane) and $\mathbf{u}$ is the displacement mode shape [76].

Figure 4.9 shows the strain energy density distributions for the power normalised mode shapes of the symmetric modes SS_1 to SS_5 at a frequency of 200 kHz. The strain energy density at the bottom of the half rail sections shown is negligibly small. It can therefore be assumed that the mode shapes are identical to those of a full rail section. A penetration depth of at least 10 mm was desirable in order to obtain

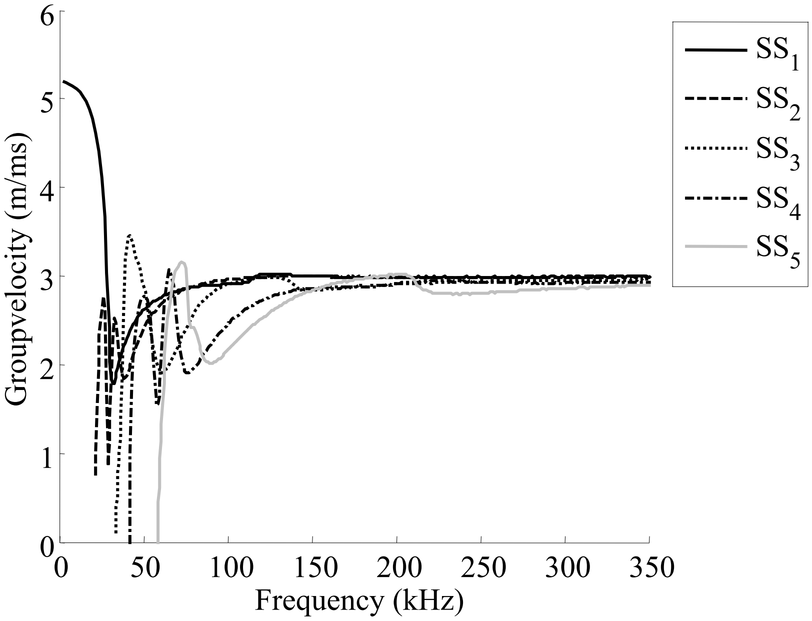

Figure 4.10: *Group velocity dispersion curves of the 5 most significant symmetric surface modes.*

an increasing reflection coefficient with defect depth up to a depth of about 10 mm; this depth is shown in all the plots by a dashed line. All modes shown are confined to a region below about this depth, but they exhibit a different number of nodes and anti-nodes around the perimeter, with SS_1 being the lowest order mode. The energy density distribution along a line normal to the surface is similar to that of a pure Rayleigh wave: the maximum value can be found at the surface (or "skin") and a second peak is located at a depth of about half the wavelength. Since the strain energy density of mode SS_1 is evenly distributed along the surface, it is best suited for inspection purposes.

The group velocities of SS_1 to SS_5 converge towards the Rayleigh wave velocity of about 3 m/ms at high frequencies, as can be seen in Figure 4.10. However, the magnified plot in Figure 4.11 of the frequency range between 100 and 350 kHz reveals a more complex situation. The group velocities of SS_1 and SS_2 converge to the same value of about 2990 m/s at around 150 kHz and stay essentially constant at frequencies higher than that, i.e. they are non-dispersive. The dispersion curves of SS_3 and SS_4 are very similar and rise fairly monotonically from 150 kHz onwards.

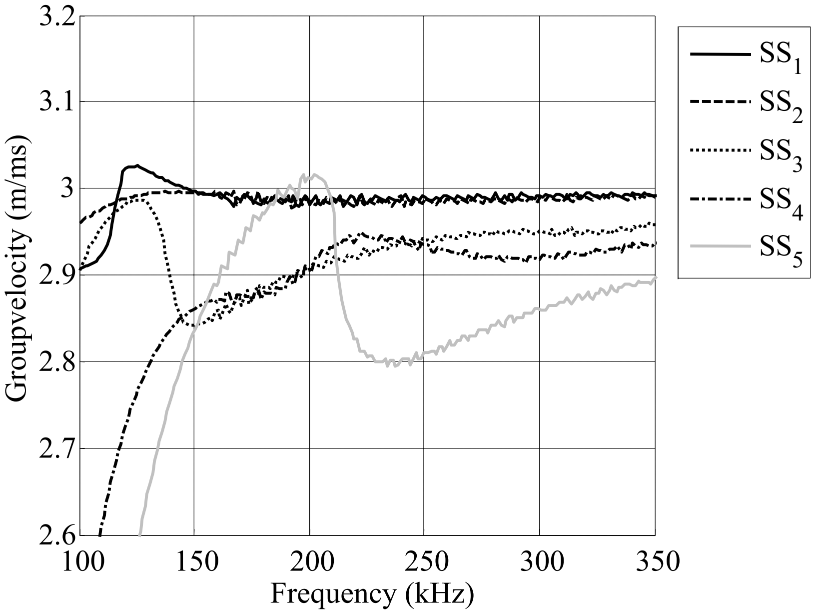

Figure 4.11: *Magnified section of Figure 4.10, group velocity dispersion curves of the 5 most significant symmetric surface modes.*

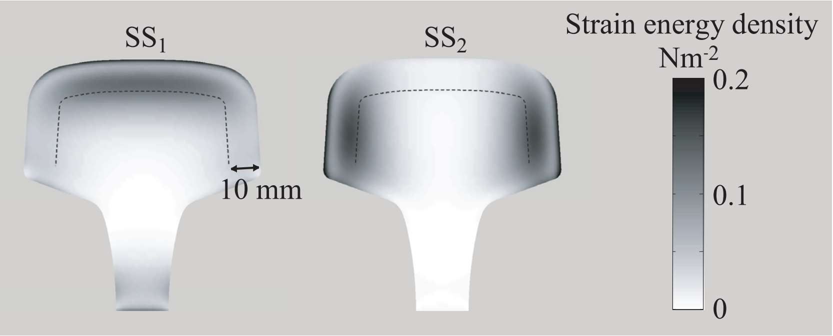

Figure 4.12: *Strain energy density of selected symmetric modes at 120 kHz.*

At 200 kHz their group velocity is still about 3% lower than that of SS_1 and SS_2 which reduces to about 1.5% at 350 kHz. The group velocity of SS_5 reaches a value of about 3 m/ms at 200 kHz, then drops to 2.8 m/ms around 230 kHz and converges towards the Rayleigh wave velocity even more slowly than SS_3 and SS_4. Note that the noise in the magnified dispersion curves is an artefact from the calculation of the group velocity.

The behaviour of SS_1 and SS_2 is similar to the fundamental modes of a rectangular bar with dimensions similar to the railhead. This becomes more obvious when

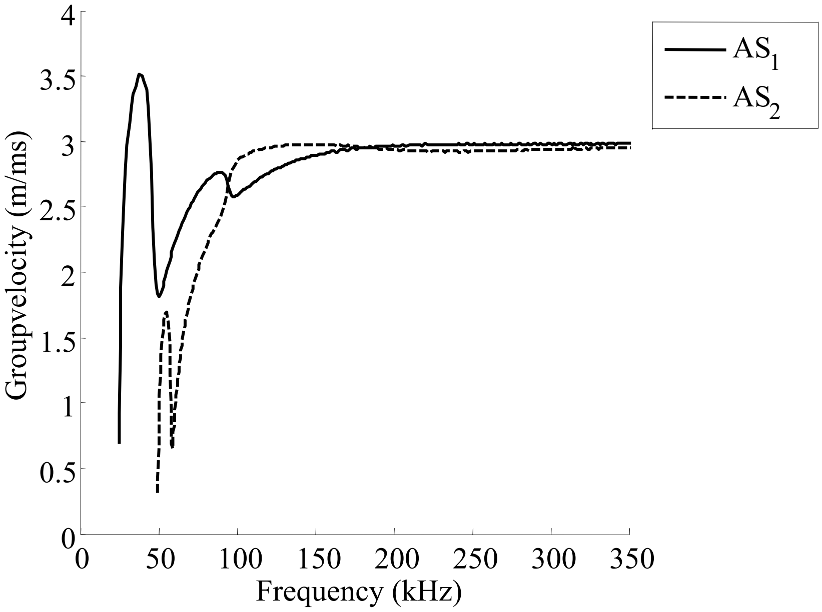

Figure 4.13: *Group velocity dispersion curves of the 2 most significant antisymmetric surface modes.*

plotting the strain energy density for these two modes at 120 kHz, see Figure 4.12 (note that the greyscale differs from Figure 4.9). At such low frequencies SS_2 does not exhibit any significant strain energy density at the top of the railhead, but only at the sides. SS_1 has significant strain energy density at the bottom of the modelled cross-section, thus starting to resemble a fundamental plate mode, too. This is partly an artefact of the reduced model, since for a full rail, due to the increased thickness, this would probably occur at lower frequencies. In this case, the mode of the reduced rail section model might therefore have a slightly different mode shape compared to the full section. Both modes, SS_1 and SS_2 have a larger penetration depth than at 200 kHz (see Figure 4.9 for comparison).

The group velocities of the two most significant antisymmetric surface wave modes AS_1 and AS_2 converge to the Rayleigh wave velocity at high frequencies, too (see Figure 4.13). It was found that the higher order modes are highly dispersive and are therefore not suitable for inspection purposes.

The strain energy density distributions of the two most significant antisymmetric modes are shown in Figure 4.14. As expected, both AS_1 and AS_2 exhibit significant

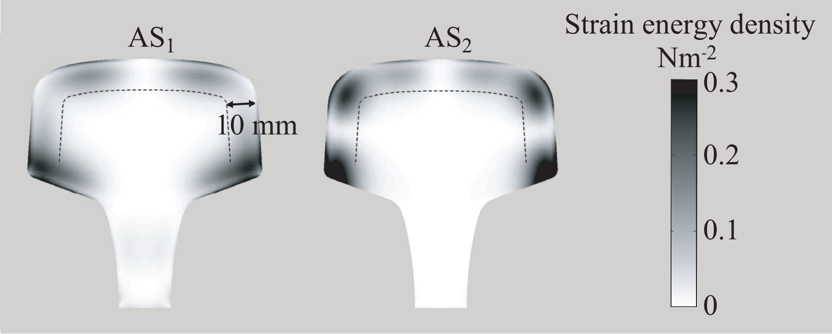

Figure 4.14: *Strain energy density of selected antisymmetric modes at 200 kHz.*

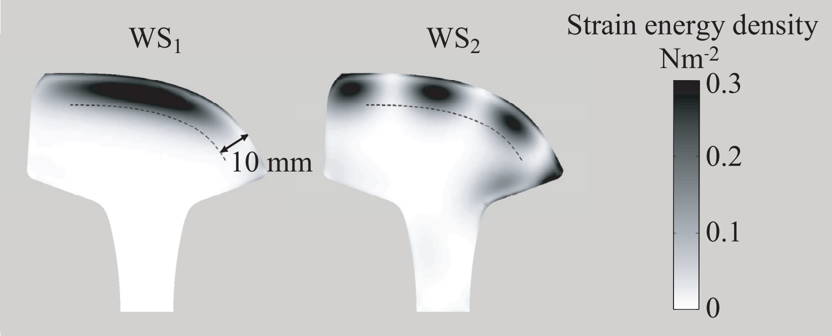

Figure 4.15: *Strain energy density of selected modes of an extremely worn rail at 200 kHz.*

strain energy density towards the rail head corners, rather than along the symmetry axis of the cross-section. Unfortunately, the strain energy density of both modes is high at the bottom corners of the rail head and fairly low close to the running surface. Therefore these modes do not seem very suitable for inspection purposes. However, they may be generated by mode conversion at defects and thus could interfere with symmetric mode signals.

An important issue for the use of surface wave modes as an inspection tool is the effect of cross-section changes due to wear on mode shapes and velocities. The cross-section shown in Figure 4.5b was therefore analysed as a worst case scenario and the extracted modes were matched up with those from the new rail. Figure 4.15 shows the strain energy distributions of the two most dominant surface modes in the worn rail for normal excitation on the centre of the rail head. It is obvious that the mode

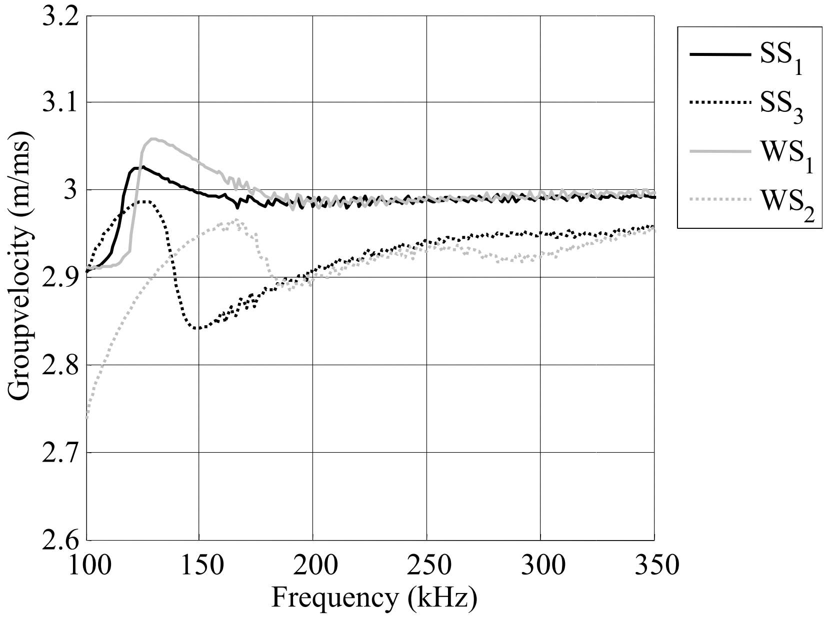

Figure 4.16: *Group velocity dispersion curves of the 2 most significant surface modes of the worn rail in comparison to the symmetric modes SS_1 and SS_3.*

denoted WS_1 is equivalent to the symmetric mode SS_1 in the new rail, whereas WS_2 corresponds to SS_3 (see Figure 4.9 for comparison). Compared to SS_1, the strain energy density of WS_1 is slightly more concentrated in the centre of the railhead and decays marginally more towards the sides. However, despite the substantial change of cross-section there does not seem to be a significant qualitative difference between WS_1 and SS_1 in terms of sensitivity to defects in the gauge corner. The comparison of the dispersion curves of the corresponding modes in Figure 4.16 shows that the group velocities of SS_1 and WS_1 are virtually identical above a frequency of about 180 kHz. This confirms the suitability of SS_1/WS_1 for inspection purposes.

The smaller radii of curvature of the analysed worn rail section also support many other surface modes which are strongly confined to these corners. Such modes have been extensively discussed in the context of topographic wave guides for SAW devices (see for example Oliner [37,38] and Krylov [40]). However, they are not suitable for inspection purposes since they do not cover the cross-section area of interest and would depend strongly on the amount of wear.

4.5 Mode shape verification using 3D FEM simulations

As described in Section 4.3.1, the guided wave modes were obtained from an axisymmetric FE model which represents the rail as a curved rather than a straight wave guide. It was therefore necessary to verify that the model radius had been chosen to be large enough and thus the effect of curvature on the computed mode shapes is negligible. Since the effect would be significant only at high wavelength-to-radius ratios, it was only necessary to establish a low frequency limit. For this purpose, the propagation of a pure surface wave mode was initiated and monitored in a 3-dimensional straight FE model of the rail head using the mode shapes from the axisymmetric model.

A very efficient way to excite a pure mode in a FE model of a wave guide is to apply an appropriate displacement input at all nodes of the front cross-section. However, since a tone burst signal has a finite frequency bandwidth, the change of the mode shape with frequency as well as position in the cross-section has to be taken into account at each excitation node [112]. This so-called ”Exact Mode Shapes” [113] technique consists of three steps. Firstly, a discretised frequency spectrum of the desired excitation waveform is calculated using a discrete Fourier transform. For all frequencies with significant amplitudes the power normalised displacement profiles (mode shapes) have to be available. Secondly, the frequency components of the signal are multiplied by the appropriate displacement profiles and finally summed up, thus generating a frequency spectrum for all three spatial directions at each node of the waveguide cross-section. Thirdly, an inverse Fourier transform is performed on all spectra to obtain time domain signals for each excitation node which can be applied as input displacement-time functions in the FE model.

The model was set up in the FE package ABAQUS utilising its time marching ”Explicit” solver and linear 8-node brick elements. Since the intention was to study the propagation of a symmetric mode, only half of a 400 mm long railhead section was modelled and appropriate symmetry conditions were applied, see Figure 4.17a.

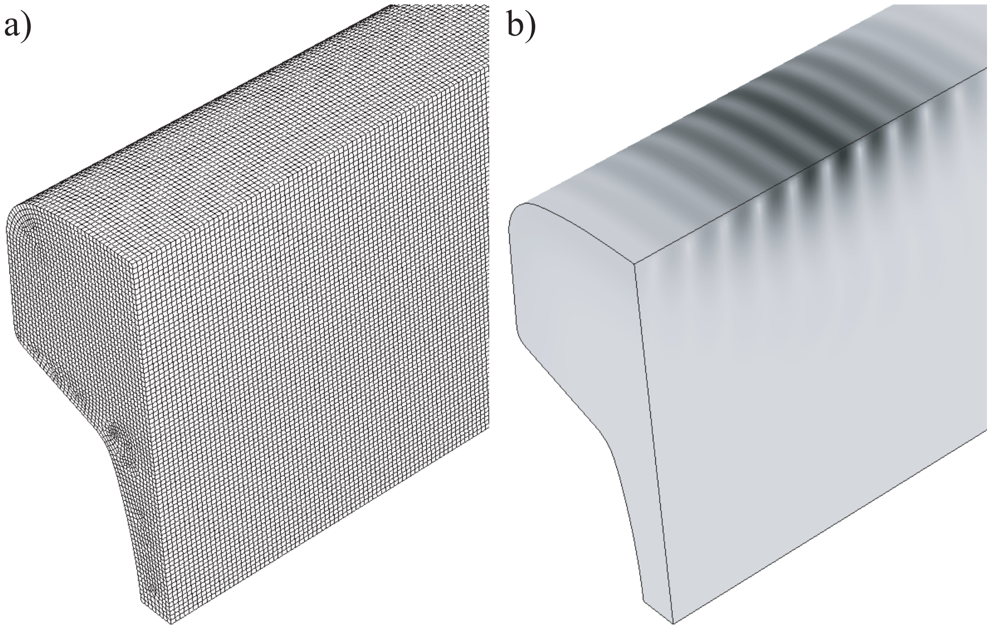

Figure 4.17: *Exact mode shape excitation of symmetric surface wave mode* SS_1*. (a) Mesh of FE model. (b) Snapshot of FE simulation after a propagation time of 40* μ*s. Displacement magnitude in linear grey scale (dark: maximum, light: zero).*

The cross-section meshing was very similar to the one utilised in the axisymmetric 2D model presented above (see Figure 4.5) with an element size of approximately 1 mm. However, since the use of the automatic meshing tool in the 3D model led to a small difference of node positions compared to the mesh of the mode shapes, a 2-dimensional interpolation was performed on the excitation signals before applying them as boundary conditions to the front face nodes. A Gaussian windowed toneburst at a centre frequency of 200 kHz with a bandwidth of 20% was used as the excitation signal resulting in significant amplitude contributions (> -40 dB) between 120 and 280 kHz. As opposed to a Hanning windowed tone burst, this has the advantage of not exhibiting any side lobes in the frequency domain and therefore manipulation of only a limited bandwidth for the exact mode shape excitation does not introduce significant errors.

Figure 4.17b shows a snapshot of the model after a propagation time of 40 μs with the displacement magnitude plotted as a linear greyscale. The form of the displacement is very similar to the input with no sign of interference from other modes developing. The maximum signal envelope of the vertical displacement was monitored along the top edge of the symmetry plane and found to be constant within ±2%. This confirms that the mode shapes generated with the axisymmetric model are not significantly affected by the curvature for frequencies above 120 kHz and can therefore be considered identical to those of a straight waveguide.

4.6 Summary

In this chapter, the properties of surface wave modes in rails were investigated. The main aim was to determine the low frequency limit at which there exists a non-dispersive surface mode with a high penetration depth suitable for inspection purposes. Additionally, information on other surface modes with similar propagation was needed in order to avoid multiple mode excitation which can lead to wrong signal interpretation. This issue was illustrated using a relatively simple experiment and showing that signal arrivals at low frequencies around 250 kHz typically consist of a large number of concurrent interfering guided wave modes rather than a single Rayleigh wave as commonly assumed in other publications. Their dispersion curves were determined using axisymmetric FE models for new and worn rail sections up to a frequency of 350 kHz and the relevant symmetric and antisymmetric surface wave modes were extracted using excitability considerations. The dispersion curves showed excellent agreement with the 2D-FFT of the experimental data so that it could be confidently assumed that the reduced cross-section model of the rail head used here is a sufficiently accurate representation of a real rail.

It was found that the symmetric mode SS_1 has promising characteristics for inspection purposes, since it has an evenly distributed strain energy distribution at the surface and is essentially non-dispersive. It maintains these qualities down to frequencies as low as 180 kHz, even if the rail is heavily worn. It appears therefore that this is the low frequency limit at which a maximum penetration depth of the surface mode can be achieved without dispersion. To reduce the sensitivity to shallow features it is beneficial to work at frequencies as low as possible; hence, it is feasible to go even slightly below 200 kHz, rather than stick to the initially estimated 250 kHz.

However, it appears to be a challenging task to separate SS_1 from the large number of other surface wave modes with very similar propagation characteristics all of which are excitable from the railhead surface. Most of them are slightly or considerably dispersive, but at least one mode (SS_2) has the same group velocity as SS_1, thus making mode separation extremely difficult. Even if only one mode is excited, others will be generated by mode conversion at defects and all the modes will interfere, thus making the received amplitude position-dependent, as shown in Figure 4.3. The detection of critical defects seemed therefore feasible, but defect sizing would be very difficult.

Chapter 5

Selective excitation and reception of surface wave modes

5.1 Background

In Chapter 4, the surface wave mode named SS_1 was found to be suitable for inspection purposes in a frequency range around 200 kHz. However, a large number of similar guided wave modes with slightly different propagation properties is excitable as well from the rail surface in the same frequency range. The initial experiment in Section 4.2 showed that the interference of these wave modes could cause severe difficulties for correct signal interpretation. In order to avoid coherent noise caused by the excitation and reception of unwanted modes, it was therefore necessary to develop a setup with high mode selectivity.

The optimisation of mode selectivity is a general issue in the context of guided wave inspection. It can be achieved by matching the excitation to (a) the displacement or stress distribution (i.e. the mode shape) of the desired wave mode around the cross-section perimeter and/or to (b) the wave propagation characteristics in the direction of interest. There are some common approaches to realise this, but typically the methods have to be customised for each type of waveguide and application.

Wedge transducers and linear arrays oriented along the propagation direction (e.g. interdigital transducers, comb transducers etc.) follow the second approach (b) and allow some degree of control over excited and received wavelengths. In the case of a wedge transducer the wedge angle determines the projected phase velocity c_p of the wave mode according to Snell's law [32, 114, 115]. Such a probe can transmit and receive different wavelengths for different frequencies, but it can only be used for wave modes with negligible dispersion in the frequency range of interest. In the case of a comb transducer the element spacing along the waveguide fixes the wavelength of the excited wave mode. This usually means that the transducer can only be used to excite a certain mode at one frequency for which the element spacing has been optimised (it may also be used for other modes at other frequencies). For linear arrays in general the mode selectivity can be adjusted by changing the element spacing or applying phase delays to the excited and received signals of individual elements [116–119]. The phase delay can be optimised to match the propagation properties of different modes which makes the use of linear arrays very flexible. The wavelength selectivity at a given frequency of wedge transducers as well as linear arrays increases significantly with increasing probe length. The minimum probe length depends on the application, but usually at least 3-5 wavelengths are required for satisfactory mode control [120]. For this reason, the strategy of matching wave characteristics in the propagation direction is mostly applied at relatively high frequencies and small wavelengths such that the transducer size can be kept reasonable. In References [116, 117] and [119] for example, linear array probes have been utilised on plates at frequencies above 1 MHz and wavelengths smaller than 6 mm.

For long range (up to around 100 m at frequencies below 100 kHz) and mid range inspection (up to about 5 m, below 1 MHz) the wavelengths are larger (tens of millimetres) such that the transducer would need to be unacceptably large to provide sufficient mode selectivity. The standard strategy for pipes and other beam-like structures with good access from all sides around the cross-section is therefore to clamp a ring of transducers around the perimeter of the waveguide and match the mode shape on the surface. The combination of both strategies, i.e. utilising multiple adjacent rings and phase-delayed signals, improves the mode selectivity further. Following this combined approach, inspection systems have been developed for example with two adjacent rings (long range) [23, 121] and four rings (medium range) [118] for pipes and six rings for rails (long range) [23, 121].

For the mid range problem investigated in this thesis at frequencies around 200 kHz and wavelength of about 15 mm it was necessary to combine both strategies as well. The probe was supposed to be integrated in a moving setup at a later stage which would only have access to the top of the railhead since lower parts could be obstructed by switch blades, fasteners, electrical contacts etc. The option of mode shape matching could therefore be applied only to a small part of the cross-section perimeter. To improve the mode selectivity further, it was therefore necessary to match the characteristics of the mode along the rail as well. As was seen in Section 4.2, using a local immersion probe as a realisation of the wedge principle was not sufficient. Due to the utilised low frequencies the probe would need to be extremely long to achieve a reasonable mode selectivity. Since it did not appear feasible to realise this in terms of probe hardware, a software algorithm was developed which can be applied at the signal postprocessing stage.

In the following, the probe design will first be explained and afterwards two signal processing methods to optimise mode selectivity will be explored. The aim of the first approach was to match the desired mode shape on a limited area across the railhead via array focussing and apodisation. The second approach is a spatial averaging method which exploits the successively acquired data gathered by scanning the probe along the rail and which acts like a filter in the wavenumber-frequency domain. The potential and limitations of both methods is discussed and a resulting procedure for experiments with defects is derived.

5.2 Probe design

As discussed in Section 2.2, it was planned to utilise a local immersion wheel probe for signal transmission and reception. The tyre of such a probe would be similar to those already used in conventional rail inspection units with enough flexibility to

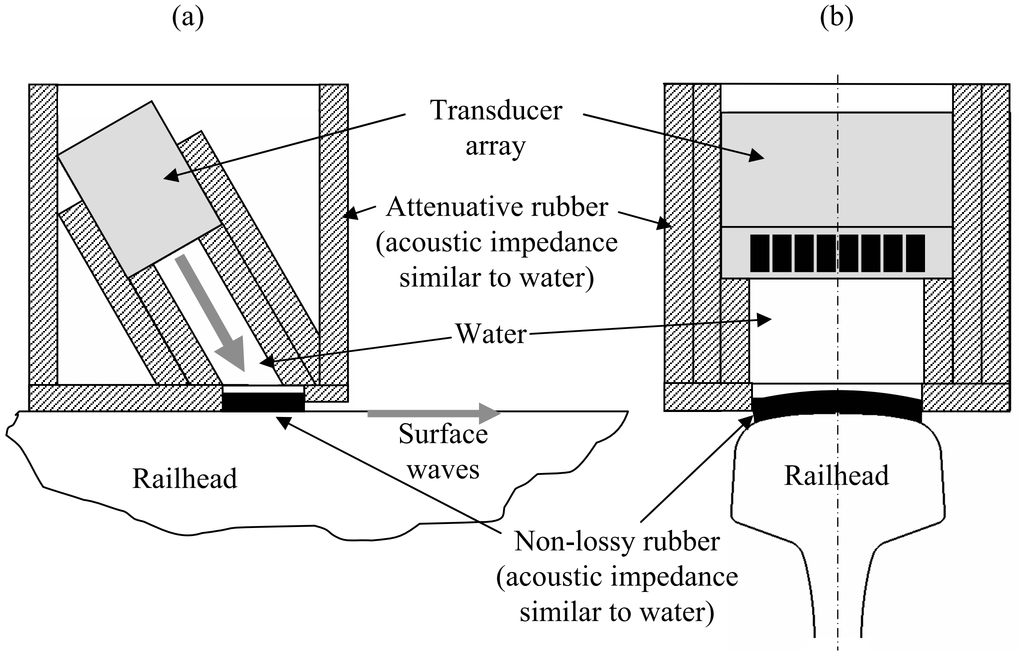

Figure 5.1: *Local immersion probe used for surface wave excitation.*

conform to the curved railhead surface. Low-loss rubber which matches the acoustic impedance of water is well suited as the tyre material, as has been shown for wheel probes on plates [122]. The probe would cover a considerable part of the railhead width and hence ensure a large excitation area on the railhead surface.

A rectangular rather than a circular transducer covering the full rail width would be ideally suited to excitation of the desired mode SS_1 shown in Figure 4.9. For this purpose, an 8 element linear array with a centre frequency of 250 kHz covering the full rail head width was commissioned from IMASONIC. As opposed to a monolithic transducer, this had the advantage that all the elements could be driven simultaneously to create a uniform beam and also, that experiments with apodisation and focussing could be carried out. Unfortunately, the supplier of the transducer array took over 12 months to produce a satisfactory array. In order to avoid further delays while the transducer was incorporated in a wheel, the design of the local immersion system of Figure 3.5 was modified to accommodate the array. This meant that the final version slid rather than rolled along the rail but this worked very satisfactorily and was used both in the laboratory and at facilities of the Health and Safety Laboratory and ESR Ltd.

Figure 5.1 shows a sketch of the final design. The transducer array was angled at 30° and located inside a casing filled with distilled water. The active area of the transducer elements was determined by measuring the surface displacement of the activated array with a laser vibrometer and found to be about 7 mm x 15 mm per element, the active area of the whole array being 65 mm wide. The stand-off distance of the transducer array to the rail surface was chosen to be about 65 mm to avoid overlap of received signals and electrical breakthrough and reverberations of the excitation signal. The casing consisted of 10 mm thick sheets of ultrasonically absorbent rubber NPL Aptflex F28 [83] in order to damp reverberations from the probe walls. For the same purpose, two layers of absorbent Aptflex rubber were used to form a tight water channel between the active area of the array and the contact patch at the bottom. The contact patch was 60 mm wide, 25 mm long and 5 mm thick and consisted of the non-lossy rubber initially intended to be used as the tyre material. Due to the increased curvature towards the railhead corners, a wider excitation and reception area across the rail head did not appear feasible. For good coupling of the contact patch it was necessary to wet the rail surface with a drop of water. The size of the contact patch was chosen to simulate that of a wheel probe. By doing this it would be easier to transfer the experience gathered with this sliding prototype to a wheel probe potentially to be developed in the future.

The simplest way of operating the array would be to run the channels in parallel, such that all channels would send and receive at the same time and the array would act as a monolithic transducer. Alternatively, the elements of the array could be excited independently. It was therefore possible to switch between all possible send and receive combinations with a multiplexer, acquire the data with an oscilloscope and test focussing and apodisation algorithms at the postprocessing stage in the computer. As discussed before, it was beneficial to excite the array at frequencies as low as possible and it was shown that the mode SS_1 would not be dispersive at frequencies as low as 180 kHz (see Section 4.6). It was decided to work with a 5 cycle Hanning windowed toneburst with a centre frequency of 200 kHz for all experiments, since this was the lowest possible output signal of the array.

5.3 Array focussing

Ultrasonic transducer arrays offer a lot of flexibility in terms of beam formation, focussing and steering and are therefore widely used in NDT and medical applications. For this project, the intention was to use focussing and apodisation of the eight array elements to match the desired surface wave mode shape on the rail surface. This should optimise the excitation and reception of the mode SS_1 (see Figure 4.9) and suppress unwanted modes. Since the curvature of the rail surface is not constant it was difficult to analytically determine the appropriate delay laws and apodisation factors. For this reason, a reverse engineering approach was taken using FE simulations. The idea was to excite only the desired mode in a rail model and receive this mode with a model of the probe. Reversing the received signal in time should then result in the optimum excitation signal for the probe to excite the desired mode. Note that this procedure is not *time reversal* in the strict sense, which requires the full field to be captured. In this case, only a minor part of the surface mode leaks out of the real into the probe and a further limited portion is received by the array inside the probe. It is therefore obvious that the reversed signal cannot generate a pure mode. However, this method appeared to be a good technique to determine the optimum excitation within the given limitations. The procedure is discussed in the following.

5.3.1 Finite Element simulations

For the simulations, the same 3-dimensional FE model of the rail and the exact mode shape excitation procedure were utilised which were already discussed in Section 4.5. The modelled rail section was 400 mm long consisting of linear solid brick elements with approximately 1 mm side length. Only half of the railhead was modelled and symmetry boundary conditions were applied to reduce the model size. In addition to the rail from Section 3.5, a model of the local immersion probe was set up and and coupled to the rail surface, see Figure 5.2a-c. The model considered only the water part of the probe and consisted of linear acoustic elements with the acoustic pressure

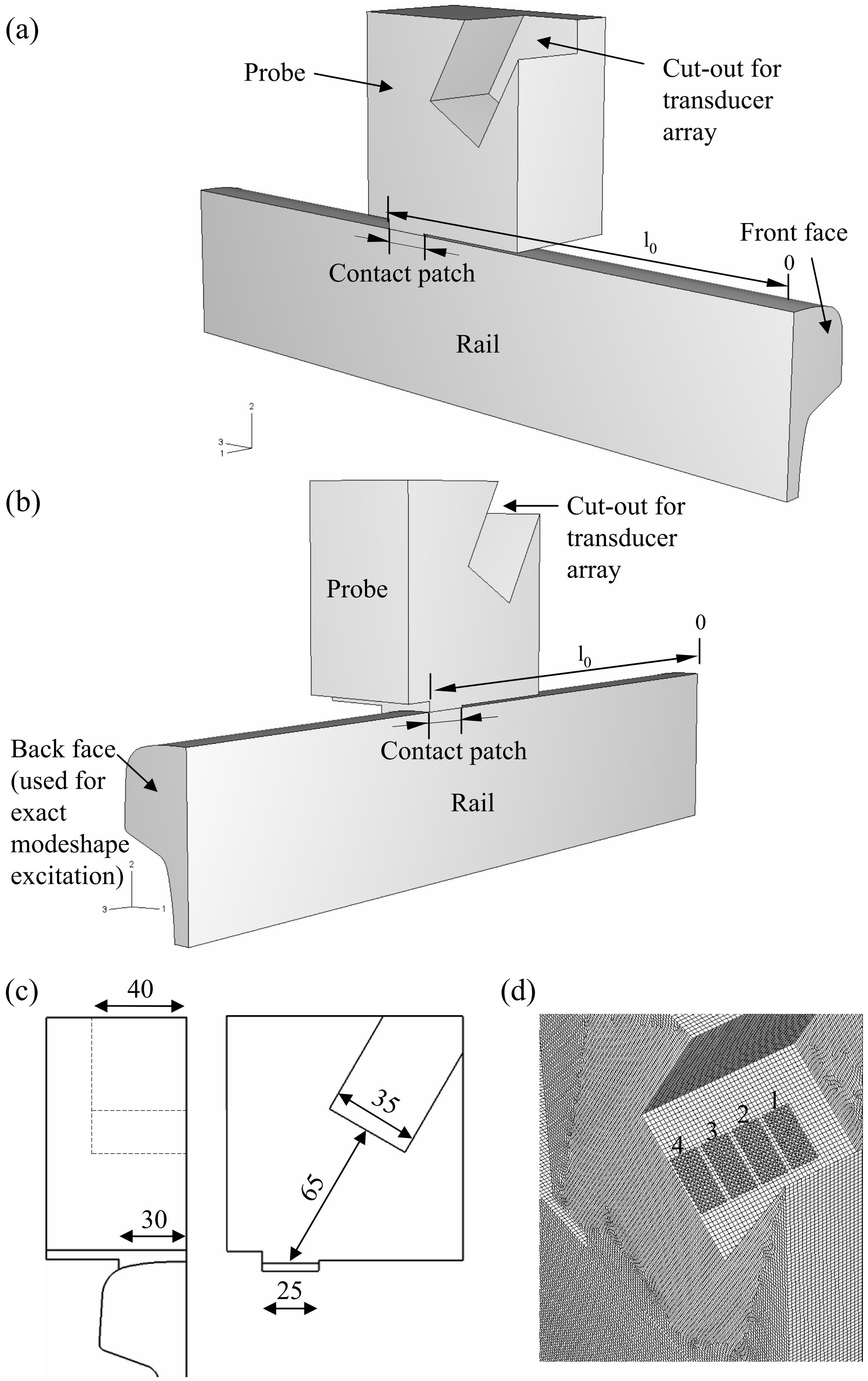

Figure 5.2: *FE model of probe on rail. (a),(b): different views of model geometry; (c): sketch of probe model, dimensions in mm, (d): zoom into FE mesh, transducer cut-out in probe with node sets representing transducer elements 1-4.*

as the sole degree of freedom. The element side length was approximately 1 mm, which is equivalent to about 6 elements per wavelength (the minimum suggested by ABAQUS [123]). The mesh was therefore relatively coarse, but it was found to perform satisfactorily. It was an acceptable compromise in order to limit the model size which was in the order of 4 million degrees of freedom. Since the impedance of all rubber components of the real probe was matched to water, the walls as well as the contact patch were simply modelled as water in the FEM simulation. Attenuation of the Aptflex rubber sheets was not considered. All dimensions were kept as close to the real probe as possible, see Figure 5.2c. Since the probe was symmetric, only half of it was modelled. The boundary condition for full reflection was set in the symmetry plane and all other boundaries of the probe apart from the contact patch, which was coupled to the rail surface. The transducer array was represented by a cut-out in the water "block". Four rectangular sets of nodes in this cut-out represented the array elements, see the highlighted areas "1"-"4" in Figure 5.2d. The received signal of each transducer "element" (i.e. node set) could then be generated by calculating the mean of the monitoring signals from all nodes in each set. To excite a transducer "element", the same pressure signal was applied to all nodes of each set.

For the first simulation, the probe was located in the centre of the rail surface ($l_0 = 250$ mm) to avoid any near field effects from the ends, see Figure 5.2a-b. Exact mode shape excitation (see Section 4.5) of the mode SS_1 was then applied to the "back" face of the rail (see Figure 5.2b). A Gaussian windowed toneburst at a centre frequency of 200 kHz with a bandwidth of 20% was used as the excitation signal (note the Gaussian window was preferred since it does not cause sidelobes in the frequency domain, see Section 4.5). Figure 5.3 shows four snapshots of the model symmetry plane at different points in time during the simulation. The surface wave mode propagated along the rail (Figure 5.3a) and underneath the probe where it excited bulk waves in the probe (Figure 5.3b). These propagated at the expected angle of 30° towards the probe (Figure 5.3c) and impinged on the node sets representing the transducer elements. The received signals of all transducer "elements" (i.e. the averaged monitoring signals of each node set) are shown in Figure 5.4. The further

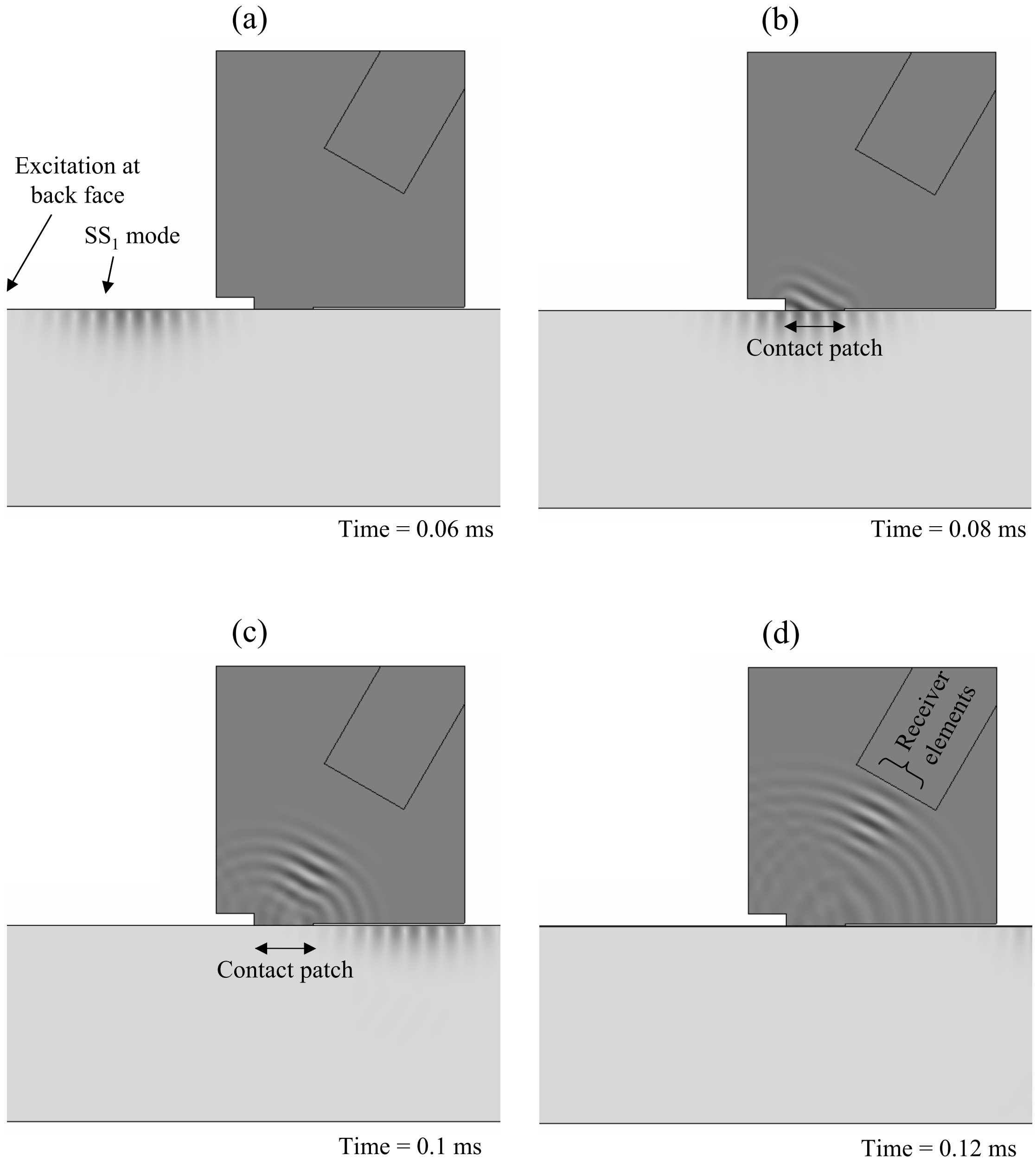

Figure 5.3: *Exact mode shape excitation at back face of rail, reception with probe. Field snapshots at different points in time in symmetry plane of FE model (shown variables: displacement magnitude for rail, pressure for water in probe).*

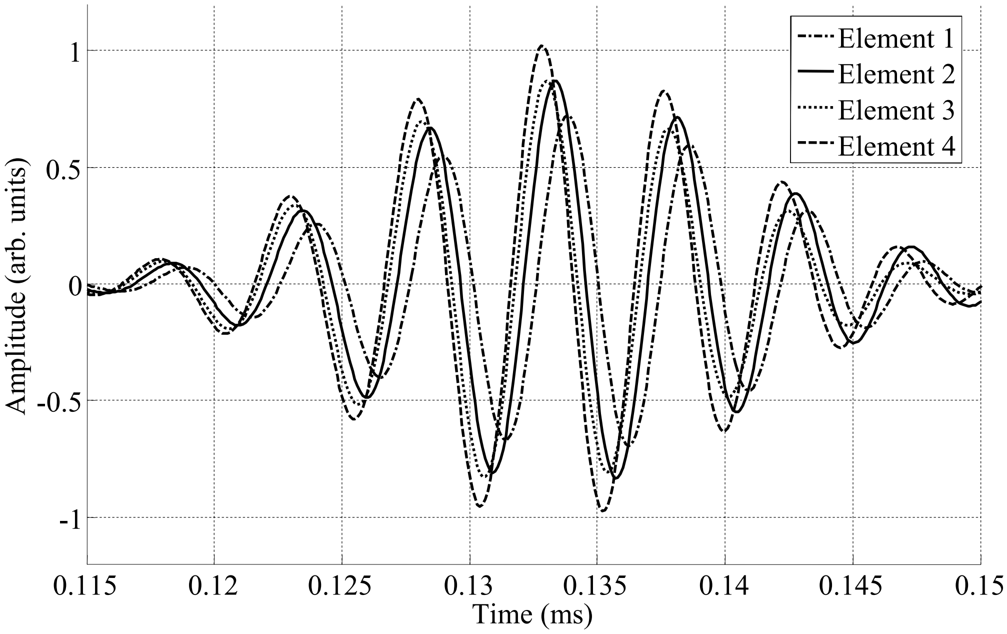

Figure 5.4: *FEM simulation utilising exact mode shape excitation of mode SS_1. Averaged received signals at node sets representing transducer elements 1-4 (see Figure 5.2d).*

away the elements are located from the rail head centreline (the farthest being element "1"), the more they are affected by the rail curvature and the increased distance between the rail surface and the transducer elements. The result is a larger phase delay and a lower amplitude of the received signal, see for example the difference between Elements 1 and 4 in Figure 5.4. If these signals were reversed in time and used to excite the elements, then they would focus the bulk wave in the water to excite the surface wave mode SS_1. Due to the limited contact area, pure mode excitation would be extremely unlikely. However, the excitation would be optimally matched to the desired mode in the available contact patch. The efficiency of this approach was evaluated in two further simulations.

For the second simulation, the probe was positioned closer to one end of the rail model ($l = 60$ mm). The received signals from the previous simulation were reversed in time and applied as excitation signals to the node sets representing the transducer elements. The excited signals in the rail were monitored along the centre line of the rail surface (in the model: the upper edge of the symmetry plane). Figure 5.5 shows four snapshots of the model symmetry plane at different points in time during

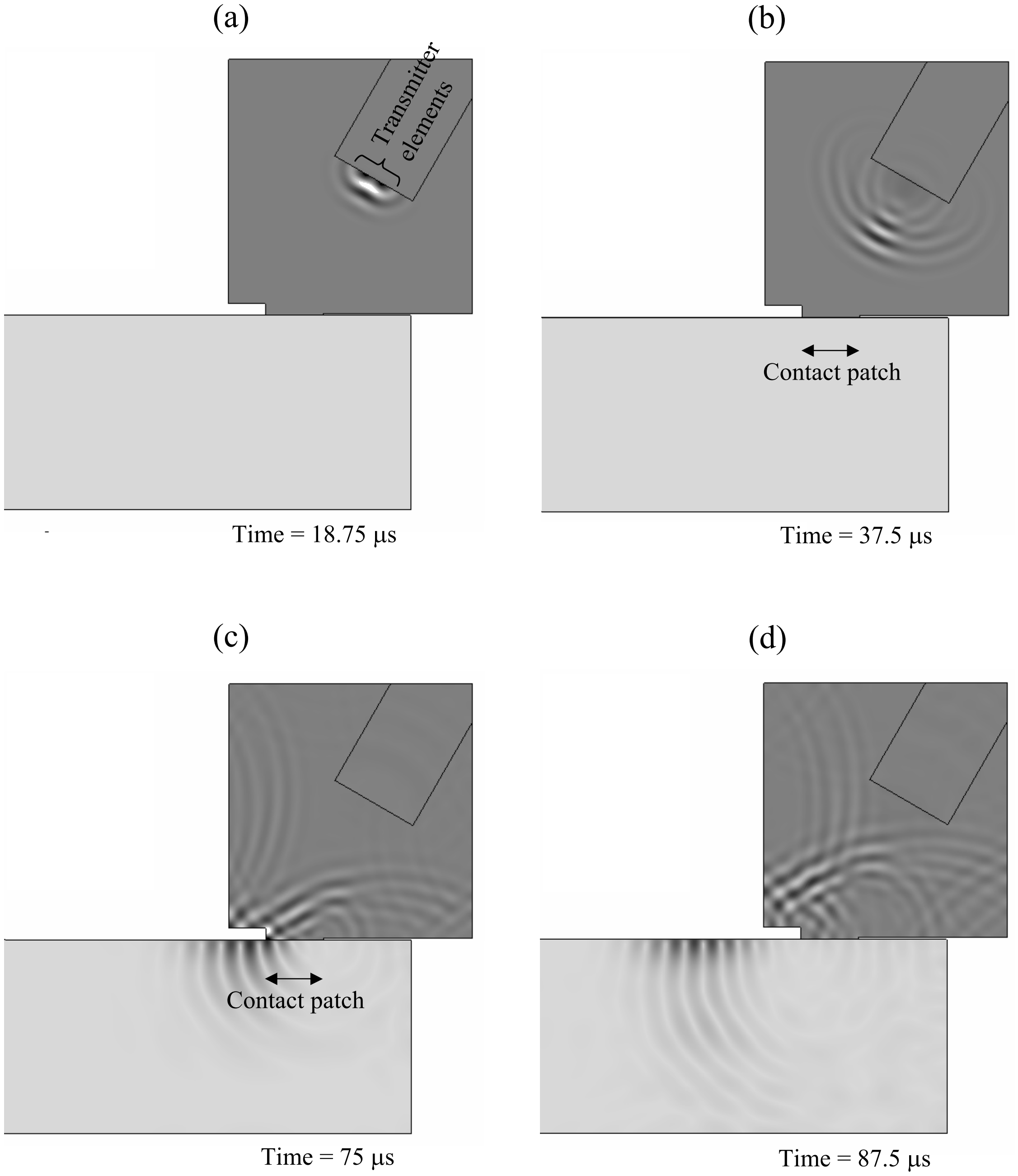

Figure 5.5: *Excitation with probe using array focussing. Field snapshots at different points in time in symmetry plane of FE model (shown variables: displacement magnitude for rail, pressure for water in probe).*

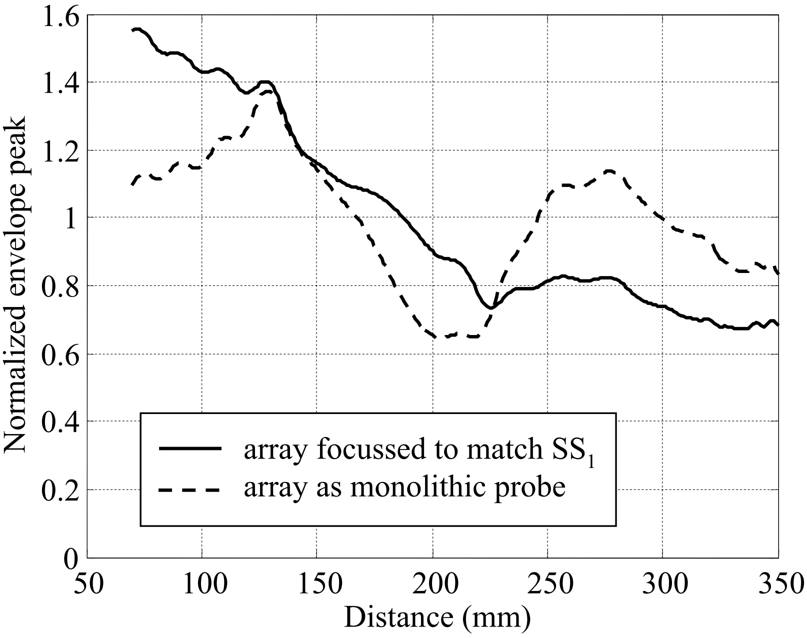

Figure 5.6: *Comparison of envelope peaks of incident wave signals monitored along rail centreline for two excitation cases. Each graph has been normalised to its mean respectively.*

the simulation. The probe excited bulk waves in the fluid (Figure 5.5a) which propagated towards the contact patch (Figure 5.5b) where they excited waves in the rail (Figure 5.5c). However, as can be seen in Figure 5.5d, the excited wave field in the rail was more complex than that of the pure mode SS_1 in Figure 5.3a, which meant that other guided wave modes were present as well. Note that the shown complex field was not due to reverberations inside the probe; such signals were seen as well but at later arrival times and far lower amplitudes.

In the third simulation, the FE model was identical to the previous one, however, the excitation was such that the array would act similar to a large monolithic transducer. Instead of array focussing and apodisation, the transducer "elements" were simply excited in parallel by the same signal, namely a 5 cycle Hanning windowed toneburst with a centre frequency of 200 kHz. The excited signals in the rail were again monitored along the centre line of the rail surface.

The results of array focussing versus parallel transducer element excitation are compared in Figures 5.6 and 5.7. The signal envelope peak of both simulations monitored

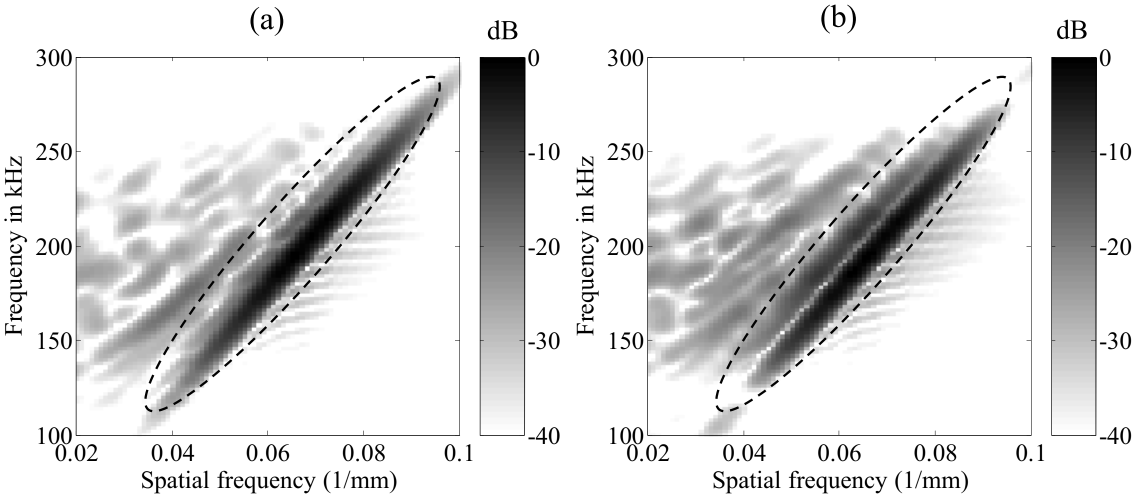

Figure 5.7: *2D-FFT on incident wave signals monitored along rail centreline for two excitation cases. (a) Array focussing to match mode SS_1. (b) Array acting as a monolithic probe (no focussing). Dashed lines indicate main area of interest.*

along the centreline of the rail versus the distance from the rail front face is plotted in Figure 5.6. Points closer than 50 mm to the end are not shown because of near field effects. The data of both curves have been normalised to their respective mean value. It can be seen that the envelope peak for both cases is not constant, but varies with distance. For the case of array focussing (solid line), the variation develops gradually and appears to be merely a decay in amplitude over the short distance of the model. However, since there was no material damping assumed, it is likely that this is just part of a beating phenomenon of interfering modes and that the amplitude would increase again over a longer distance. The amplitude variation is substantial, in a range of up to 60% of the mean value. For the case of unfocussed parallel excitation of all array elements, i.e. the array acting similar to a monolithic transducer, the amplitude varies more rapidly with distance (dashed line). The variation is still substantial, but less pronounced than that for the array focussing case, namely in the range of up to 40% of the mean.

In order to investigate this, a 2D-FFT was performed of the raw incident wave signals monitored along the railhead centreline in each model. Plots of the normalised magnitude of the 2D-FFT data for both cases are shown for comparison in Figure 5.7. In both plots the same main area of interest is indicated with a dashed line. In the case of the focussed array, there is one wide main lobe indicating a high signal content located in this area (see Figure 5.7a). The comparison with the dispersion curves in Figure 4.8 leads to the conclusion that the desired mode SS_1 was excited as well as other modes with very similar dispersion curves, such as SS_2, SS_3, SS_4. The content of modes with a slightly lower lower spatial frequency, such as SS_5, SS_6, appears to be lower. In contrast to this, there are *two* separate lobes in the indicated area for the case of the non-focussed array (see Figure 5.7b). The signal content of additional modes at lower spatial frequencies outside the marked area is higher in Figure 5.7b than in Figure 5.7a. The lobe on the right in the marked area containing the signal content of mode SS_1 appears to be narrower than that in Figure 5.7a. It seems that some of the modes with very similar spatial frequencies to SS_1 were less excited, leading to the gap between the two lobes, and other modes with lower spatial frequencies were excited more, resulting in the second lobe. This also explains the observed amplitude variation behaviour in Figure 5.6: The focussed array excited mainly modes with nearly identical wavenumbers leading to a very slowly varying interference pattern (solid line in Figure 5.6). In contrast to this, the array acting like a monolithic probe excited less unwanted modal content in the direct vicinity of SS_1, but more at lower wavenumbers, resulting in a rapidly changing interference pattern (dashed line in Figure 5.6). Thus, it can be said that the array acting as a monolithic probe was more mode selective in the direct vicinity of SS_1 than the focussed array.

5.3.2 Practical issues

The considerations so far regarding the use of array focussing and apodisation to optimise surface wave mode excitation and reception were based on FE simulations. During experiments for this project the author also encountered three major practical issues which limit the usability of this approach:

1. *Transducer quality*

   The transducer elements need to have nearly identical transfer functions such that they do not distort the applied apodisation factors and phase delays. Unfortunately, this was not the case for the array utilised in this work: the transducer elements in the centre of the array had a far higher output than those at the ends. This was a "natural" apodisation, though much more strongly than that required according to the FE simulations. Attempts to compensate for that with inverse filtering based on the measured transfer functions of each send-receive path did not work satisfactorily and also led to an increased noise level.

2. *Transducer alignment*

   The phase delays and apodisation factors were derived for the perfectly aligned FE model. As was seen in the previous section, these alterations are relatively subtle. In practice, there are always small alignment errors of the probe on the rail as well as of the array in the probe itself. It was found that slightly incorrect alignment actually increased the excitation of unwanted modes.

3. *Rail wear*

   For cross section changes due to wear the delay laws and apodisation factors would require adjustment.

5.3.3 Conclusions

The FE simulations have shown that even an optimally focussed array (based on time reversal of a received pure mode signal) does not significantly improve the excitation of the desired mode SS_1. In fact, the envelope peak varied more with distance than for the unfocussed array. The fact that very similar modes to SS_1 were excited stronger than for the unfocussed array would make it more difficult to separate the mode with an additional method. Furthermore, the problems encountered during practical implementation such as transducer quality, alignment and rail wear showed that the method is not robust enough for purpose. It was therefore concluded that there was no benefit in applying array focussing and apodisation to the signals captured by the array. Instead, it was decided to run all elements in parallel in pulse-echo mode such that the array acted like a monolithic probe. This would also speed up the data acquisition since no multiplexing was required.

5.4 Spatial averaging

The method presented in this section was developed to improve the mode selectivity of a simple, robust probe which can be moved along the wave guide. The idea behind this is to exploit the acquired scan data to match the excitation to the propagation properties of the desired mode at the signal postprocessing stage.

In the following, the general concept of the method will first be presented and its characteristics in terms of mode selectivity will be analysed using a simple analytical model. Finally, the results of an experimental test on rail will be discussed.

5.4.1 Principle

Guided waves can propagate long distances along a wave guide, usually several metres at low frequencies in non-lossy materials. If a probe is moved along the waveguide and successive measurements are taken at relatively small intervals, e.g. a few centimetres, then the inspected sections of the waveguide overlap significantly. This redundancy can be exploited to reduce the amount of unwanted guided wave modes in the received signals. The method discussed here as *spatial averaging* can be applied to any kind of waveguide on which multiple pulse-echo measurements are carried out along the propagation direction of the wave mode of interest. Note that the probe speed is assumed to be negligibly small compared to the wave speed such that the send and receive locations of the probe can be considered to be identical.

The probe is scanned along the waveguide and the pulse-echo RF signals as well as the spacing between the measurement positions are recorded. The spatial averaging process is carried out at each new measurement position. Firstly, the signals of a set number of previous measurement positions are phase-shifted using the wavenumber

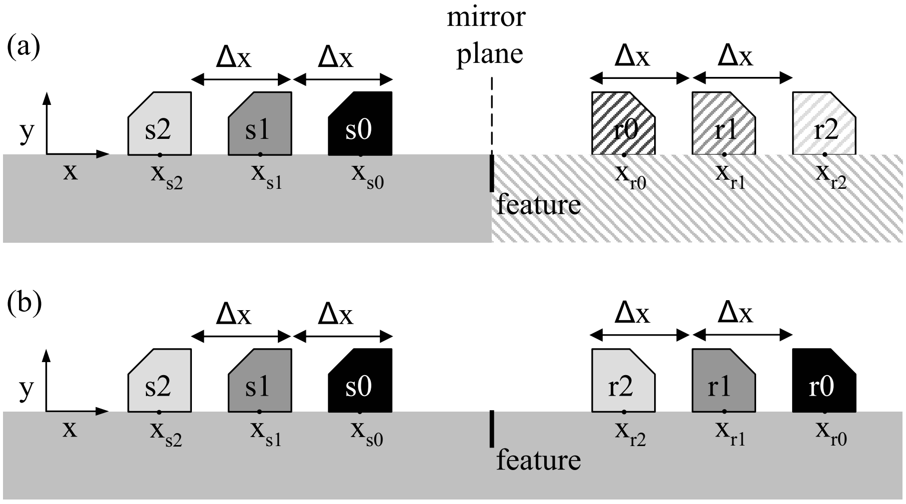

Figure 5.8: *Comparison of different probe setups regarding spatial averaging. (a) pulse-echo; (b) pitch-catch with equal distance between transmitter and receiver.*

of the desired mode such that they are synchronised to the signal of the current reference position. The phase shift is carried out in the frequency domain and is a synthetic propagation of the acquired signal from each of the measurement positions to the reference position. Dispersion can readily be taken into account. Subsequently, these phase-shifted signals are summed and result in an averaged signal for the reference position. Every new measurement position can be used as the new reference position for the spatial averaging process over a fixed number of signals, resulting overall in a moving average. The envelopes of the obtained averaged time traces can then for example be displayed in a B-scan type plot or condensed into a single mean envelope, as will be illustrated later.

In the following sections, the characteristics of the spatial averaging technique will be discussed and the differences compared to a full linear phased array will be highlighted (including the special case of a longer monolithic probe).

5.4.2 Basic model

A pulse-echo setup is considered for a probe which is scanned along a waveguide in intervals of Δx. This can also be interpreted as a pitch-catch configuration where the receiver is a mirror image of the probe using a single feature as the mirror plane, see Figure 5.8a. Multiple reflections can be accounted for by multiple superposition of this concept, however this does not change the aspects to be illustrated here. Send positions are marked by "s", receiver positions by "r" and the indices link corresponding positions (e.g. send "s0" and receive "r0"). For the reference position, the index $n = 0$ is used, positive indices $n = 1, 2, ...$ denote positions of previous measurements when moving in the positive x-direction. The send-receive distance is then:

$$x_{rn} - x_{sn} = x_{r0} - x_{s0} + 2n\Delta x. \tag{5.1}$$

In a pulse-echo setup the distance between transmitter and receiver changes and their respective distance to the feature is identical. Note that this is not the case for a pitch-catch setup where the distance between transmitter and receiver is kept constant, as illustrated in Figure 5.8b. In that case, it is the position of the feature which changes with respect to transmitter and receiver. The following considerations are therefore not applicable for that case.

It is assumed that the amplitude received by a pulse-echo probe at a position n depends on the excitation signal $A(\omega)$, a constant coupling factor C_n (to be taken into account for both excitation and reception), the send-receive sensitivity G_n of the probe setup at a position n with perfect coupling as well as a function $D(\omega, k)$, which combines influences such as mode excitability and interaction with features (i.e. reflection or transmission coefficient). The received signal $R_n(\omega, k)$ can therefore be written as:

$$R_n(\omega, k) = A(\omega) \cdot D(\omega, k) \cdot C_n^2 \cdot G_n(\omega, k). \tag{5.2}$$

The transducer converts the received signal $R_n(\omega, k)$ into a voltage $U_n(\omega)$ which can then be measured by an oscilloscope. It is assumed here that this transformation can be interpreted as an inverse Fourier transform in the spatial domain and a subsequent integration over the transducer surface S:

$$U_n(\omega) \propto \int_S \int_{-\infty}^{\infty} R_n(\omega, k) \cdot e^{ikx} dk dS. \tag{5.3}$$

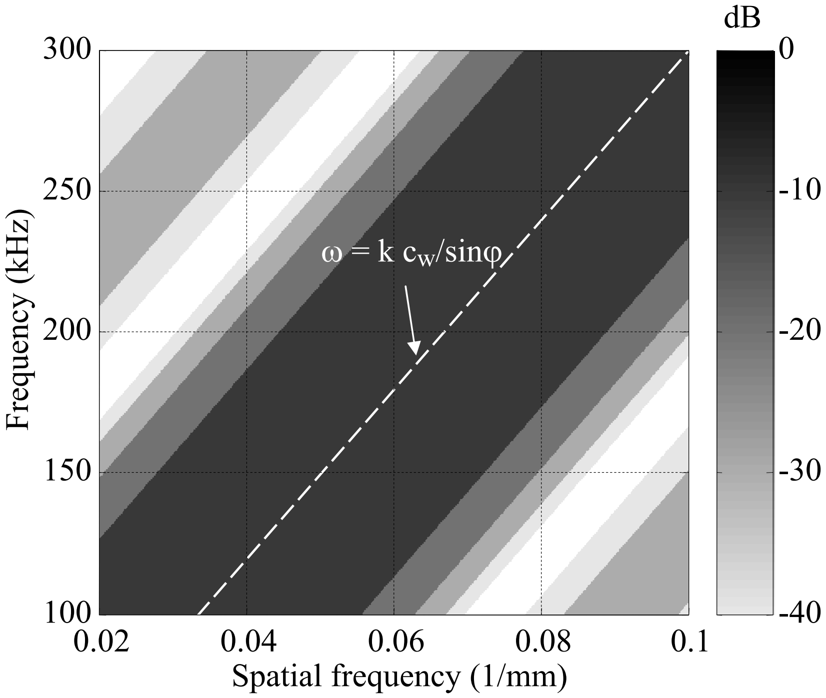

Figure 5.9: *Normalised send-receive sensitivity G_n of a 25 mm long local immersion probe angled at 30°. Filled contour levels at -10, -20, -30 and -40 dB.*

In the following, a local immersion probe will be assumed as an example to illustrate the discussion, however the findings apply to other probe types as well. Using the simple model from Appendix B, the send-receive sensitivity G_n in (5.2) for this case can be written as:

$$G_n(\omega,k) = B^2(\omega,k)\cdot e^{ik(x_{rn}-x_{sn})} \tag{5.4}$$

$$= L^2\cdot \mathrm{sinc}^2\left[\frac{L}{2}\left(\frac{\sin\varphi}{c_w}\omega - k\right)\right]\cdot e^{ik(x_{rn}-x_{sn})}. \tag{5.5}$$

Figure 5.9 shows G_n for a probe of length L = 25 mm angled at $\varphi = 30\,^\circ$ in order to excite surface waves. (Note that there is an offset for both x- and y-axis in all figures; this is to keep a consistent zoom into the area which will be of interest later.) There is a main lobe centred on the line determined by the desired constant phase velocity $\frac{c_w}{\sin\varphi} = 3000$ m/s,

$$\omega = \frac{c_w}{\sin\varphi}k, \tag{5.6}$$

and lower side lobes parallel to this. These lobes are caused by the squared sinc-function in (5.5) and are tilted according to (5.6). It is clearly shown that the probe

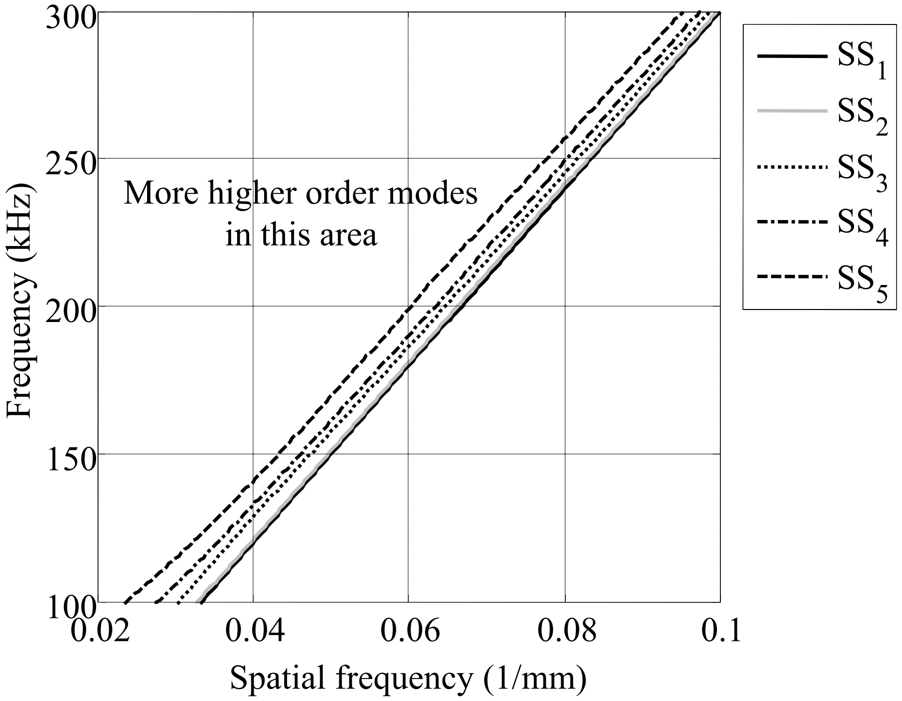

Figure 5.10: *Dispersion curves of selected symmetric surface wave modes in the rail.*

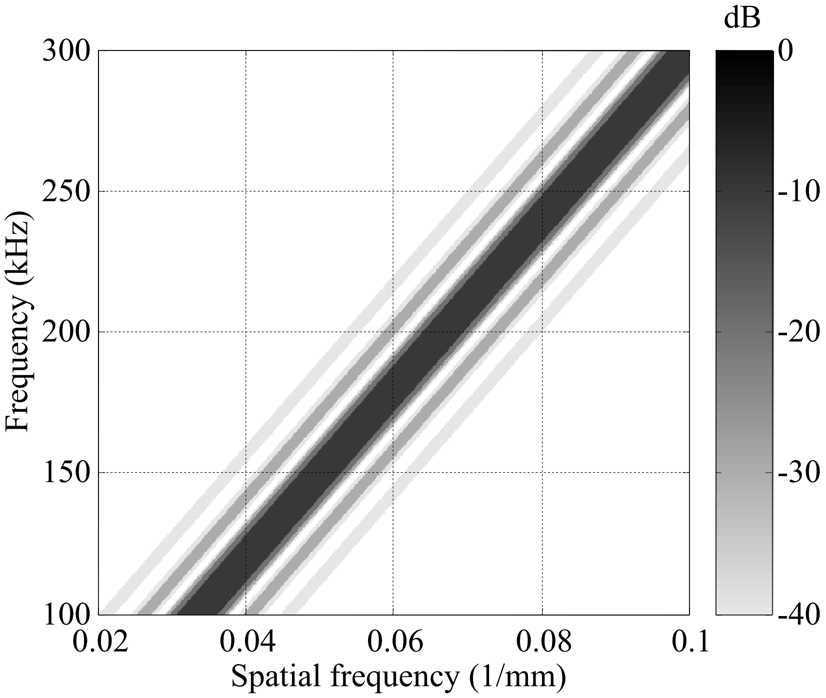

Figure 5.11: *Normalised send-receive sensitivity G_n of a 200 mm long local immersion probe angled at 30°. Filled contour levels at -10, -20, -30 and -40 dB.*

is sensitive over large areas in the 2-dimensional frequency domain and not very selective if the guided wave modes are very closely spaced as for example in this case of a rail, see Figure 5.10. It is well known that if the length L of the angled probe is increased, then the width and the spacing of the lobes is reduced and the amplitude of the side lobes is decreased, see Figure 5.11 where $L = 200$ mm.

As explained above, the process of spatial averaging consists of two steps. Firstly, a phase-shift $\Phi(\omega)$ is performed in the frequency domain on the measured voltage signals $U_n(\omega)$ from adjacent pulse-echo positions to align them to the voltage signal $U_0(\omega)$ at the reference position. Secondly, the average of the N phase shifted signals is calculated for the chosen reference position. The spatially averaged voltage signal $\bar{U}(\omega)$ is then:

$$\bar{U}(\omega) = \frac{1}{N} \sum_{n=0}^{N-1} U_n(\omega, k) \cdot e^{-i\Phi(\omega)}. \tag{5.7}$$

The phase-shift $\Phi(\omega)$ is based on the theoretical wavenumber $\tilde{k}(\omega)$ of the guided wave mode of interest and the difference in propagation distance compared to the reference position:

$$\Phi = (x_{rn} - x_{r0} - x_{sn} + x_{s0})\tilde{k}(\omega) = 2n\Delta x\tilde{k}(\omega) \tag{5.8}$$

Note that $\tilde{k}(\omega)$ is complex if attenuation is taken into account.

From (5.3) and (5.7) after swapping the order of integration and summation:

$$\bar{U}(\omega) \propto \int_S \int_{-\infty}^{\infty} \bar{R}(\omega, k) \cdot e^{ikx} dk dS, \tag{5.9}$$

where $\bar{R}(\omega, k)$ is the resulting signal obtained by spatial averaging:

$$\bar{R}(\omega, k) = \frac{1}{N} \sum_{n=0}^{N-1} R_n(\omega, k) \cdot e^{-i2n\Delta x\tilde{k}(\omega)}. \tag{5.10}$$

The coupling condition of the probe may be expressed in the form of a spatial window:

$$C(n) = \begin{cases} C_n, & \text{for } n = 0 \leq n \leq N-1, \\ 0, & \text{otherwise.} \end{cases} \tag{5.11}$$

We assume that $D(\omega, k)$ (see (5.2)) is the same for all positions n used for one spatial average. This effectively assumes that the same feature reflections are seen from each probe position. It follows that

$$\bar{R}(\omega, k) = A(\omega) \cdot D(\omega, k) \cdot \bar{G}(\omega, k), \tag{5.12}$$

in which $\bar{G}$ is the spatially averaged sensitivity:

$$\bar{G}(\omega, k) = \frac{1}{N} \sum_{n=0}^{N-1} C_n^2 \cdot G_n(\omega, k) \cdot e^{-i\tilde{k}(\omega)2n\Delta x} \tag{5.13}$$

$$= \frac{1}{N} G_0(\omega, k) \cdot H(\omega, k). \tag{5.14}$$

Hence, the sensitivity $\bar{G}$ obtained by spatial averaging is the product of the probe sensitivity G_0 at the reference position and a term $H(\omega, k)$:

$$H(\omega, k) = \sum_{n=-\infty}^{n=\infty} C^2(n) \cdot e^{i \cdot \left(k - \tilde{k}(\omega)\right) \cdot 2n\Delta x}. \tag{5.15}$$

For any given frequency ω can be interpreted $H(\omega, k)$ as a Discrete-Space Fourier Transform (DSFT) of the squared coupling function $C^2(n)$. Note that $H(\omega, k)$ is a periodic function with respect to k with a period of $\frac{\pi}{\Delta x}$, i.e.:

$$H(\omega, k) = H(\omega, k \pm n \cdot \frac{\pi}{\Delta x}), \qquad n = 1, 2, 3, \ldots \tag{5.16}$$

With respect to the spatial frequency $\frac{k}{2\pi}$ the period is equal to $\frac{1}{2\Delta x}$.

5.4.3 Characteristics and limitations

If the spatial averaging distance $N \cdot \Delta x$ is greater than the probe length L, then the selectivity of the probe is dominated by the DSFT of $C^2(n)$. This can clearly be seen in Figure 5.12 where $\bar{G}$ is shown for spatial averaging over $N = 20$ positions and $\Delta x = 10$ mm spacing for the same probe geometry as for the example in Figure 5.9. In this case, attenuation has been neglected and a constant phase velocity c_p has been assumed such that it follows for $\tilde{k}(\omega)$:

$$\tilde{k}(\omega) = \frac{\omega}{c_p}. \tag{5.17}$$

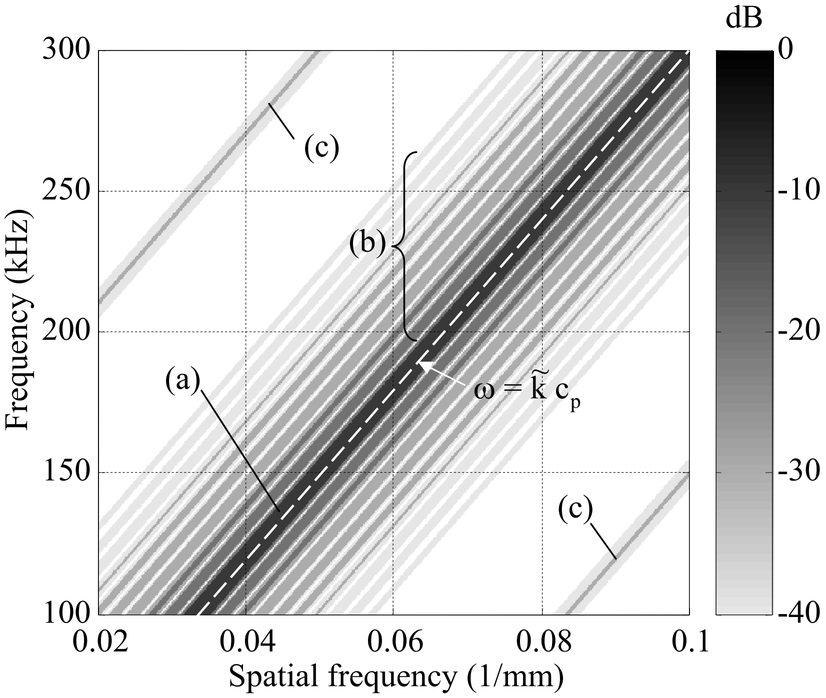

Figure 5.12: *Normalised send-receive sensitivity $\bar{G}$, spatial averaging of $N = 20$ positions, spacing $\Delta x = 10$ mm, 25 mm long local immersion probe angled at 30°. Filled contour levels at -10, -20, -30 and -40 dB. (a) Main lobe; (b) side lobes; (c) grating lobes due to periodicity of $H(\omega, k)$.*

Furthermore, perfect coupling has been assumed, i.e. the coupling function $C(n)$ is a rectangular window of length $N \cdot \Delta x = 200$ mm, and therefore the sensitivity $\bar{G}$ exhibits lobes that approximate a sinc-function. The main lobe is centred on the line determined by the dispersion relation for $\tilde{k}(\omega)$, i.e., in this case, (5.17). There are grating lobes (labelled (c) in Figure 5.12) parallel to this line caused by the periodicity of $H(\omega, k)$ with respect to k (see (5.16)). The magnitude of these grating lobes is reduced by the sensitivity function G_0 of the single probe, see Figure 5.9 for comparison. This becomes even clearer for a case with increased probe spacing Δx, i.e. the period of $H(\omega, k)$ with respect to k is shortened. The resulting aliasing effect can be seen in Figure 5.13, which is a normalised plot of $\bar{G}$ for the same probe geometry and averaging length as in Figure 5.12, but for $N = 5$ positions and $\Delta x = 40$ mm spacing. The distance between the grating lobes is reduced such that some of them are located inside the main lobe of the single probe sensitivity G_0 (see Figure 5.9) where they are not significantly lowered in

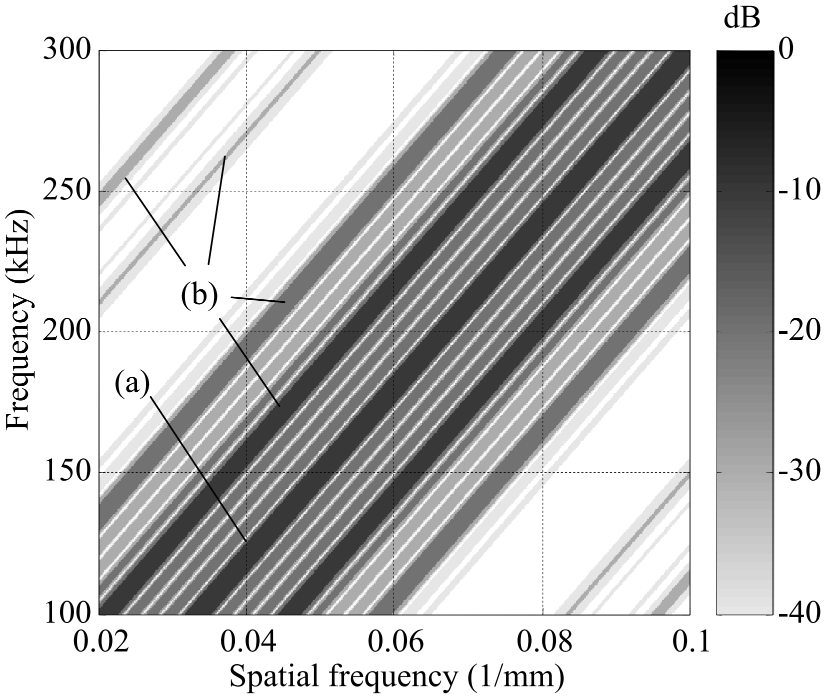

Figure 5.13: *Normalised send-receive sensitivity* $\bar{G}$*, spatial averaging of* $N = 5$ *positions, spacing* $\Delta x = 40$ *mm, 25 mm long local immersion probe angled at 30°. Filled contour levels at -10, -20, -30 and -40 dB. (a) Main lobe; (b) grating lobes due to periodicity of* $H(\omega, k)$*.*

amplitude. This means that the mode selectivity of the setup significantly decreases if the probe spacing is too large. However, the single probe sensitivity G_0 which can attenuate grating lobes allows us to spatially undersample the signal to some extent without significantly reducing the modal selectivity. In this example, the probe was simplified as a plane wave multiplied by a rectangular window. The optimal compromise between measurement efficiency and aliasing in this case is to choose the probe spacing to be half the probe length, such that grating lobes due to aliasing are positioned at minima of the single probe sensitivity G_0. Figure 5.14 confirms that there are no relevant grating lobes in $\bar{G}$ for $N = 16$ and $\Delta x = L/2 = 12.5$ mm.

The three spatial averaging examples shown in Figs. 5.12, 5.13 and 5.14 have the same spatial averaging length $N \cdot \Delta x = 200$ mm, hence the width of their main lobes is identical. However, due to the factor 2 in the exponent of $H(\omega, k)$ (see (5.15)), the width of the lobes in these three examples is only half that of the probe

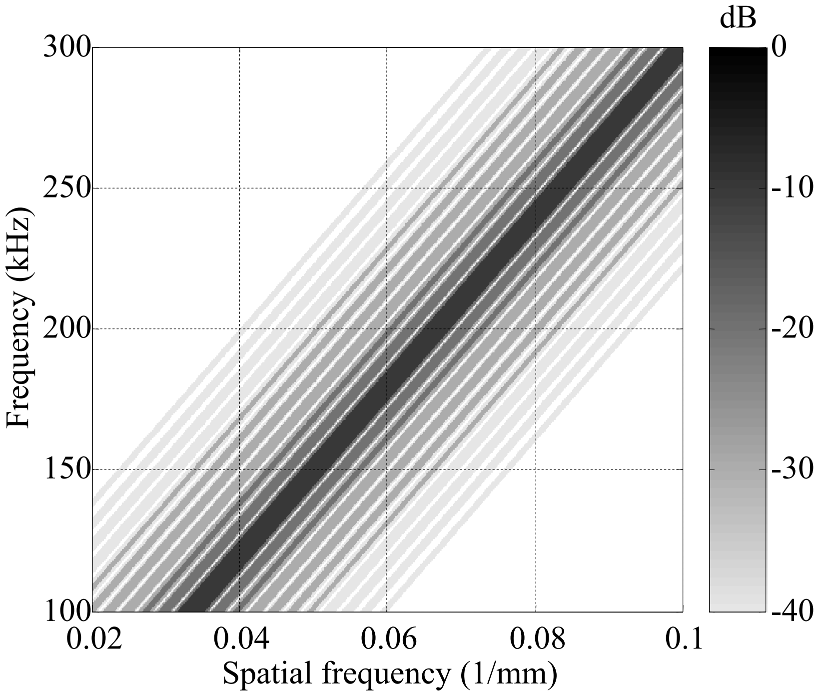

Figure 5.14: *Normalised send-receive sensitivity* $\bar{G}$*, spatial averaging of* $N = 16$ *positions, spacing* $\Delta x = 12.5$ *mm, 25 mm long local immersion probe angled at 30°. Filled contour levels at -10, -20, -30 and -40 dB.*

with $L = 200$ mm in Figure 5.11. The selectivity of spatial averaging over a long distance therefore appears to be higher than that of a single probe of equivalent length. However, the side lobes have lower amplitudes in the case of the long single probe since they are caused by a squared sinc-function, see (5.5). This difference will be discussed in more detail when single probe spatial averaging is compared to a phased array.

Theoretically, the mode selectivity could be improved by increasing the spatial averaging length $N \cdot \Delta x$ further and further. However, the accuracy of the phase shift which is applied to the acquired signals depends on the uncertainties in the wavenumber $\tilde{k}(\omega)$ of the mode of interest and the probe spacing Δx. The wavenumber $\tilde{k}(\omega)$ is essentially an estimate, and uncertainties can be associated with both the real part, i.e. the phase velocity c_p, as well as the imaginary part, i.e. attenuation. The latter will not be considered here.

The procedure averages the signal assuming a nominal phase velocity c_p. In practice,

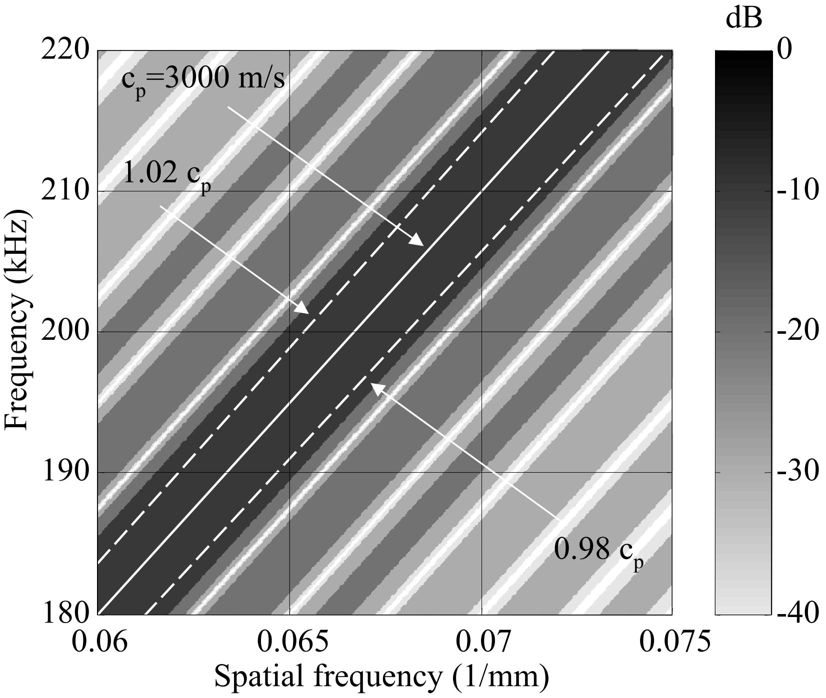

Figure 5.15: *Estimated phase velocity c_p = 3000 m/s (solid line) and possible true phase velocities (dashed lines) for an uncertainty of ±2% plotted on normalised sensitivity $\bar{G}$ for N = 10, Δx =20 mm. Filled contour levels at -10, -20, -30 and -40 dB.*

the true phase velocity may be different and it is important that the signals of interest are still seen even though an incorrect phase velocity has been assumed. Figure 5.15 shows an enlarged plot of Figure 5.12 in which the nominal phase velocity was assumed to be $c_p = 3000$ mm (solid line). The two dashed lines represent true phase velocities 2% lower and 2% higher than the estimate c_p (note that the two dashed lines are not parallel). Both lines are situated inside the main sensitivity lobe which means that the over- or underestimation of the phase velocity would not severely affect the signals in this example. Increasing the averaging length would narrow the main lobe and therefore the dashed lines could be located partly outside the main lobe. This means that the received signal of the mode of interest would be distorted in the frequency domain or it might be fully suppressed. The uncertainty of the phase velocity estimate therefore seems to be a major limitation of the mode selectivity achievable by spatial averaging.

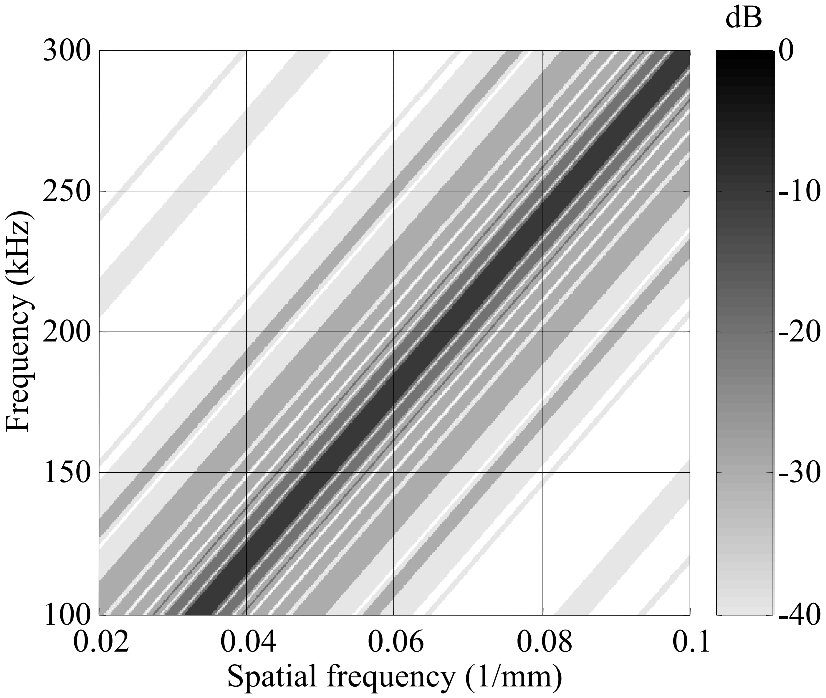

Figure 5.16: *Normalised send-receive sensitivity $\bar{G}$ for same configuration as Figure 5.12, but with a random error of -5 mm $\leq x_{err,n} \leq$ 5 mm. Filled contour levels at -10, -20, -30 and -40 dB.*

Uncertainties $x_{\mathrm{err},n}$ of the probe spacing such that

$$x_{rn} - x_{sn} = x_{r0} - x_{s0} + 2n\Delta x + x_{\mathrm{err},n} \tag{5.18}$$

instead of (5.1) result in phase errors of the DSFT term $H(\omega, k)$ in (5.15). If these errors are of random nature and N is fairly high, then the width of the main sensitivity lobe is hardly affected. Figure 5.16 shows the same configuration as Figure 5.12, but with an unrealistically high random error of -5 mm $\leq x_{\mathrm{err},n} \leq 5$ mm, normally distributed with a variance of $\sigma^2 = 0.2$. The side lobe amplitudes as well as their spacing are altered and have become more irregular, but the main lobe has not changed significantly compared to Figure 5.12. For a somewhat more realistic uncertainty of -0.5 mm $\leq x_{\mathrm{err},n} \leq 0.5$ mm, even the effect on the side lobes was found to be negligible. Therefore spatial averaging appears to be relatively robust with respect to random probe positioning errors.

So far, perfect coupling of the probe has been assumed for all positions n, i.e. $C_n = 1$. Inconsistencies of the coupling are equivalent to an apodisation of the received signals

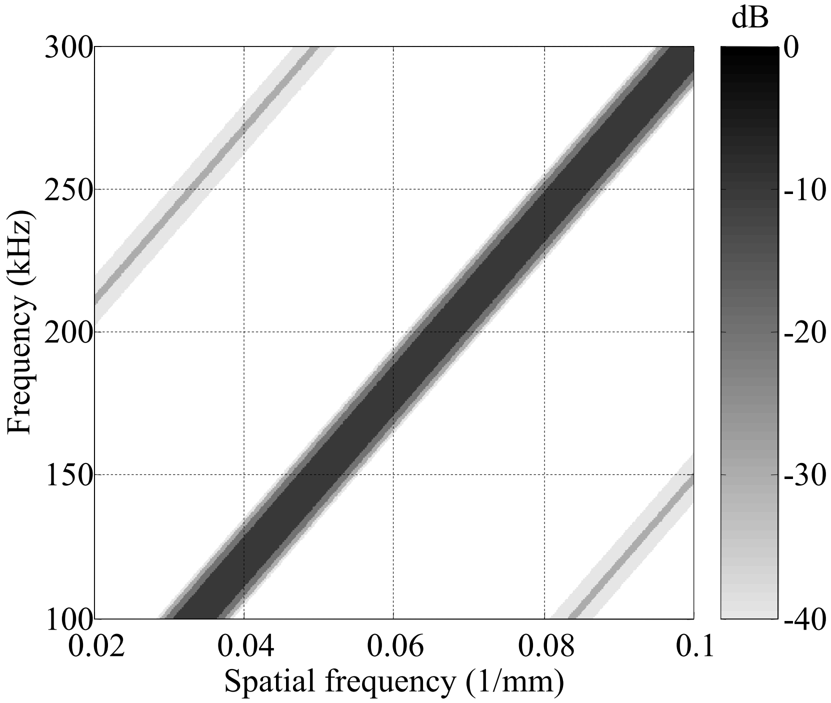

Figure 5.17: *Normalised send-receive sensitivity $\bar{G}$, spatial averaging of $N = 20$ positions, spacing $\Delta x = 10$ mm, Hamming window apodisation of $C^2(n)$, 25 mm long local immersion probe angled at 30°. Filled contour levels at -10, -20, -30 and -40 dB.*

at different positions with unknown weighting factors. Thus the coupling function $C(n)$ is not a rectangular window but can be of arbitrary shape. Since $H(\omega, k)$ can be interpreted as a DSFT of $C^2(n)$, the coupling inconsistencies will affect the amplitude, spacing and width of both main and side lobes of the spatial averaging sensitivity $\bar{G}(\omega, k)$. The likely result is a reduction in mode selectivity which can be compensated to some extent by increasing the spatial averaging length.

Deliberate apodisation of signals from different positions can be used as a means to customise the spatial averaging sensitivity $\bar{G}(\omega, k)$. We can introduce a weighting

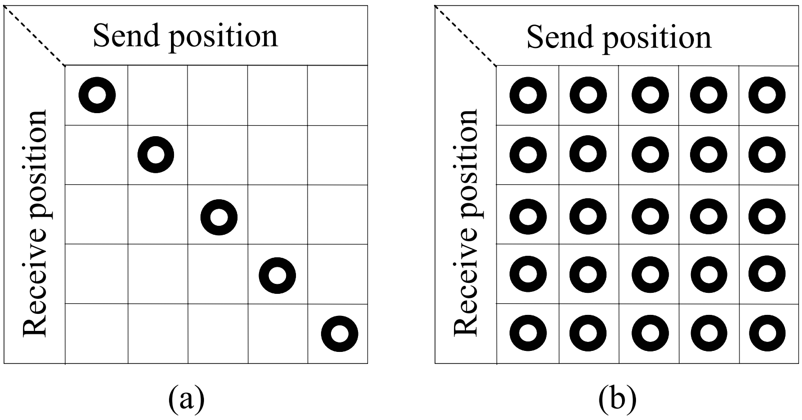

Figure 5.18: *Send-receive matrix of (a) single probe spatial averaging and (b) phased array (taking into account all possible send-receive-paths).*

function $w(n)$ into (5.7), (5.10) and (5.11) such that:

$$\bar{U}(\omega,k) = \frac{1}{N}\sum_{n=0}^{N-1} w(n)\cdot U_n(\omega,k)\cdot e^{-i2n\Delta x\tilde{k}(\omega)}, \tag{5.19}$$

$$\bar{R}(\omega,k) = \frac{1}{N}\sum_{n=0}^{N-1} w(n)\cdot R_n(\omega,k)\cdot e^{-i2n\Delta x\tilde{k}(\omega)}, \tag{5.20}$$

$$C(n) = \begin{cases} \sqrt{w(n)}\cdot C_n & \text{for } n = 0 \le n \le N-1, \\ 0 & \text{otherwise.} \end{cases} \tag{5.21}$$

Figure 5.17 shows $\bar{G}$ for the same parameters as Figure 5.12, but with an additional weighting function $w(n)$ chosen to be a Hamming window. (Note: The Fourier transform of this features a wider main lobe than that of a rectangular window, but all side lobes are below -40 dB, see Appendix C.) For the spatially averaged sensitivity $\bar{G}$ this results in significantly reduced side lobes (even compared to the long monolithic probe in Figure 5.11), but an increased width of the main lobe compared to Figure 5.12. Note that the position and the amplitude of the grating lobes due to the periodicity of $H(\omega,k)$ remain unchanged.

5.4.4 Comparison with phased array

In order to compare the spatial averaging technique applied to a moving pulse-echo probe with a linear phased array the measurement positions are interpreted as elements of an array. For a single moving probe the send and receive positions are identical (assuming that the probe velocity is negligible compared to the wave velocity). This corresponds to the main diagonal in a matrix of all send and receive combinations, as illustrated in Figure 5.18a. If there were identical fixed transducers at all positions, i.e. a full linear phased array (PA), it would be possible to obtain data for all send-receive combinations such that the matrix would be fully populated, see Figure 5.18b. For the sake of this discussion, it is assumed that each element of the array is coupled with the same coupling characteristics as a single probe. If random noise is neglected, the matrix is symmetric with respect to the main diagonal due to reciprocity. Analogously to the single moving probe the same procedure of phase-shifting and summation is applied to the phased array. The resulting signal $\bar{R}_{PA}(\omega, k)$ is then:

$$\begin{aligned}\bar{R}_{PA}(\omega, k) = \frac{1}{N^2} \sum_{m=0}^{N-1} \sum_{n=0}^{N-1} & R_{mn}(\omega, k) \\ & \cdot e^{-i(x_{rn} - x_{r0} - x_{sm} + x_{s0})\tilde{k}(\omega)}, \end{aligned} \tag{5.22}$$

with R_{mn} denoting the signal sent by element m and received by element n. This procedure is essentially the same as the synthetic phase tuning method utilised by Wooh and Shi [117]. However, in their algorithm the diagonal of the send-receive matrix has not been taken into account, probably due to limitations of the multiplexer in their experimental setup. Another difference is that they have applied delays in the time domain rather than the frequency domain which means that dispersion and attenuation cannot be allowed for.

From (5.22) and analogous to (5.12)-(5.15) the send-receive sensitivity $\bar{G}_{PA}$ of the linear phased array can be derived as:

$$\begin{aligned}\bar{G}_{PA}(\omega, k) &= G_0(\omega, k) \cdot \frac{1}{N^2} \cdot \sum_{m=-\infty}^{m=\infty} C(m) \cdot e^{i\left(k - \tilde{k}(\omega)\right) m \Delta x} \\ &\quad \cdot \sum_{n=-\infty}^{n=\infty} C(n) \cdot e^{i\left(k - \tilde{k}(\omega)\right) n \Delta x} && (5.23) \\ &= \frac{1}{N^2} \cdot G_0(\omega, k) \cdot H_{PA}(\omega, k), && (5.24)\end{aligned}$$

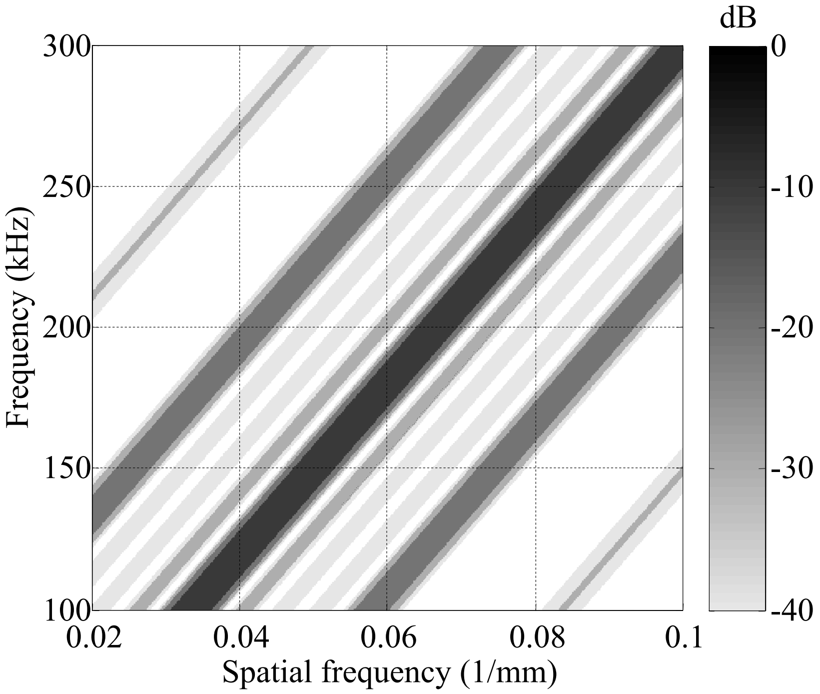

Figure 5.19: *Normalised send-receive sensitivity $\bar{G}_{PA}$, phased array consisting of $N = 5$ local immersion probes (25 mm long, angled at 30°), spacing $\Delta x = 40$ mm. Filled contour levels at -10, -20, -30 and -40 dB.*

where

$$H_{PA}(\omega, k) = \left(\sum_{n=-\infty}^{n=\infty} C(n) \cdot e^{i\left(k-\tilde{k}(\omega)\right)n\Delta x} \right)^2 . \tag{5.25}$$

Analogous to single probe spatial averaging, the sensitivity $\bar{G}_{PA}$ is essentially a product of the sensitivity G_0 of a single probe or array element and a term $H_{PA}(\omega, k)$ that contains a DSFT of the contact function. In contrast to $H(\omega, k)$ for single probe spatial averaging however (see (5.15)), the DSFT is performed on $C(n)$ rather than $C^2(n)$ using a spatial sampling interval of Δx (rather than $2\Delta x$) and then the overall result is squared. The period of $H_{PA}(\omega, k)$ with respect to k is $2\pi/\Delta x$, i.e. twice as large as for $H(\omega, k)$ in (5.15). For a given number of positions N and a probe spacing Δx the phased array sensitivity $\bar{G}_{PA}(\omega, k)$ therefore exhibits lower side lobes and twice the spacing between periodic main lobes than the single probe spatial averaging sensitivity $\bar{G}(\omega, k)$. However, this is at the expense of doubling the width of the main lobe which can be very disadvantageous for the separation of modes with very similar propagation properties. Figure 5.19 shows $\bar{G}_{PA}(\omega, k)$

for a setup with $N = 5$ local immersion probes with a length of $L = 25$ mm each and a spacing of $\Delta x = 40$ mm. These are the same parameters as for the spatial averaging case presented in Figure 5.13. It can be seen that side lobes in Figure 5.19 are reduced compared to Figure 5.13, the distance between periodic main lobes is doubled and the main lobe is twice as wide.

Note that if the probe spacing of the linear phased array is chosen to be the same as the element length, i.e. $\Delta x = L$, then the additional periodic main lobes coincide with minima of G_0 and are therefore suppressed. This is essentially the same as a monolithic probe with the length of the array aperture $N \cdot \Delta x$ (see Figure 5.11).

The array interpretation of the moving probe also reveals an interesting analogy to synthetic aperture imaging algorithms (see for example References [124–128]). When comparing (5.7) and (5.10) to definitions given there, it turns out that spatial averaging can essentially be regarded as a one-dimensional case of a SAFT algorithm. The spatial averaging positions, i.e. the array, and all imaging points are located on a single line. In conventional SAFT imaging, the array is located on the edge of a two-dimensional imaging space. The case of the linear array corresponds in turn to a one dimensional variant of phased array (PA) imaging (also referred to as the Total Focussing Method (TFM)) which uses all possible send and receive paths. The characteristics found for mode selectivity in this thesis are analogous to characteristics of the point-spread function of these imaging algorithms.

5.4.5 Experiment on rail

An experiment to illustrate the effect of spatial averaging was carried out on a relatively short piece of rail containing several artificial defects. The specimen was a BS113A type rail with a length of 730 mm. Three vertical defects with a maximum depth of 1.5 mm, 3 mm and 5 mm had been cut into the railhead corner using a circular slitting saw blade (4” x 1/64”) so that they produced reasonably realistic defects, see Figure 5.20a.

The probe described in Section 5.2 was operated in standard pulse-echo mode. The

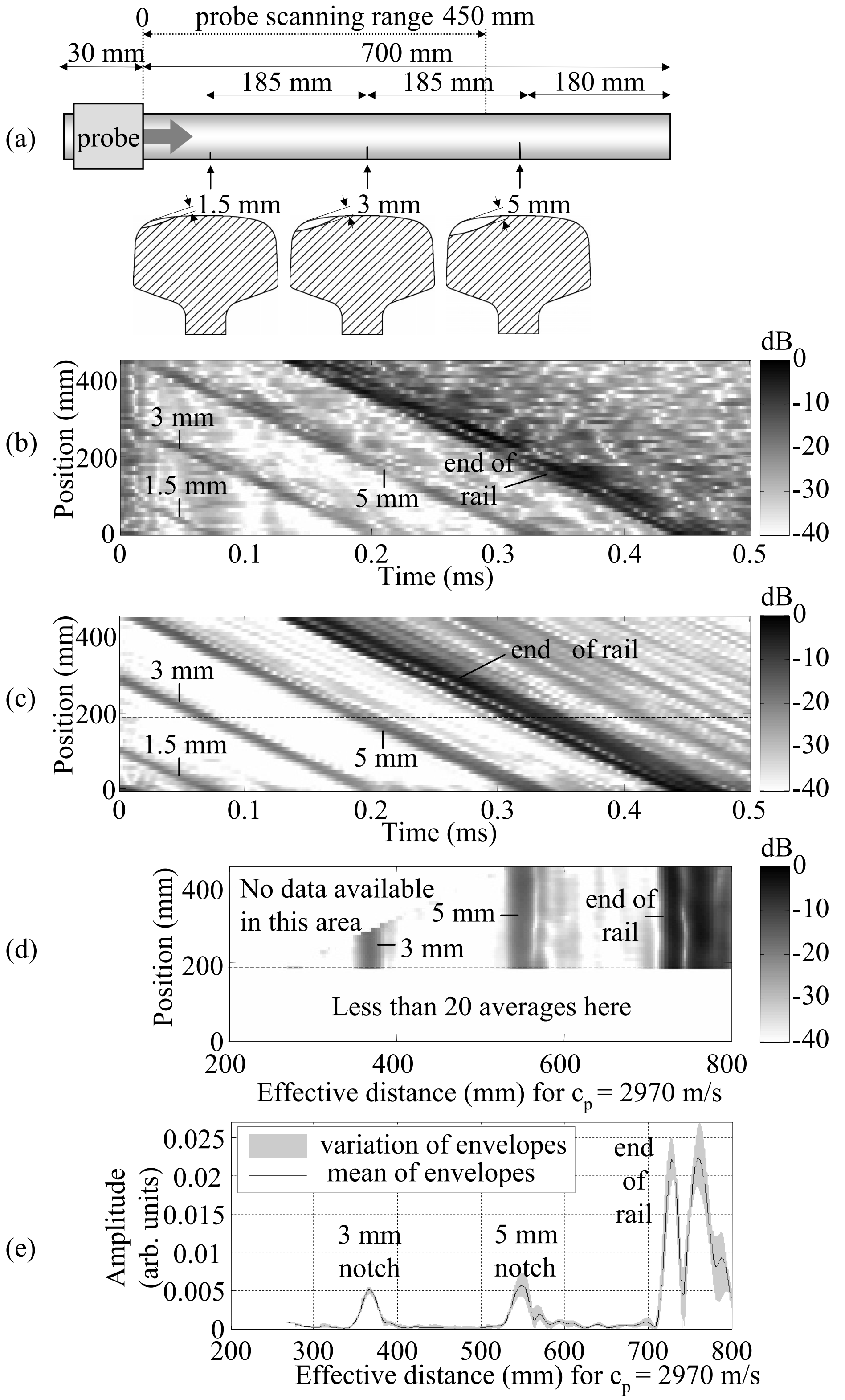

Figure 5.20: *(a) Sketch of rail specimen containing artificial defects; (b) B-scan plot of envelope of raw signals; (c) B-scan plot of envelope of spatially averaged signals ($N = 20$, $\Delta x = 10$ mm); (d) tilted B-scan based on Figure 5.20c, time replaced with effective distance, (e) mean and variation of envelopes, extracted from Figure 5.20d .*

array elements were effectively all connected together such that the array acted like a wide monolithic probe to allow the excitation and reception of waves nearly across the full width of the railhead. No focussing or apodisation was applied, based on the findings discussed in Section 5.3. The excitation signal was a 5 cycle Hanning windowed toneburst with a centre frequency at 200 kHz.

The probe was placed 700 mm away from the end of the railhead (zero position) and then scanned 450 mm along the centreline of the rail towards the end in increments of $\Delta x = 10$ mm (see Figure 5.20a). Following the data acquisition, unwanted modes were suppressed by applying the single probe spatial averaging method. Since the mode of interest in this case, SS_1, is virtually non-dispersive, the spatial averaging process can alternatively be performed in the time domain resulting in a very fast and simple summation algorithm.

The results are presented in Figure 5.20b as a B-scan, thus combining the A-scans of all probe positions in one image and plotting the normalised signal envelopes on a logarithmic grey scale. Features in the rail specimen show up as angled features in the time-position plane with their slope corresponding to the group velocity of the wave. The reflections from the 1.5 mm, 3 mm and 5 mm notches as well as from the end of the rail can be seen. However, there is a very high level of coherent noise present and the feature amplitudes vary for different probe positions. Figure 5.20c is a B-scan plot of the signal envelopes after spatial averaging using N=20 positions, a probe spacing of $\Delta x = 10$ mm and a phase velocity of $c_p = 2970$ m/s. The level of coherent noise and the amplitude variations of the reflected signals due to the interference of multiple modes are significantly reduced compared to Figure 5.20b. Note that the full number $N = 20$ of averages has been reached only above the dashed line in Figure 5.20c; below that there were fewer previous measurement points available due to the short specimen. A very compact alternative means of displaying the data can be achieved by condensing the data of Figure 5.20c into an A-scan type plot. As a first step, the time axis is replaced with an effective distance on the specimen based on the phase velocity c_p of SS_1. The probe positions have been taken into account as well such that the B-scan is now effectively tilted and

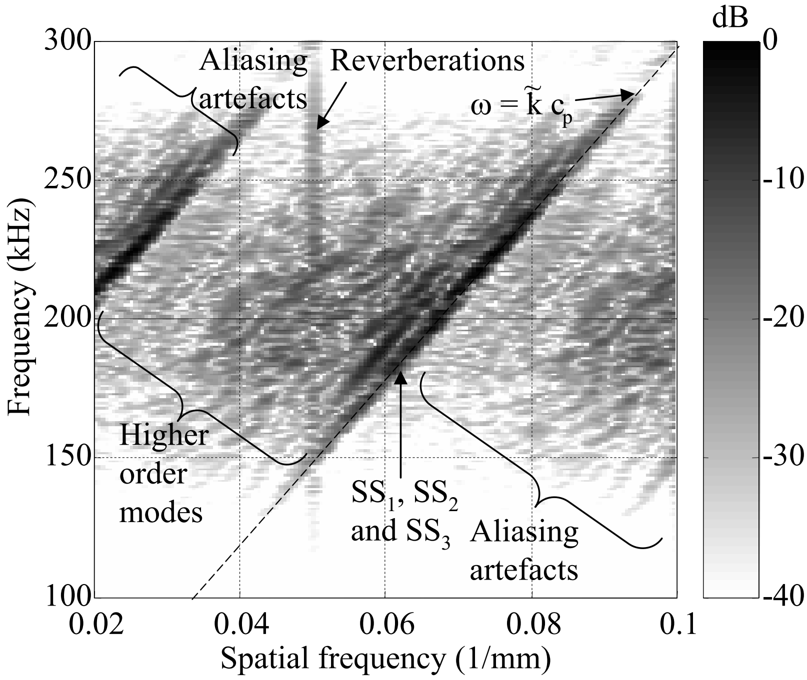

Figure 5.21: *2D-FFT of RF signals measured on rail specimen.*

the reflections appear vertically aligned, see Figure 5.20d. The white triangle in the top left corner indicates an area for which no data is available because of the scanning of the probe. Furthermore, note that the area with fewer than $N = 20$ averages due to the short specimen (see above) was not considered which results in an (only apparent) loss of the 1.5 mm notch in Figure 5.20d. In the second step, for each column of the envelope matrix plotted here (i.e. a given effective distance on the specimen) the mean across all rows (i.e. all probe positions) is calculated. Similarly the maximum and minimum values of each column are determined. The values for all rows are then combined, resulting in three vectors, namely the mean of the envelopes, the minima along the columns and the maxima along the columns. The area between the latter two is the variation of the envelopes. The mean and the variation of the envelopes are plotted in an A-scan equivalent which indicates clearly where defects are located in the specimen, see Figure 5.20e. (The 1.5-mm-notch is again not visible because of omission of probe positions with fewer than N=20 averages as explained earlier.)

The effect of the spatial averaging process in the wavenumber-frequency domain can

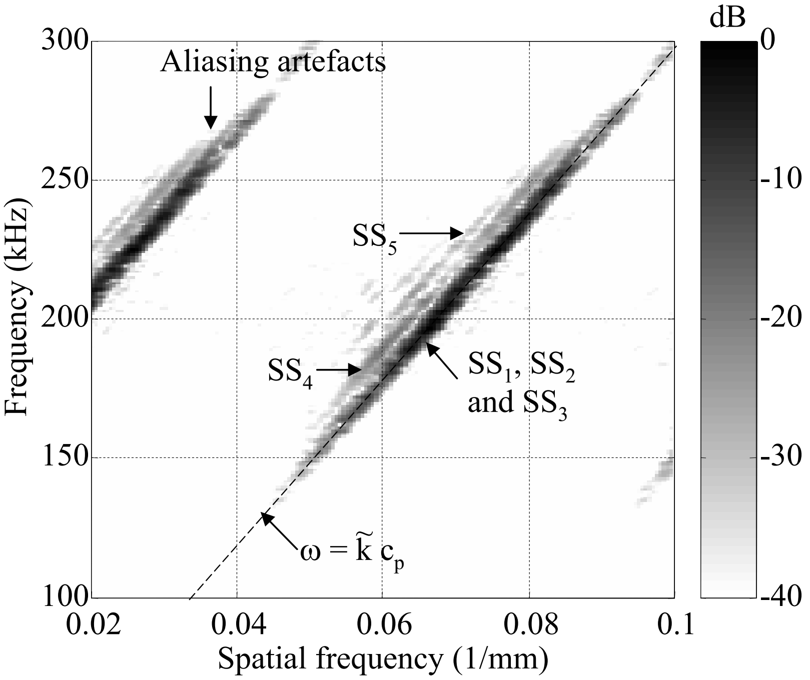

Figure 5.22: *2D-FFT of spatially averaged signals with $N = 20$ and $\Delta x = 10$ mm.*

be visualised by performing a two-dimensional Fourier transform (2D-FFT) [87] on the spatially averaged RF data. Figure 5.21 shows a 2D-FFT of all available raw RF signals without spatial averaging. Dark patches in the 2-dimensional frequency domain correspond to different modes, however in this case the number of modes present was very high and it was difficult to identify individual modes. The limited spatial resolution of the 2D-FFT was caused by the relatively short sampling length due to the short specimen. The comparison with Figure 5.10 shows that the modes SS_1, SS_2 and SS_3 constituted the dominant patch in the 2-dimensional frequency domain. In addition to this, there was a vast number of higher order modes contained in the signal, see the indicated area in Figure 5.21. Note that the effective spatial sampling interval of the 2D-FFT was $2\Delta x$ rather than Δx because of the pulse echo setup. The relatively large probe spacing caused the signals to be spatially undersampled which results in the marked aliasing regions. The vertical stripe in the area of higher order modes is due to reverberations of the incident wave inside the probe. This stripe is actually located at a spatial frequency of 0 mm^{-1}, however it also appears at 0.05 mm^{-1} because of aliasing. Figure 5.22 is a 2D-FFT on all available signals after spatial averaging. The dashed line in both figures represents the dispersion relation used for the spatial averaging process (see (5.17)) assuming a constant phase velocity of $c_p = 2970$ mm. Modes inside the main lobe centred on this dashed line and in the marked aliasing regions remained unaffected, but the unwanted modes outside these areas were significantly suppressed, see Figure 5.22. A probe of this size is not very sensitive in these aliasing regions (see Figs. 5.9 and 5.12), which means that the high magnitude there is mainly an artefact of the 2D-FFT rather than an actual signal. Note that the vertical stripe caused by reverberations of the incident wave inside the probe (see Figure 5.21) has completely disappeared in Figure 5.22. The spatial averaging process efficiently removes such reverberations and therefore reduces the dead zone of the probe. From the comparison of Figures 5.21 and 5.22 it can be concluded that the spatial averaging method very effectively suppressed higher order modes, but there are still contributions of some unwanted modes, most notably SS_2 and SS_3, as well as smaller contributions of SS_4 and SS_5.

5.4.6 Conclusions

The single probe spatial averaging method was found to be a very efficient technique to increase the mode selectivity of a probe scanned along a wave guide in pulse-echo mode. The method can potentially be applied to any type of wave guide or probe type. If the dispersion curves of the wave guide are known, the method makes it possible to utilise a simple robust but not very mode selective probe for the data acquisition and then customise the mode selectivity using the spatial averaging technique.

The sensitivity of the probe itself acts like an additional weighting in the wave number frequency domain. For a probe which is short in the direction along the waveguide with a fairly broad sensitivity the effects of small manufacturing or alignment errors are therefore negligible. Since the effective spatial sampling interval of the DSFT term is half the probe spacing, the main lobe of the sensitivity function for spatial averaging is half as wide as that of a linear phased array or monolithic probe of the same length. This advantage of spatial averaging comes at the expense of a halved effective spatial sampling frequency compared to a linear phased array. If the probe spacing is too large, the suppression of unwanted modes can therefore be insufficient due to aliasing effects. However, since the finite size of the probe itself leads to a reduced sensitivity in certain areas of the 2-dimensional frequency domain, spatial undersampling can be tolerated to some extent. This allows a compromise between mode selectivity and higher probe speed due to larger intervals between the measurement points.

The experimental test on rail has shown that the method suppressed unwanted modes and reverberations inside the probe very efficiently. In order to isolate the mode SS_1 from the remaining unwanted modes, especially SS_2 and SS_3, it would be necessary to increase the spatial averaging length. This would require very accurate knowledge of phase velocity of SS_1 with an uncertainty below 1% in order to avoid errors in the applied phase delays. This did not appear feasible because of variations of rail geometry and material properties. For this reason, it was decided not to extend the spatial averaging length further and that the remaining signal content of some unwanted modes had to be accepted. However, the achieved suppression of unwanted modes was substantial and the method has been found to be highly beneficial, robust and easy to implement.

5.5 Summary

In this chapter, strategies for the efficient excitation and reception of the desired surface mode SS_1 have been investigated. These involved matching the excitation to the mode shape of the desired wave mode around the cross-section perimeter and to the wave propagation characteristics along the waveguide.

The probe design incorporated an 8-channel transducer array orientated across the railhead which provided the flexibility to test different focussing and apodisation methods at the signal postprocessing stage. Unfortunately, due to issues with the supplier of the transducer array and resulting delays, a reduced probe prototype had to be built. However, this sliding (rather than rolling) probe performed satisfactorily and was sufficient for the purpose of this project.

The first approach was to optimise the excitation of the mode SS_1 across the railhead surface by array focussing and apodisation. Due to the complex geometry of the railhead, it was decided to determine the necessary phase delays and apodisation factors for the array elements via a reverse engineering approach using FEM. A pure mode SS_1 signal was received by a probe model and then time reversed to excite the mode in the rail. The result was not satisfactory, since other very similar modes were excited as well. It was found that the unfocussed array of which all channels are excited in parallel produced a more acceptable surface wave signal. That way, more higher order modes were excited but the signal content of modes which are very similar to SS_1 was reduced. The advantages of this are a smaller (if more rapid) variation of the signal envelope with propagation distance and the option of suppressing higher order modes with another method.

As a second technique, a single probe spatial averaging method has been developed to customise the mode selectivity of guided wave probes that are scanned along a wave guide. If the dispersion relation of the mode of interest is known, then the sensitivity to this mode can be enhanced and other modes are suppressed. In principle, it is therefore possible to utilise a very simple universal probe for different waveguides and to adjust its mode selectivity by spatial averaging.

It was shown that the main effect of the spatial averaging method can be explained as a DSFT of the probe coupling represented as a spatial window. Another way of looking at spatial averaging is to interpret it as a one-dimensional SAFT algorithm. Since the mode selectivity is determined by the spatial averaging length, a higher selectivity is achieved by simply averaging over a longer distance without the need for a long transducer. Single probe spatial averaging is limited by uncertainties of the assumed phase velocity of the mode of interest, but appears to be robust with respect to small random probe position uncertainties.

The benefit of the method was demonstrated experimentally using the sliding probe mentioned above on a rail containing artificial defects. Spatial averaging over a distance of 200 mm with 10 mm probe spacing significantly reduced the level of coherent noise caused by unwanted interfering wave modes. Complete suppression of unwanted modes was not achieved because of very similar propagation properties and uncertainties in the assumed phase velocity. A very compact visualisation of the results was developed by combining the envelopes of the spatially averaged signals into an A-scan type plot. This clearly indicates positions of features in the wave guide and is therefore easy to interpret. The sliding probe with the array acting like a monolithic probe combined with single probe spatial averaging has proven very efficient and robust and was therefore adopted as the experimental method for further experiments.

Chapter 6

Detection of defects in the rail head

6.1 Background

In Chapter 5 it was shown that a local immersion probe containing a wide transducer (realised as an array with all channels connected in parallel), in conjunction with a spatial averaging method to boost mode selectivity at the signal postprocessing stage, would be a suitable setup for rail inspection purposes. The probe was sliding rather than rolling, however it was expected that the experience gathered with this prototype could be transferred to a wheel probe at a later stage. In order to assess the performance of the method for reliable defect detection, experiments were performed on a number of specimens containing artificial defects and real RCF cracks. The results and their implications are discussed in this chapter.

After a brief explanation of the experimental procedure, the results of measurements on specimens containing artificial defects are presented. This is followed by a detailed section on specimens containing different kinds of real RCF cracks.

6.2 Experimental procedure

The probe, the measurement procedure and the signal processing were the same as in Section 5.4.5. The probe was scanned along the specimens with a spacing of $\Delta x = 10$ mm, its position being measured with a ruler. The array was run as a monolithic transducer, i.e. all elements were effectively connected in parallel. (Note: For the experiments with artificial defects this was done in software by summing all acquired send and receive signals of the array; for all other experiments the elements were physically connected in parallel.) The excitation signal was a 5 cycle Hanning windowed toneburst with a centre frequency of 200 kHz, which was generated by a "Macro Design WaveMaker-Duet". This was operated in pulse-echo echo mode and amplified the received signal before sending it to an oscilloscope. At each measurement point the probe was carefully aligned, the data acquisition was triggered manually and the summed average of 50 signals was captured by the oscilloscope and then transferred to a PC. This procedure took nearly 1 min per measurement position, which is of course far from being a fast moving setup. The high number of averages and a very low pulse repetition frequency (in the order of 10 Hz) was chosen to suppress noise caused by signal reverberations in the relatively short specimens (many of them less than 1 m long). Note that the problem of signal reverberations would be significantly reduced in longer sections of rail, such that it should be possible to do single shot data acquisition in practice on the rail track.

All settings of the test equipment were kept the same throughout the experiments for the comparison of the results in this section. However, small unintended variations may have occurred due to limited accuracy of the amplifier settings as well as coupling changes. After a full set of measurements on each specimen, the data was postprocessed with MATLAB. All signals were bandpass filtered in the range between 50 and 500 kHz using a non-causal butterworth filter without phase distortion. Afterwards, the spatial averaging algorithm was applied according to Section 5.4.2, with $c_p = 2970$ m/s. The data was then condensed into A-scan equivalents as explained in Section 5.4.5.

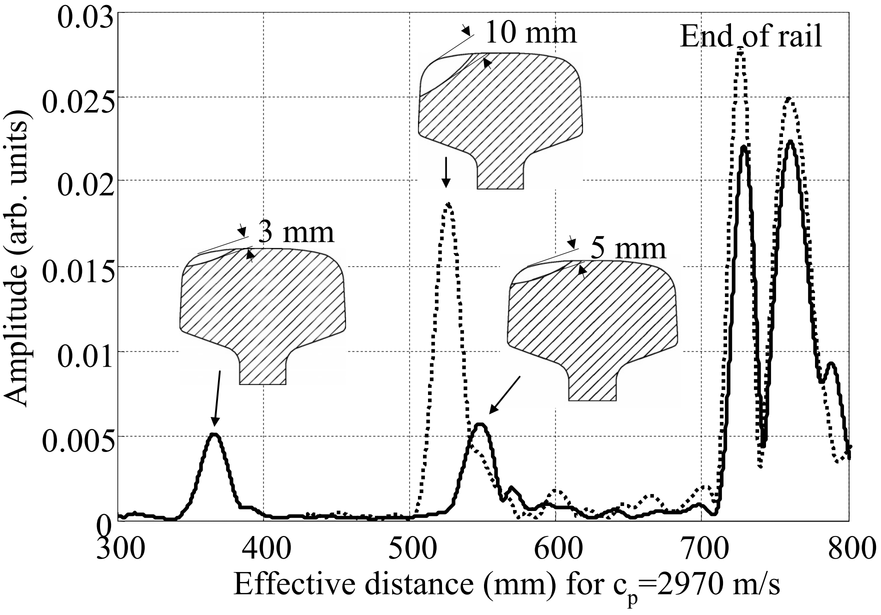

Figure 6.1: *Surface wave scans of rail containing artificial defects. Solid line: specimen 1 containing a 3 mm and 5 mm deep transverse notch. Dotted line: specimen 2 containing a 10 mm deep transverse notch.*

6.3 Artificial gauge corner defects

The system was first tested on a number of specimens containing artificial defects. The test specimens were three BS113A type rail sections: specimens 1 and 2 were about 730 mm long, specimen 3 was about 1350 mm long. Vertical and angled notches were machined into the railhead corner using circular slitting saw blades (4" x 1/64" for 1.5 mm to 5 mm deep notches, 5" x 1/32" for a 10 mm deep notch, 4" x 1/32" for an angled 3 mm deep notch) so that they produced reasonably realistic defects.

6.3.1 Isolated transverse defects

Figure 6.1 shows the results obtained from two specimens containing well separated transverse defects. The solid line depicts the mean of the envelopes obtained from specimen 1 and is identical to Figure 5.20e. A sketch of the specimen is shown in Figure 5.20a. Note that the 1.5 mm notch also contained in the specimen is not shown in Figure 6.1 because of gating in the signal processing as explained in section 5.4.5. The reflected amplitudes of the 3 mm and 5 mm deep gauge corner notches do not differ significantly, partly because of the energy loss of the incident wave at the 3 mm notch. The 5 mm notch is followed by a longer tail of additional signals. The dotted line in Figure 6.1 is the mean of the envelopes from measurements on specimen 2 which contained a single 10 mm deep gauge corner notch. In terms of rail safety such a defect would be considered critical. Its reflected amplitude is much higher than that of the two shallow notches since the defect covers a larger portion of the cross section in which the mode SS_1 is sensitive to defects, see Figure 4.9. Finally, the end-of-rail reflection in both A-scan equivalents appears as a large group of interfering signals due to complex mode conversion and waves propagating round the corner across the end face causing additional reflections. Note that the curves shown here depict only the mean of the envelopes; there are still position dependent variations of the envelopes due to the presence of multiple unwanted modes which were not fully suppressed by the spatial averaging process. The fact that the reflection of the critical 10 mm notch is far more pronounced than those of the shallow notches underlines the potential of the method as a screening tool. Since the reflected amplitude is lower than that of the end reflection, there seems to be more headroom left for the discrimination of larger defects. Note that a larger reflected amplitude can be due to deeper as well as wider defects.

6.3.2 Clusters of transverse defects

So far the considered defects were well separated and their respective reflections did not interfere. Since RCF defects usually occur in clusters, it was crucial to assess whether a critical defect could be detected in a dense cluster of non-critical shallow ones. As a first step, seven 3 mm deep transverse defects were machined into the gauge corner of rail specimen 2. The spacing of the defects was chosen to be 10 mm which is less than the wave length of 15 mm at the tone-burst centre frequency (200 kHz). The dashed line in Figure 6.2 shows the resulting A-scan equivalent of a surface wave scan covering the part of the specimen containing this cluster of

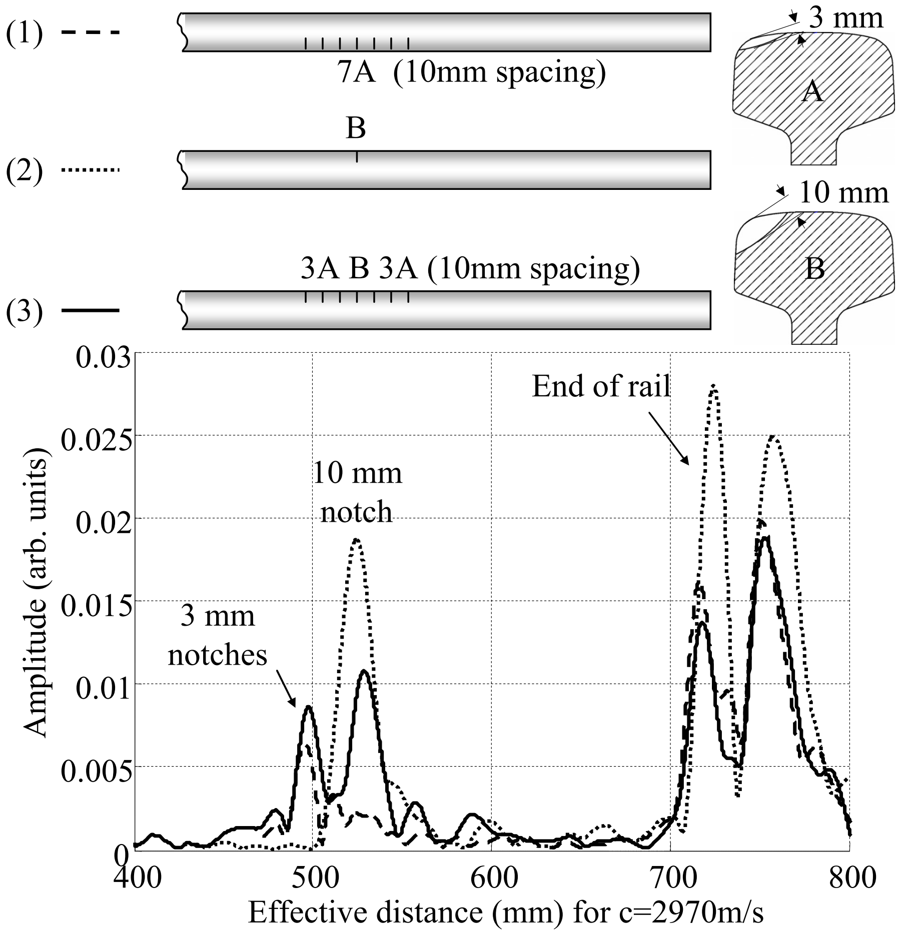

Figure 6.2: *Surface wave scan of specimen 2 with artificial defects. (1) Dashed line: cluster of seven 3 mm deep transverse notches. (2) Dotted line: single 10 mm deep transverse notch. (3) Solid line: seven transverse notches, the central one 10 mm deep, all others 3 mm.*

shallow defects. The reflection from the entry of the cluster is clearly visible and appears to be similar but slightly higher in amplitude than that of a single 3 mm deep defect, see Figure 6.1 for comparison. However, since the defect spacing is smaller than the wavelength, the individual reflections of the following defects in the cluster interfere and cannot be distinguished. This may be less of a concern for the application as a screening tool, if it is possible to detect defects within the cluster which are deeper compared to the cluster entry. To verify this, six 3 mm deep notches spaced 10 mm apart were added around the existing 10 mm notch in specimen 2 to simulate an identical cluster, but with a hidden critical defect. The dotted line in Figure 6.2 is the A-scan equivalent of the specimen with the 10 mm notch only (same as in Figure 6.1), the solid line is the A-scan equivalent after the machining of the shallow notches. The latter shows that the 10 mm deep defect in the cluster can be detected very clearly and is not masked by the preceding shallow defects. However, its amplitude is lower than in the isolated case. This is likely to be caused by multiple scattering inside the defect cluster which also affects reflections from subsequent features, see in this case the reduced amplitude of the end-of-rail-reflection. The results of this experiment were a first indication that the detection of a deep defect in a shallow cluster could be possible, but that accurate sizing would be difficult.

6.3.3 Isolated angled defects

The third specimen contained a 3 mm deep defect angled at 20° to the railhead surface, see the sketch in Figure 6.3. Its orientation and position was chosen such that its projection onto the rail cross-section would be identical to that of the vertical 3 mm notches of the other two specimens. Surface wave scans were performed in both directions on the specimen; the results are shown in Figure 6.3. In measurement set 1 (dotted line) the defect tip pointed away from the probe position, whereas in set 2 (solid line), it pointed towards the probe and thus forced the surface wave to propagate partly on a tapering wedge. The reflection in set 2 is more pronounced and has a longer signal tail compared to that of set 1. As indicated by the light and dark grey areas the respective envelopes in both sets of measurements vary significantly which again confirms the presence of multiple modes. However, the maximum of the mean of set 2 agrees well with the reflection of the transverse 3 mm notch in Figure 6.1 which matches the cross section projection of the angled notch. The reflection arrival of set 2 corresponds well to the location of the defect mouth. As opposed to this, the main reflection of set 1 has a lower amplitude and its arrival corresponds to the defect tip. Apparently, the angle of the defect is extremely shallow such that there is no significant reflection of the incident wave at the defect mouth from this direction. This kind of behaviour is in line with findings regarding Rayleigh waves which exhibit a very low reflection coefficient when reflected from

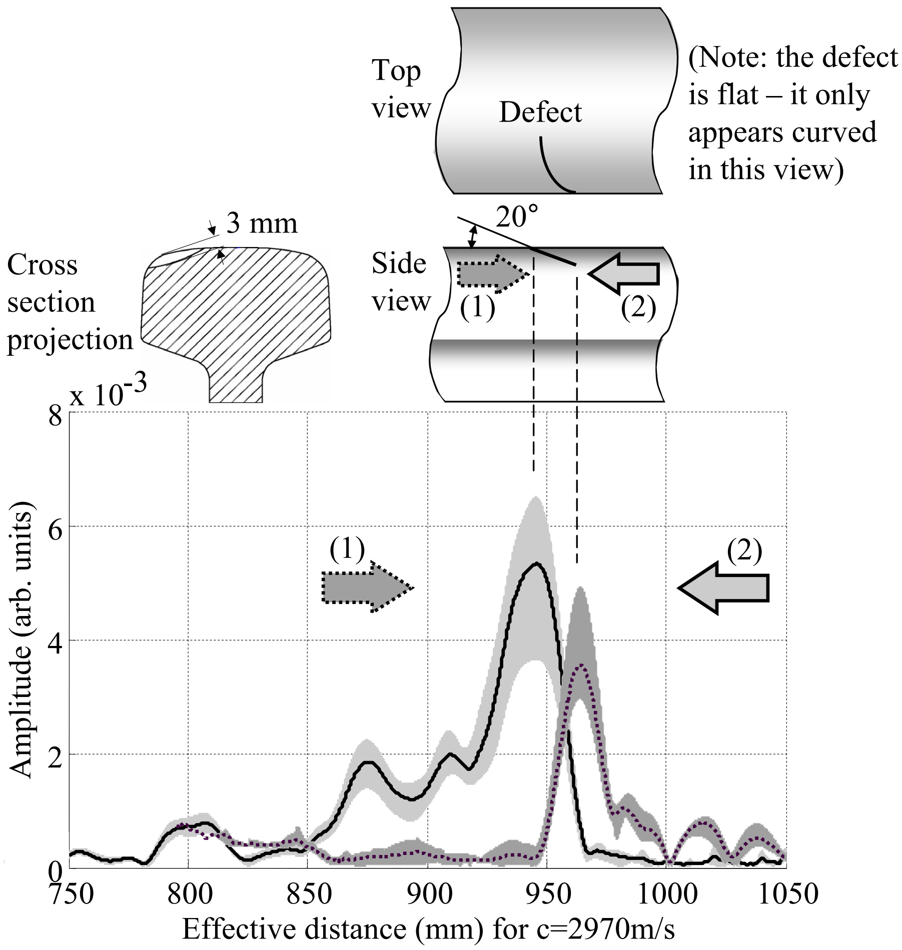

Figure 6.3: *Surface wave scan of specimen 3 with an angled defect. Solid and dotted lines denote mean of the envelopes of measurements in both directions, light and dark grey areas indicate the corresponding variation of the envelopes.*

wedge corners with wedge angles larger than 150° [53]. The difference between the two sets of measurements in our example is therefore due to the fact that for direction 1 the reflected signal is mainly caused by the defect tip and for the opposite direction mainly from the defect mouth. This implies that it is highly beneficial to perform surface wave scans in both directions in order to maximise the usable information obtained from features in the rail.

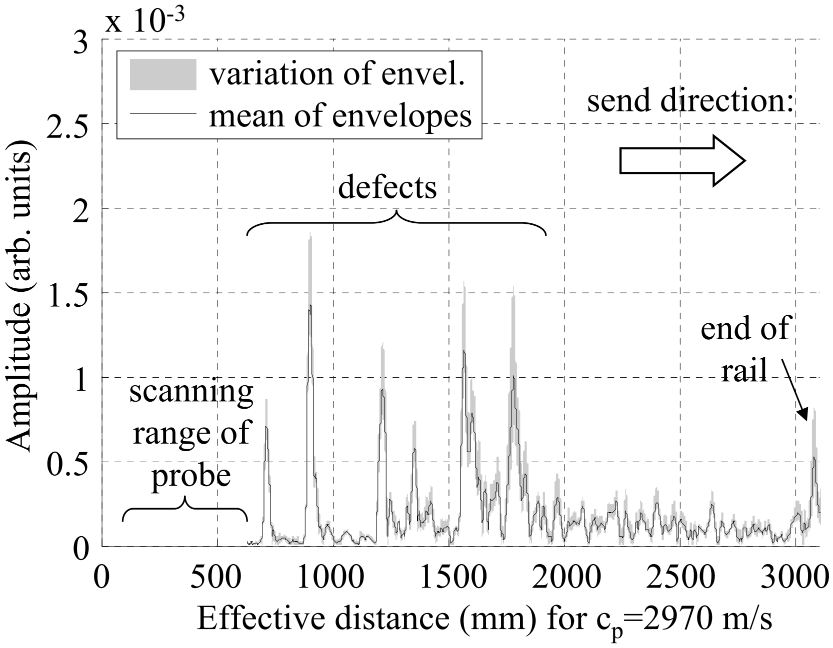

Figure 6.4: *Surface wave scan of RCF specimen I.*

6.4 Specimens containing real RCF defects

The system has also been tested on many samples of realistically damaged rail, three examples of which are presented here. For all three cases the probe setup and the signal processing are the same as discussed before. Spatial averaging was always carried out using $N = 20$ positions, a probe spacing of $x = 10$ mm and a phase velocity of $c_p = 2970$ m/s.

6.4.1 RCF specimen I

The first example was a 3 m long test specimen at ESR Technologies Ltd. (UK) which contained some isolated areas of gauge corner cracking. It was sufficient to scan the probe over a distance of only 500 mm from one end of the specimen (starting 100 mm from the end due to the probe size), since the signals were found to easily cover the remaining 2.5 m up to the other end. Figure 6.4 shows the A-scan equivalent for the whole specimen after spatial averaging over $N = 20$ positions. It was not possible to section the rail, so instead of this, the results were corre-

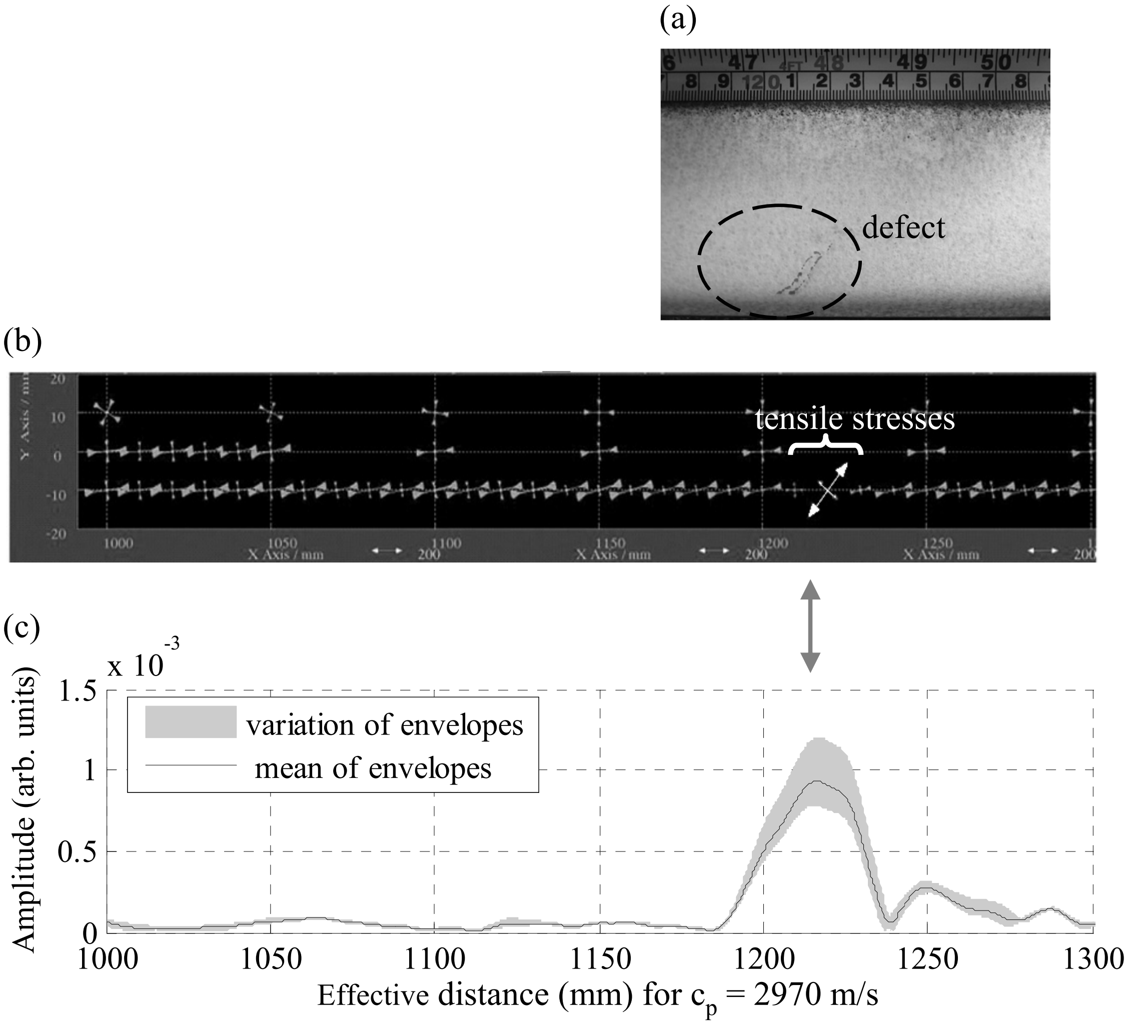

Figure 6.5: *Measurement on RCF specimen I. Comparison of (a) photograph after dye penetrant inspection; (b) MAPS stress measurement; (c) surface wave inspection using spatial averaging.*

lated with the prototype MAPS residual stress measurement method developed by ESR [129]. The defect locations indicated agree perfectly with locations of tensile stresses determined by MAPS as well as photographs after dye penetrant inspection. An example for a single defect location is shown in Figure 6.5, in which (a) is a top view photograph of the rail after dye penetrant inspection, (b) a MAPS graph and (c) the corresponding enlarged section of the surface wave A-scan equivalent taken from Figure 6.4.

6.4.2 RCF specimen II

A second example is shown in Figure 6.6. This approximately 700 mm long specimen obtained from Network Rail (UK) was tested in both directions and then sectioned. The probe was scanned in a range of 50 mm - 400 mm from both ends of the specimen. Both resulting A-scan equivalents have been combined in Figure 6.6a, thus showing all detected features in a compact way. In addition to the end reflections, the plot clearly identifies a defective area in the middle of the specimen. The top view photograph of that area (Figure 6.6b) confirms that there was obvious surface damage in that region (so-called ”squats”). However, it was not clear from visual inspection whether there were cracks underneath the dark spots or not. Figure 6.6c is an enlarged image of the defective area with indications for the two longitudinal sections taken. The enlarged surface wave A-scan in Figure 6.6f denoted by the solid line indicates defects between about 220 mm and 310 mm on the effective distance scale, but not underneath the surface damage between 320 mm and 340 mm. This is confirmed by the two sections shown in Figures 6.6d and e. The presented method has therefore correctly distinguished cracked from un-cracked areas. However, the complex defect shapes and their close spacing causes interference of reflected signals. Depending on the wave propagation direction and distance these interference patterns change, resulting for example in different envelopes for the two send directions shown in Figure 6.6f. Both the magnitude and the precise location of maxima differ slightly, see Figure 6.6f. Precise defect sizing as opposed to detection appears therefore to be difficult.

6.4.3 RCF specimen III

The third example is a 5.5 m long specimen also obtained from Network Rail, which contained large areas of severe RCF cracking and surface spalling at both ends and a seemingly defect free area in the middle. Surface wave scans were carried out on several areas on the specimen in both directions (forward and backward). Figure 6.7 shows the A-scan equivalent of a forward scan with a probe spacing of

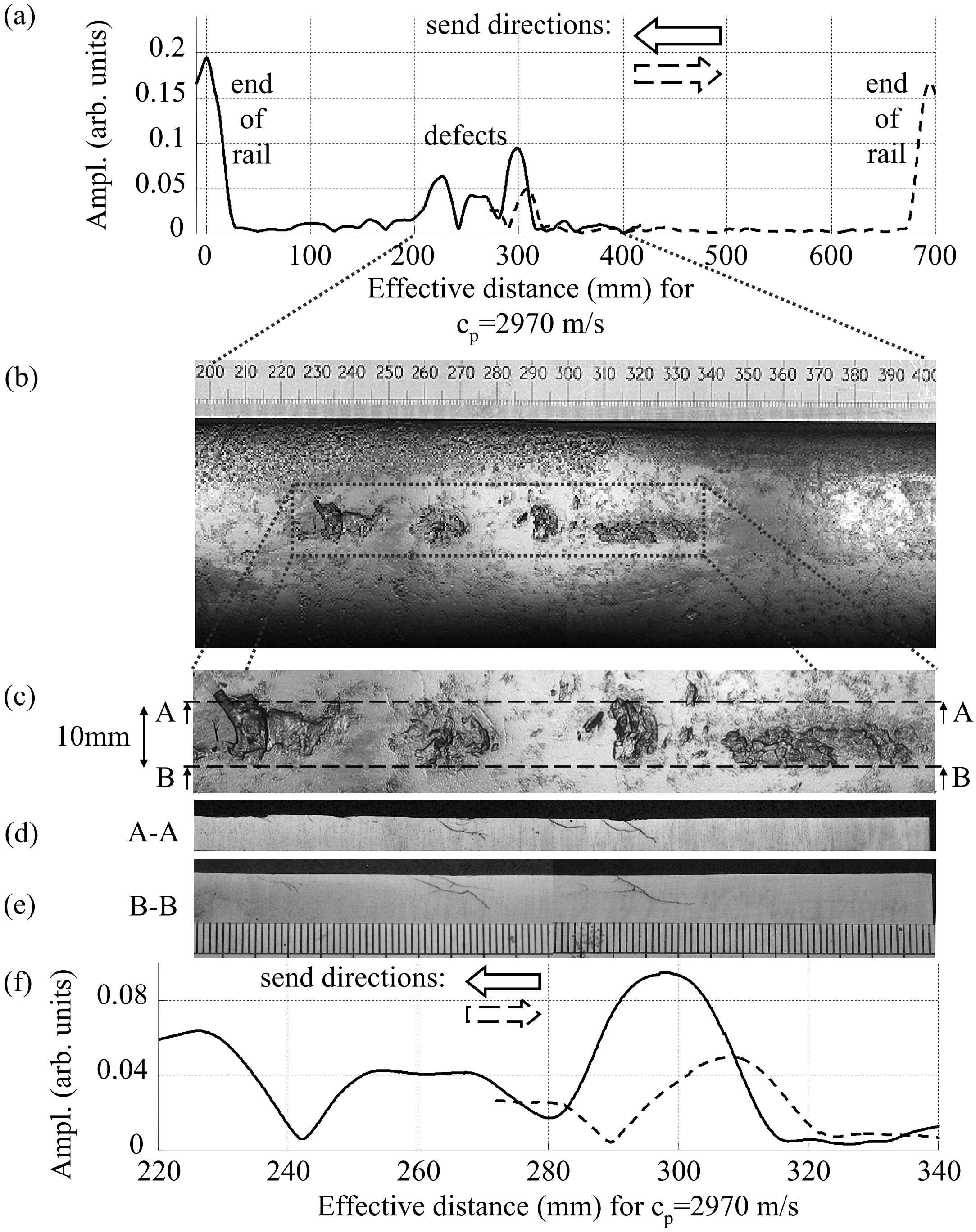

Figure 6.6: *Measurements on RCF specimen II. (a) Surface wave inspection in two directions using spatial averaging; (b) photograph of defective surface area; (c) enlarged area of Figure 6.6b with sectioning indications; (d) photograph of section A-A; (e) photograph of section B-B; (f) enlarged part of surface wave scan in Figure 6.6a on same scale as Figures 6.6c-e for comparison.*

10 mm performed between 1000-1500 mm measured from one end of the specimen. In the same way, the A-scan equivalents resulting from backward scans between 2000-2500 mm as well as 1000-1500 mm are presented in Figures 6.8 and 6.9. Note again that the measurements were only performed in these 500 mm long regions, however each set of results covered a much larger region. For a better overview the mean envelopes shown in these three graphs are presented again in a combined plot in Figure 6.10a with a sketch of the specimen in 6.10b. The first thing to notice is that the A-scans in Figures 6.7, 6.8 and 6.10a indicate two defect locations in the middle of the specimen where the surface seemed intact at first sight. Both scans consistently show a very strong reflection from an area around 1600 mm on the effective distance scale and a smaller one from a location at approximately 1350 mm. Apart from the two indicated regions there are no further reflections between about 900 and 3200 mm, see Figure 6.10a. Beyond this range there is a region at each end of the specimen with a multitude of interfering reflections which correspond to visibly defective regions with severe RCF defects and surface damage, see the specimen sketch in Figure 6.10b. Note that it is not possible to distinguish the end of rail reflection at the right end of the defective region in Figures 6.7 and 6.10a from other reflections. The rail section at this end had a very irregular shape and rough surface due to flame cutting of the specimen and therefore caused rather complex and disperse reflections. As opposed to this, the other end was sawn off and the resulting smooth surface led to a very clean pronounced reflection, see Figures 6.8-6.10a. The boundaries of the surface damage regions and the isolated defects cause the most pronounced signals and are therefore of special interest. In order to validate the measurements, three regions were cut out of the specimen for sectioning as indicated in Figure 6.10b and the findings are discussed in the following.

The first section region corresponds to the boundary of the surface damage region at one end of the specimen, see Figure 6.10b. Figure 6.11a shows a top view photograph of the region in inverted greyscale to emphasise severe RCF defects and spalling areas. Three longitudinal sections were taken with a spacing of 10 mm as indicated in Figure 6.11a, photos of these are shown in Figures 6.11b-d. An

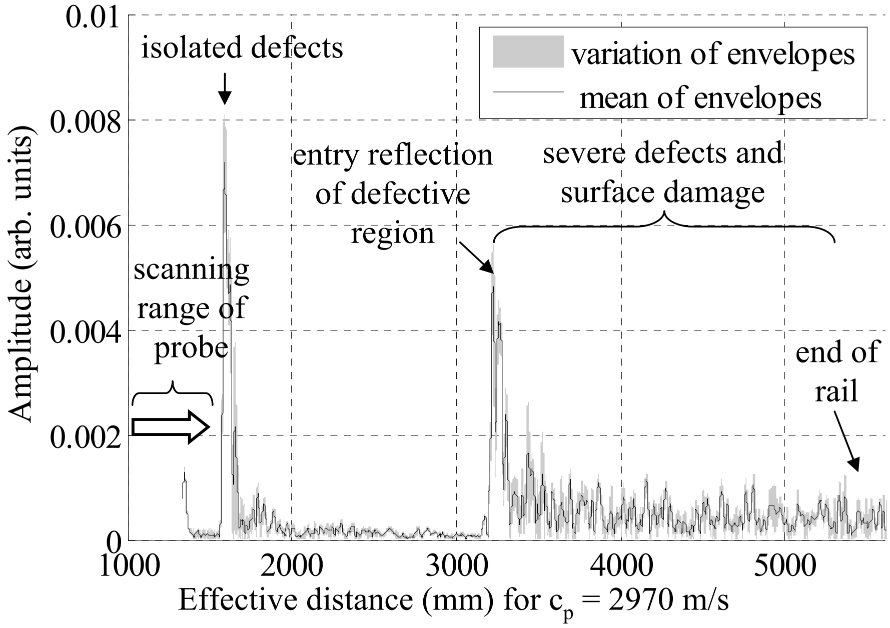

Figure 6.7: *A-scan equivalent of surface wave scan on RCF specimen III. Forward scan between 1000-1500 mm.*

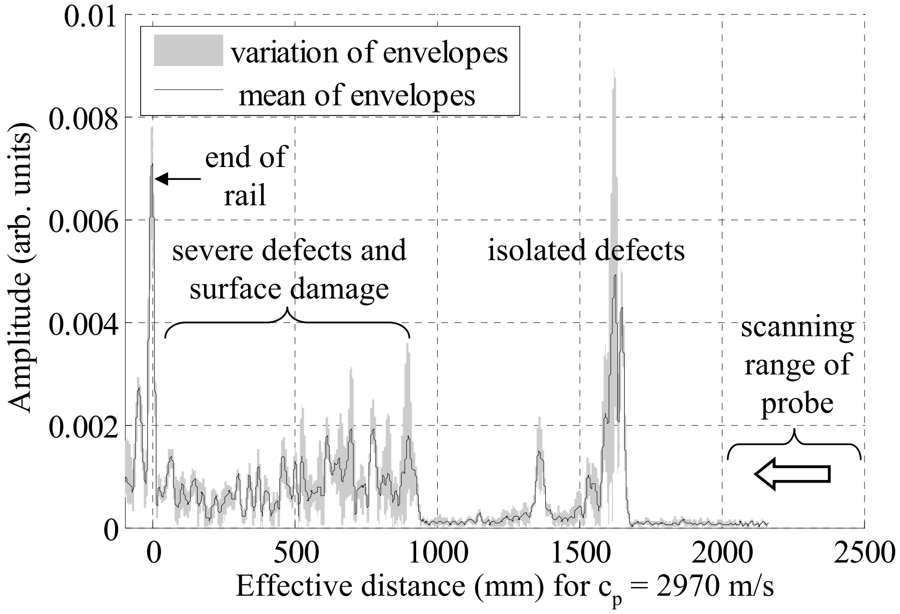

Figure 6.8: *A-scan equivalent of surface wave scan on RCF specimen III. Backward scan between 2000-2500 mm.*

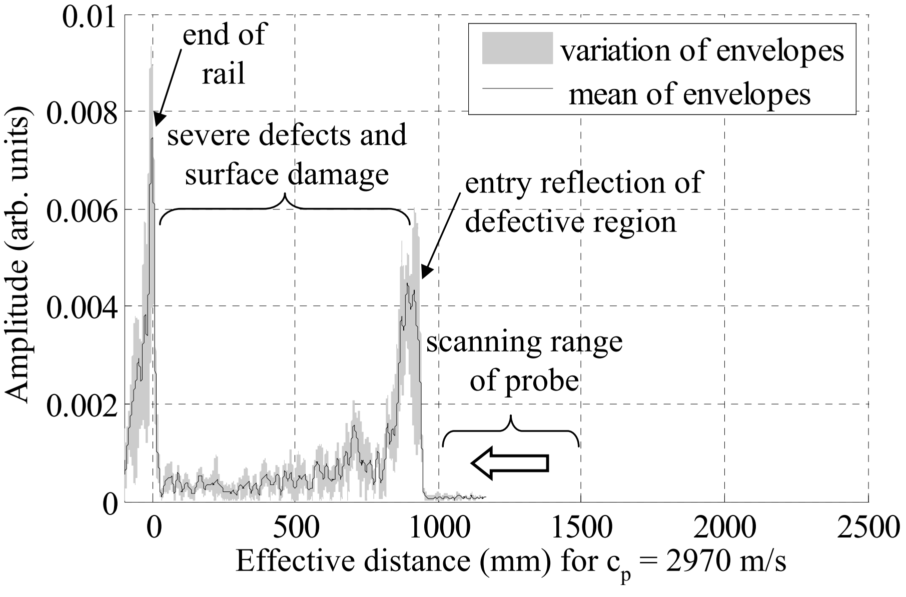

Figure 6.9: *A-scan equivalent of surface wave scan on RCF specimen III. Backward scan between 1000-1500 mm.*

enlarged section of the combined A-scan equivalents in Figure 6.10a is shown in Figure 6.11e matching the scale of the photographs. The section photographs reveal the remarkable 3-dimensional complexity of the defects: Figure 6.11b shows a very dense cluster of cracks with many branches, in Figure 6.11c many of these cracks are joined to form a single massive horizontal crack and in the third section in Figure 6.11d there are again separate angled defects. Most cracks in all three sections extend to a similar depth, many of them to more than 5 mm which means that the condition of the rail in this whole area is critical. Due to this complex and consistently dense cracking and the resulting interference of ultrasonic reflections the A-scan equivalents in Figure 6.11e (see also Figure 6.8 and 6.9) do not resolve single defects. Instead, there is a strong and relatively wide group of reflections from the boundary of the defective region (labelled "entry reflection" in Figure 6.9) and decaying reflections thereafter. This kind of reflection behaviour appears to be typical for closely spaced defect clusters since it also has been observed for artificial defects as discussed in Section 6.3.2. It applies as well to the defective region at the other end of the specimen in Figure 6.7 and 6.10a. Note however, that there is a significant difference in magnitude and shape between the two pictured A-scan equivalents in Figure 6.11e (compare also Figure 6.8 and 6.9). The solid line in

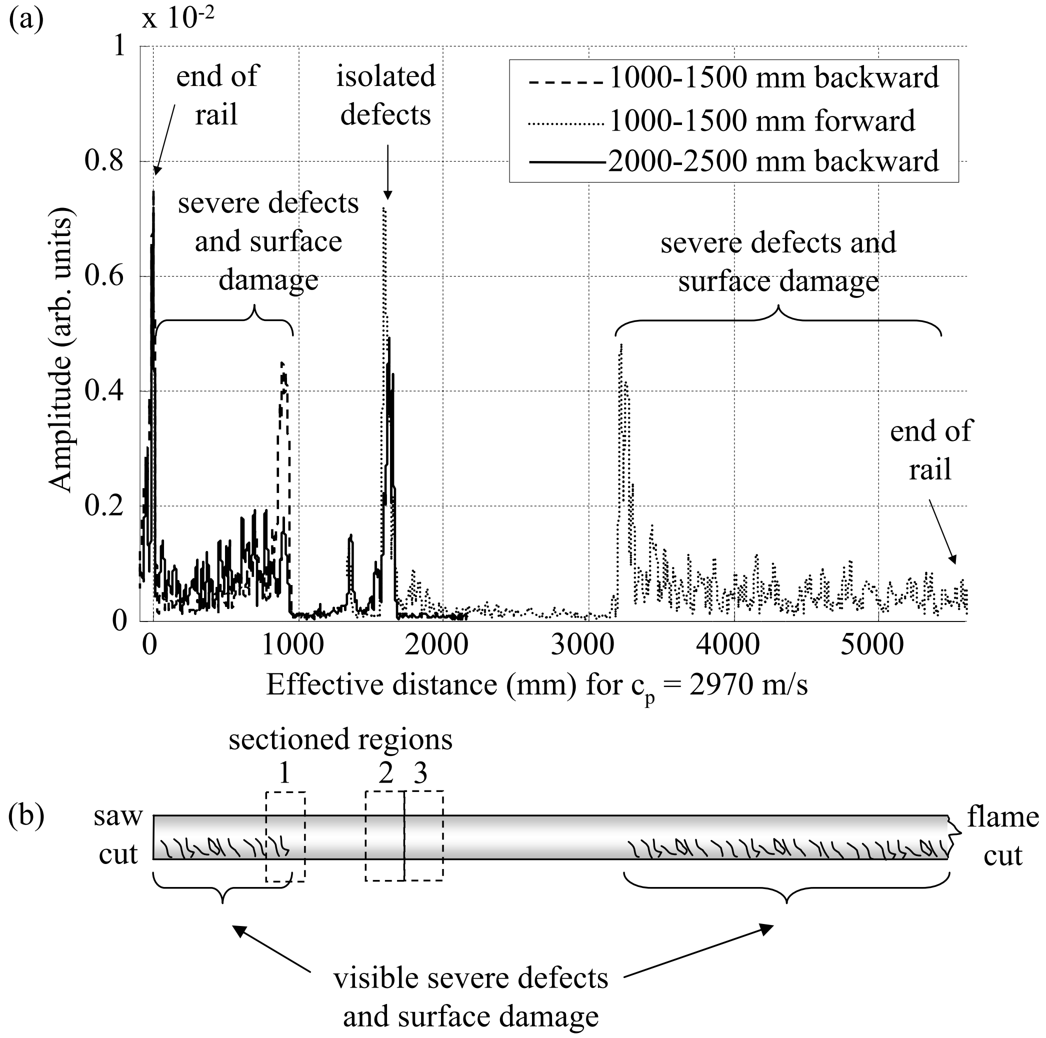

Figure 6.10: *(a) Combined surface wave A-scan equivalents (mean of the envelopes only) of three scanning regions on RCF specimen III, taken from Figures 6.7-6.9. (b) Sketch of specimen.*

Figure 6.11e exhibits a very high magnitude over a relatively wide distance at the boundary of the defective region on the right and a lower one towards the end of rail reflection on the left, see also Figure 6.9 on a different scale. In contrast to this, the dotted line (corresponding to the scan shown in Figure 6.8) remains on a more consistent level for the whole defective region. This observation can be explained again by multiple modes contained in the signal which lead to varying signals amplitudes depending on the distance between probe and defect. Furthermore, the signals corresponding to Figure 6.8 were transmitted through the isolated defects in the middle of the specimen before and after being reflected from the RCF region

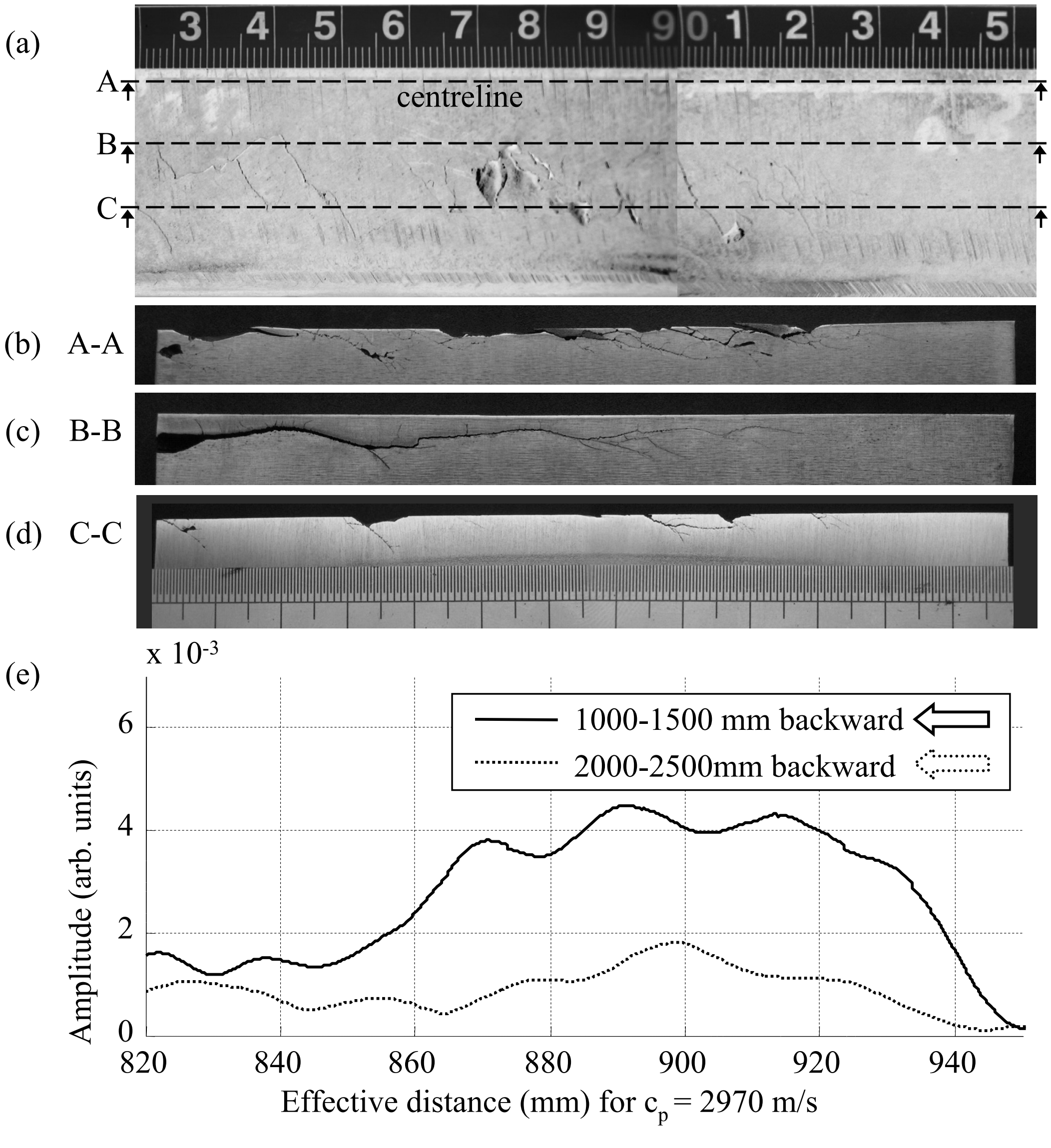

Figure 6.11: *Measurements on RCF specimen III, section region 1. (a) Photograph of defective surface area (inverted grey scale) with sectioning indications; (b) photograph of section A-A; (c) photograph of section B-B; (d) photograph of section C-C; (e) enlarged part of combined surface wave scan in Figure 6.10a on same scale as photographs for comparison.*

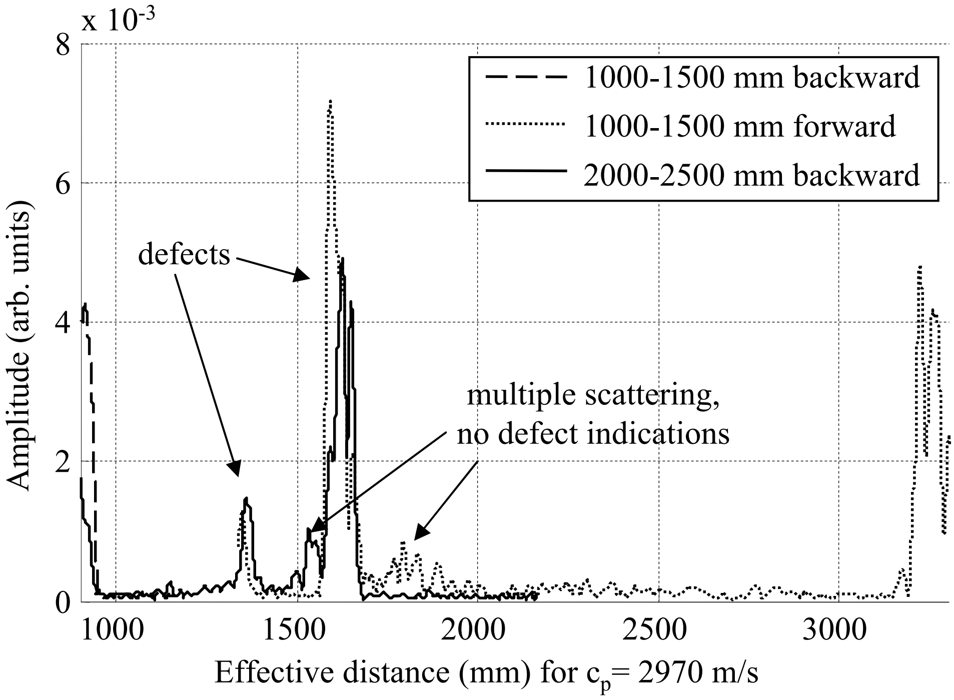

Figure 6.12: *Zoom into Figure 6.10a, combined surface wave A-scan equivalents (mean of the envelopes only) of three scanning regions on RCF specimen III.*

which has a frequency filtering effect on the signals. In addition to this, multiple scattering caused by these defects complicates the transmitted signal even further. Due to the extremely bad condition of the rail it is not surprising that the surface wave inspection method cannot deliver very detailed results. However, it can be stated that even in this worst case scenario the location of the defective area has been correctly determined and that the complexity of the received signal indicates qualitatively the damage severity.

The second and third sectioning regions are located in the range of the isolated defects as indicated in Figure 6.10. Figure 6.12 is an enlarged plot of Figure 6.10a focussing only on the region around these defects. Note that there are apparent defect indications to the right of the signal at 1600 mm for the dotted curve and to the left for the solid curve, but none in the opposite direction scans. These "ghost" indications do not correspond to defects but are caused by multiple scattering around the true defects. They occur in the signal after the reflection of an actual defect location and can therefore readily be identified when comparing the two scans in

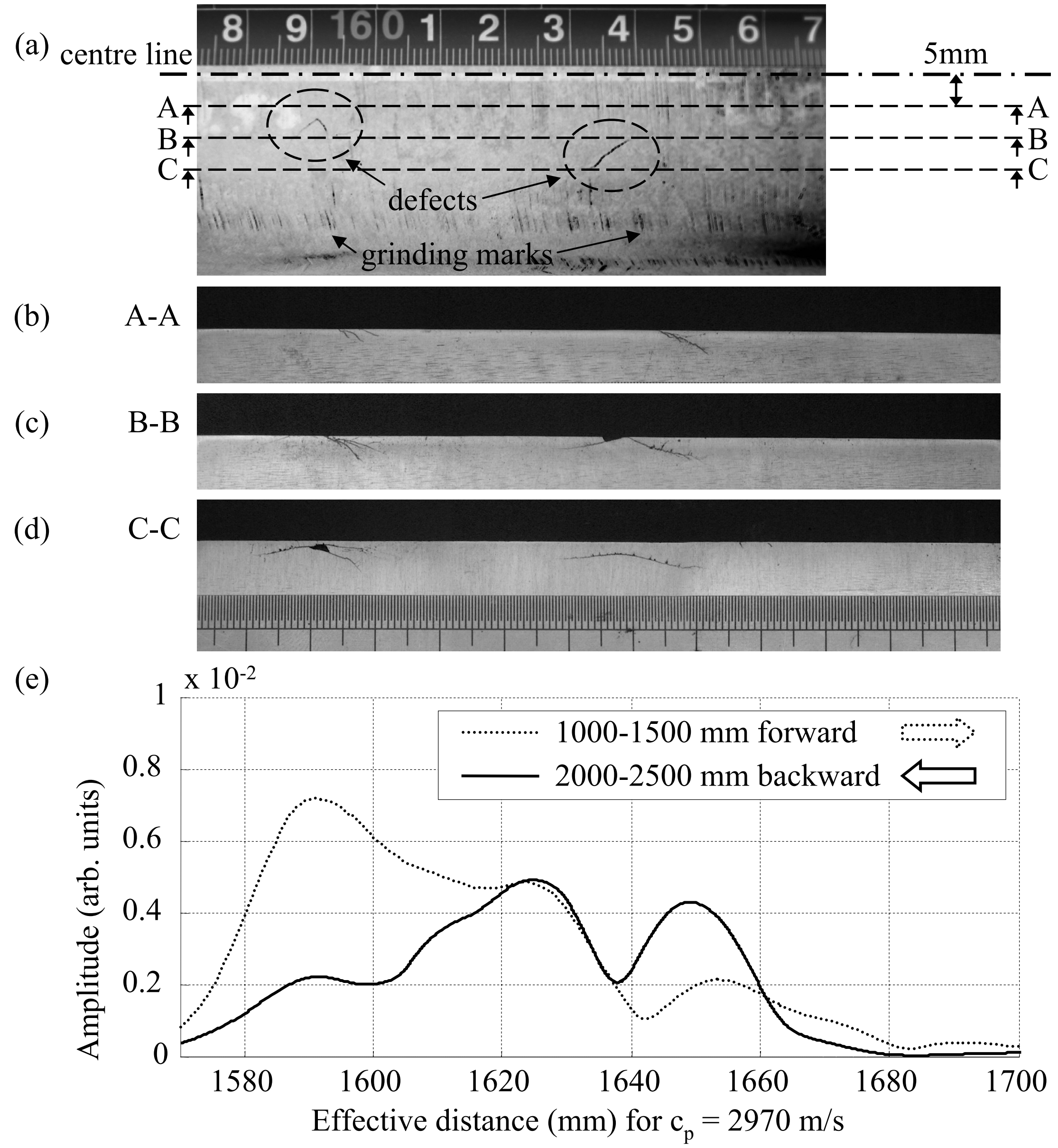

Figure 6.13: *Measurements on RCF specimen III, section region 2. (a) Photograph of defective surface area (inverted grey scale) with sectioning indications; (b) photograph of section A-A; (c) photograph of section B-B; (d) photograph of section C-C; (e) enlarged part of combined surface wave scan in Figure 6.10a on same scale as photographs for comparison.*

opposite directions shown in Figure 6.12. (Note that in practice, such "ghost" indications, i.e. reverberations which follow the directly reflected signals, could also be received from other features in the rail, e.g. block joints.) The longitudinal sections cut out of region 3 between 1700-1830 mm confirmed the absence of defects in that range. Section range 2 was chosen such that it contained the defect location around 1600 mm. The top view photograph in Figure 6.13a shows two isolated defects which were only visible under certain lighting conditions. The section photographs in Figures 6.13b-d illustrate again the 3-dimensional complexity of even such isolated defects: they exhibit different angles and a changing number of branches in the three different sections. Figure 6.13b supports the common assumption that the defects tend to grow in one direction (depending on the traffic direction), however in Figure 6.13c and d there are also branches in the opposite direction. Furthermore, the defects are only partly surface breaking; in section C-C in Figure 6.13d both defects are situated below the surface. Due to multiple scattering the cracks are not separated in the two A-scan equivalents in Figure 6.13e, but appear as one defective area. Depending on the incident wave direction, the reflected amplitude of the defect located closest to the probe appears larger than that on the other side. The magnitude of the A-scan equivalent of the isolated defects in section range 2 appears to be larger than that of the clustered defects in section range 1, however the defects are not as deep. This illustrates again that the presence of multiple modes and interfering reflections makes correct defect sizing unlikely. However, the defective region has been correctly detected with a very high accuracy, confirming the reliability of the method as a screening tool.

So far, the presented A-scan equivalents were generated based on measurements taken on more or less intact regions of the specimen surface. Figure 6.14 shows an example for which the probe was scanned over the severely damaged surface at one end of the rail. Substantial spalling and surface cracks reduced the amount of energy transmitted into the rail leading to a low signal-to-noise ratio. Furthermore, reverberations in the excitation area mask reflections from other parts of the rail such that they are hardly identifiable even with previous knowledge of feature locations based on the other scans, see Figure 6.14. However, the limited usability of such data

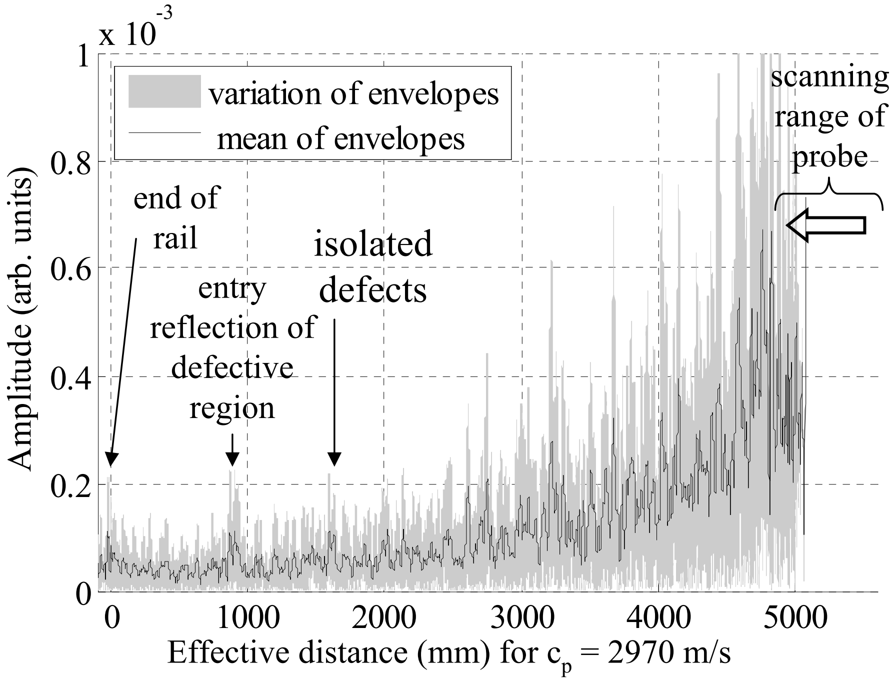

Figure 6.14: *A-scan equivalent of surface wave scan on RCF specimen III. Backward scan between 4700-5400 mm on a severely damaged surface.*

from probe locations with severe surface damage is fully compensated by the fact that there is sufficient redundancy in data obtained from other positions as seen above. Furthermore, the strong reflections and severe variations of the envelopes obtained at a severely damaged location are a good indication of the poor state of the rail surface in itself and can therefore give valuable qualitative confirmation of surface damage identified from other probe positions.

6.5 Summary

In this chapter, the developed surface wave inspection method was tested on specimens with artificial defects as well as rail containing real RCF defects.

The results from artificial transverse gauge corner defects indicated an increasing reflection with increasing defect portion of the cross-section in which the mode SS_1 is sensitive to defects. The reflection of a 10 mm deep defect was far more pronounced than those of shallower ones, and there appeared to be headroom left to distinguish even deeper defects. In a cluster of shallow defects it was possible to detect a critically deep defect. The latter was not masked by the shallow ones, however, it appeared with a lower amplitude than in the isolated case. Results from an angled defect implied that it is highly beneficial to perform surface wave scans in both directions in order to maximise the usable information obtained from features in the rail.

Tests on specimens containing real RCF defects have confirmed that the method can reliably distinguish between defective and defect-free areas. Furthermore, in areas with visible surface damage the method has proven capable to discriminate between locations with relevant defects and those with tolerable superficial damage. The signals can easily be propagated over a distance of several metres such that regions with severe surface damage, and hence reduced probe coupling, can be assessed from areas with better surface condition. However, precise sizing of real defects appears to be difficult due to the complex crack shapes and small spacing in defect clusters which lead to interfering signals. Nevertheless, certain patterns in the reflected signals could prove useful to qualitatively identify types and severity of defects, for example the presence of severe defect clusters.

Chapter 7

Conclusions

7.1 Review of thesis

In this thesis, the use of ultrasonic surface waves for rail inspection has been investigated. Currently deployed inspection systems have not proven reliable enough for the detection of rolling contact fatigue (RCF) cracks which are of growing concern for the railway industry. The aim of this project was therefore to develop a robust screening method which would reliably detect critical RCF defects in the railhead and could be integrated into moving inspection systems.

Chapter 1 of this thesis briefly reviewed types of defects found in the railhead with emphasis on those caused by RCF. The current rail inspection methods and their shortcomings were discussed and the need for a complementary inspection method identified. Some current research elsewhere into new methods was outlined which partly took place concurrently with this work. After having established the basic context, the aims for this project were formulated and surface waves were suggested as a promising candidate to address the problem.

In Chapter 2, a literature review was undertaken regarding the use of surface waves for non-destructive testing applications in general as well as more specifically for rails. Possible approaches in terms of measurement type, frequency range and transduction system were discussed and the most promising approach identified.

Chapter 3 described how the suggested approach was first tested on plates with the thickness of a railhead rather than on rails to reduce the system complexity. A simple immersion probe was developed and experiments with isolated transversal notches in thick steel plates were carried out. The experiments and additionally performed finite element (FE) simulations confirmed that the approach was promising, but also that mode control would be an issue.

For this reason, the characteristics of surface wave modes in rails were investigated in Chapter 4. No data had been published yet for guided wave modes in rails in the frequency range of interest and surface waves in particular, therefore dispersion curves and mode shapes for guided wave modes in rails were determined using a FE method. The dominant surface wave modes were extracted and a mode suitable for inspection purposes was identified. Some important properties of surface wave modes and the resulting issues were discussed. The content of Chapter 4 has been published (see [P3] in the List of Publications).

The efficient excitation and reception of the selected surface wave mode was investigated in Chapter 5. The initial plan to design a wheel probe had to be abandoned due to the severely delayed supply of the commissioned transducer array. Therefore, a sliding probe prototype containing the array was built. Two signal processing methods were investigated to improve mode selectivity: array focussing and single probe spatial averaging. An experimental procedure and signal processing routine for the surface wave rail inspection process resulted from this chapter. The investigation of the single probe spatial averaging method has been submitted for publication (see [P5] in the List of Publications).

Chapter 6 discussed the results from testing the developed inspection method on rail specimens containing artificial defects and real RCF cracks. The presented experimental results have been submitted for publication (see [P6] in the List of Publications).

The findings of this thesis will be summarised in the following section.

7.2 Summary of findings

Surface waves are highly sensitive to defects on or below the running surface of rails and allow screening of several metres of rail from a single inspection position. In order to develop a robust defect detection method it was decided to measure the signal amplitude of surface waves *reflected* from features in the rail. In contrast to transmission measurements conducted by other authors (see e.g. [18–20, 27–30]), this has the advantage that information on defect locations can be directly retrieved from the measured signal. Furthermore, amplitude changes due to changed surface condition cannot falsely be interpreted as defects.

In order to distinguish critical cracks with a depth of more than 5 mm from shallower tolerable ones, the frequency range of the surface waves needed to be chosen such that the reflected signal amplitude would increase with increasing defect depth. Based on the behaviour of Rayleigh waves on a half space, the frequency range around 250 kHz and less was found to be suitable.

A sliding local immersion probe (to be replaced in practice by a wheel probe) scanned along the rail in pulse-echo mode was utilised for signal excitation and reception. This solution was favoured over non-contact methods because of its robustness, high-signal-to-noise-ratio and possibly easier integration with existing inspection methods. However, the findings of this thesis are not restricted to this probe type and apply to other methods as well.

Mode selectivity was found to be the major issue when using low frequency surface waves. Even experimental tests on plates, being a simpler waveguide than rails, showed that a finite size surface wave probe excited a number of unwanted modes. These interfered with each other and caused signal amplitude variations of the excited and reflected signals depending on the position of the probe. Such amplitude variations complicate signal interpretation and could potentially lead to significant over- or underestimation of defect depths. It turned out that calculating the mean of the reflected signals for different probe positions was not sufficient to remove the effect of unwanted modes.

For rails, the problem of mode selectivity is even more significant. In a simple initial experiment, it was found that a large number of very similar surface wave modes is easily excitable from the top of the railhead. In order to investigate this further, the mode shapes and dispersion curves of guided wave modes in rails up to frequencies of 350 kHz for new and worn rail were determined and symmetric and antisymmetric surface wave modes were extracted. Good agreement between these and the experiment was found. It was shown that among the guided wave modes there is a symmetric surface mode well suited for inspection purposes (here named SS_1) whose non-dispersive behaviour is not affected by rail wear down to frequencies as low as 180 kHz. However, in order to develop a reliable inspection method it would be necessary to suppress the large number of similar unwanted modes.

The problem of mode control was complicated by the requirement that it should be possible to integrate the method into an moving inspection unit. Only the upper surface of the railhead would be accessible since lower parts could be obstructed by switches, fasteners etc. To optimise the excitation and reception of surface waves within this limitation, a sliding probe with a transducer array across the railhead was built and two signal processing strategies were tested.

The first approach involved focussing and apodisation of a transducer in order to match the desired mode on the running surface and compensate for the rail curvature. This turned out to be inefficient and not robust. Practical issues such as probe alignment, rail wear and transducer quality as well as finite element simulations with disappointing results led to the conclusion that mode matching across the railhead is not worth pursuing. The reason for this is that the part of the rail reasonably accessible to a moving probe is not wide enough to significantly differentiate the large number of possible surface wave modes. Instead of time consuming phased array techniques, it is sufficient to utilise a large monolithic transducer (or, as in this work, an array with all elements connected in parallel) covering the width of the railhead.

The second approach developed in this thesis to improve mode selectivity utilises the successively acquired data from scanning the probe along the rail. This single probe spatial averaging method exploits the redundancy in the signals due to the overlap of screened rail sections from several probe positions. The technique allows the mode selectivity of a scanned probe to be customised at the signal postprocessing stage and acts like a filter in the wavenumber-frequency domain. The algorithm can be interpreted as a one-dimensional SAFT algorithm and consists of phase-shifting of successively acquired waveforms to a reference position and subsequent summation. It was shown that the main effect of the spatial averaging method can be explained as a DSFT of the probe coupling represented as a spatial window. Since the mode selectivity is determined by the spatial averaging length, a higher selectivity is achieved by simply averaging over a longer distance without the need for a long transducer. Performing a 2D-FFT on the processed data has proven to be a useful tool to monitor and tune the filtering effect of the method. The spatial averaging technique is limited by uncertainties of the assumed phase velocity of the mode of interest, but appears to be robust with respect to small random probe position uncertainties. It was shown that spatial averaging over a distance of 200 mm with 10 mm probe spacing significantly reduced the level of coherent noise caused by unwanted interfering surface wave modes in rails. Complete suppression of unwanted modes was not achieved because of very similar propagation properties of some unwanted modes and uncertainties in the assumed phase velocity of the desired mode SS_1. A very compact visualization of the results was developed by combining the envelopes of the spatially averaged signals into an A-scan type plot. This clearly indicates positions of features in the wave guide and is therefore easy to interpret. In general, single probe spatial averaging has proven very efficient and robust and appears to be very useful for rail inspection as well as other applications.

The finalised inspection method, comprising the sliding probe with an array used as a wide monolithic transducer and the spatial averaging postprocessing, was tested on a number of rail specimens containing artificial defects and real RCF cracks. Sending surface waves in both directions along the rail was found to be beneficial in order to maximise the information obtained on angled cracks and identify "ghost" signals, i.e. signals which are no defect indications, but are caused e.g. by reverberations at a defect. It was shown that the complex geometry of real cracks and the interference of reflections from multiple defects leads to very complex signals such that accurate sizing does not appear to be feasible. However, it was shown that areas with cracks were reliably detected, even over a distance of several metres. Furthermore, the method has proven to reliably distinguish areas with cracks from those with tolerable shallow surface damage. Moreover, deep defects were detected even with multiple smaller ones in front. The inspection method developed in this thesis therefore appears to be very suitable for the detection of defects in the railhead, especially those originating from RCF. It could be easily integrated into existing inspections systems as a complementary method and thus enhance the reliability of rail inspection.

7.3 Future Work

7.3.1 Rail inspection system

The next step for further development of the presented rail inspection method should be the design of an inspection trolley or ”walking stick” which can be moved along the rail. It will be necessary to develop a wheel probe and an automated data acquisition system, such that the whole system can be operated at least at walking speed. In order to achieve this, the data acquisition needs to be performed on a single shot basis, rather than by summed averaging. As explained before, the main reason for performing averaging was to suppress reverberations in the relatively short specimens. This should not be an issue on longer rail sections and continuous track. Additionally, there is potential to improve the shielding and utilise balanced connections to reduce environmental noise, such that single shot data acquisition should be feasible.

As was shown in this thesis, it will not be necessary to deploy a phased transducer array; instead it would be sufficient to utilise a single large transducer inside the local immersion wheel probe. Apart from being a more robust and cost-effective solution this would also make it feasible to use a probe at frequencies lower than the current 200 kHz. It would therefore be possible to increase the penetration depth and reduce the unwanted sensitivity to very shallow defects at the surface. A crucial issue of the wheel design itself will be the damping of internal reverberations. In order to excite and receive signals at the appropriate spacing Δx for spatial averaging, there needs to be a trigger for the automated signal excitation and data acquisition system. This could for example be realised using a wheel which contains a rotary encoder (e.g. a quadrature encoder) to measure the relative probe position.

The system should then be tested both in the laboratory and on track to gain more experience with real defects and develop the signal processing further. It might for example be possible to further optimise the spatial averaging parameters for an even higher mode selectivity.

As was found in this thesis, it is beneficial to send surface waves in both directions along the rail to maximise the obtained information on angled defects and identify "ghost" signals, i.e. signals which are no defect indications, but are caused e.g. by reverberations at a defect or block joint. An interesting issue would therefore be the arrangement of either several wheel probes or two transducers in one probe to achieve coverage of both directions. With several probes it would also be possible to perform additional pitch-catch measurements along the rail. A data fusion of the pulse-echo method developed in this thesis and pitch-catch methods considered by other researchers (e.g. [18–20, 27–30]) could improve the overall reliability of the system.

The experiments presented in this thesis were carried out by step-wise manual movement of the probe. This meant that so far it was not necessary to consider potential issues and restrictions of a higher probe speed. For further development of the method involving integration into a pushed device at walking speed, i.e. about 1-2 m/s, or the implementation into an inspection train, with a possible envisaged speed around 30 m/s, inspection speed related issues need to be considered. Some of these are outlined in the following brief discussion.

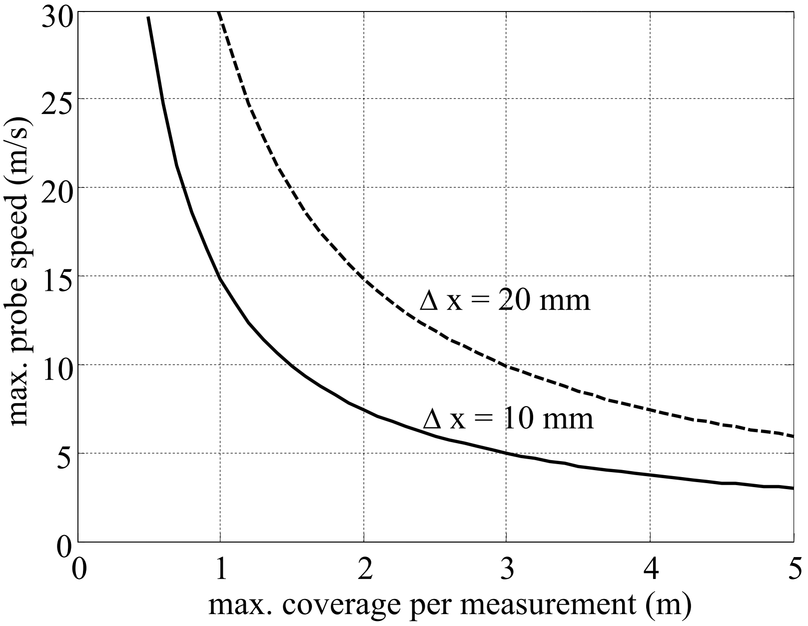

Figure 7.1: *Max. probe speed as a function of spatial averaging probe distance Δx and coverage per measurement.*

If the probe moves along the rail, then the emitted and received waves will be affected by the Doppler effect. However, even the high speed of a train-mounted probe (30 m/s) would be very low compared to the surface wave velocity, i.e. around 1%. The Doppler effect of such a system appears therefore to be negligible, especially for operation at walking speed which would be less than 0.1% of the wave velocity.

A much more important problem is the pulse repetition frequency (PRF) of the emitted signal and related issues. In the current quasi-stationary setup which was used on relatively short specimens, the PRF was chosen to be very low (in the order of 10 Hz). This allowed reverberations in the specimens to die down before the next signal was emitted. Moreover, it was possible to maximise the coverage from each measurement location, since even very small reflections which had travelled very long distances could still be identified. In a moving setup, the PRF would have to be adjusted such that signals are emitted and received according to the measurement spacing Δx required for the spatial averaging process. As was discussed before, $\Delta x = 10$ mm gave good results, it seems possible to increase that to $\Delta x = 20$ mm without too much effect of spatial aliasing. However, increasing the PRF reduces the coverage l_{max} from a single measurement position, i.e. the maximum distance a wave can travel from the probe and back before the next signal is sent. A rough estimate for the maximum possible probe speed c_{Probe} as a function of the desired measurement spacing Δx and the maximum coverage l_{max} without considering delay lines of the probe design (e.g. transducer stand-off in the probe) would be:

$$c_{Probe} = \frac{\Delta x}{2l_{max}} c_p. \tag{7.1}$$

Note that this does not take reverberations at features in the rail into account which might still interfere with subsequently emitted signals. In Figure 7.1, this relation is illustrated for the cases $\Delta x = 10$ mm and $\Delta x = 20$ mm with an assumed phase velocity of the excited mode of $c_p = 2970$ mm. It can be seen that for walking speed ($c_{Probe} \approx$ 1-2 m/s) the possible coverage is large, i.e. 5 m and more. For a train mounted probe, it would be less than a metre. As was seen in the experiments in this chapter, a coverage of 5 m can easily be realised from a single measurement position, potentially even more. This means that the real problem is to *limit* the actual wave propagation to the coverage l_{max} such that the probe speed c_{Probe} can be realised with a measurement spacing of Δx without interference of reflections from emitted and previously emitted signals.

One possibility of doing this would be to deploy a ”damping wheel” which would need to be pressed onto the rail surface and thereby would attenuate the surface wave signals at a fixed distance from the wheel probe. Another way of dealing with reflections from previous signals could be to vary Δx between the measurement positions. Since the covered distance would need to be measured anyway, e.g. by means of a wheel containing a rotary encoder, one could trigger the data acquisition either according to a fixed pattern of different Δx or even completely randomly. By applying the spatial averaging process with the correct phase shifts the unwanted reflections would be treated as incoherent noise and would be suppressed. Both these approaches should be considered for future work.

Both the maximum coverage l_{max} and the measurement spacing Δx used for spatial averaging lead to a limit of the possible inspection velocity. It is therefore crucial to explore the limits of both parameters further and find an optimum balance.

However, the issues considered here apply mainly to a very fast moving setup, i.e. a train borne system. A device operating at walking speed should not be affected by these issues and therefore appears to be relatively straightforward to realise.

7.3.2 Universal guided wave probe

The single probe spatial averaging method developed in this thesis could be used to design a universal guided wave probe. This could be useful for example for the inspection of a lot of similar components of slightly different dimensions, such as stiffeners in a bigger structure. The mode selectivity of a simple robust probe scanned along any wave guide structure could be adjusted in software without the need of changing the probe.

It could even be possible to retrieve the necessary dispersion relation of the desired mode experimentally with the same probe without the need of modelling. The probe could be scanned towards a feature in the structure and the dispersion curves could be extracted from a 2D-FFT performed on the reflected signals. This would allow instant adjustment of the mode selectivity even to structures with unknown properties.

Appendix A

FEM simulations for Rayleigh wave reflection coefficient

In order to determine the spectral reflection coefficient of pure Rayleigh waves scattered by transverse defects in steel, simulations were carried out using the finite element software FINEL/FE77 [108] and its explicit time marching solver. The models were set up by Dr Malcolm Beard [130] as the initial step of this research project. After he left to take on a position in industry, the author of this work took over from him and finished the signal analysis.

About 20 two-dimensional plain strain models assuming plane wave propagation were utilised with a sufficiently large block approximating an infinite half space, see the sketch in Figure A.1. The mesh of all models consisted of square elements with 1 mm side length to ensure a sufficient spatial resolution. The material properties for steel were assumed to be Young's modulus $E = 206$ GPa, Poisson's ratio $\nu = 0.29$ and density $\rho = 7900$ kg/m^3. Transverse defects with different depths d (in 1 mm steps between 1-20 m) were realised by disconnecting elements. Rayleigh waves (as well as shear and longitudinal waves) were excited by applying a normal force on a single node at the surface. The excitation signal was a 5 cycle tone burst centred at 200 kHz. The reflected signals were monitored at a single point at the surface as indicated in Figure A.1. The model dimensions were chosen sufficiently large such

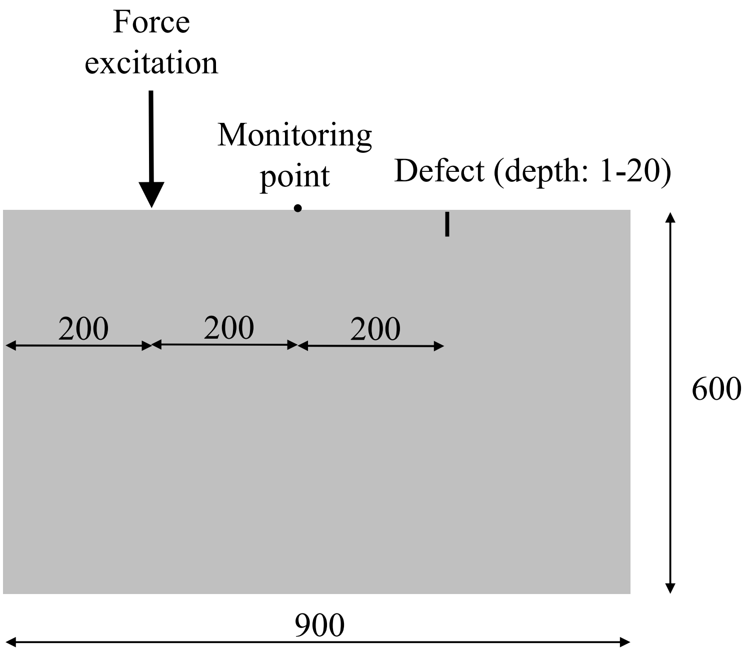

Figure A.1: *Sketch of utilised FEM models for determination of of Rayleigh wave reflection coefficient from transverse defects. All dimensions in mm.*

that different reflections were well separated. For the signal processing, the reference signal of a model without a defect was first subtracted from the signals containing defect reflections. Afterwards, the Rayleigh wave reflection from the transverse defect was identified and other signals were gated. The spectral reflection coefficient was then determined using the Fourier transformed incident and reflected Rayleigh waves (the incident wave from the model without a defect). All curves from the different models were then condensed into a single curve using spline interpolation. The result is shown in Figures 2.3, 2.4 and 3.4.

Appendix B

Simple model for the sensitivity of a wedge transducer

This appendix discusses a very simple way to assess the sensitivity of a wedge or angled probe to transmit and receive guided wave modes. As a particular variant, a local immersion probe is considered which uses a liquid (here water) as the wedge medium. Using a well known simple model we can represent the probe as a plane wave propagating in water (Amplitude $A(\omega)$, phase velocity c_w) which impinges at an angle φ on a solid surface in the interval $\left[x_{sn} - \frac{L}{2}, x_{sn} + \frac{L}{2}\right]$, see Figure B.1a. Variations of this simple probe model have also been used for other kinds of angled beam transducers and are discussed in more detail by for example Viktorov [32] and Rose [78]. The following pressure load p_n is applied on the surface at a probe

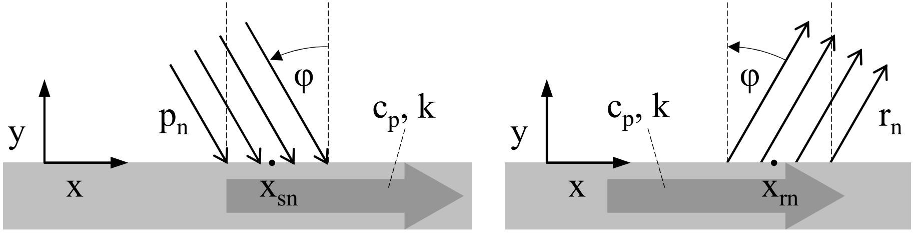

Figure B.1: *Simple model for local immersion probe: (a) send; (b) receive.*

position n:

$$p_n(\omega, x) = \begin{cases} A(\omega) \cdot e^{i\omega \frac{\sin\varphi}{c_w}(x - x_{sn})}, & \text{for } |x - x_{sn}| \leq \frac{L}{2}, \\ 0, & \text{otherwise.} \end{cases} \tag{B.1}$$

Applying a Fourier transform in the x-direction yields:

$$P_n(\omega, k) = \int_{-\infty}^{\infty} p_n(\omega, x) \cdot e^{-ikx} dx \tag{B.2}$$

$$= A(\omega) \cdot \int_{x_{sn}-\frac{L}{2}}^{x_{sn}+\frac{L}{2}} e^{i\left(\frac{\sin\varphi}{c_w}\omega(x - x_{sn}) - kx\right)} dx \tag{B.3}$$

$$= A(\omega) \cdot e^{-i\frac{\sin\varphi}{c_w}\omega x_{sn}} \cdot \frac{1}{i\left(\frac{\sin\varphi}{c_w}\omega - k\right)}$$

$$\cdot \left[e^{i\left(\frac{\sin\varphi}{c_w}\omega - k\right)\left(x_{sn}+\frac{L}{2}\right)} - e^{i\left(\frac{\sin\varphi}{c_w}\omega - k\right)\left(x_{sn}-\frac{L}{2}\right)} \right] \tag{B.4}$$

$$= 2A(\omega) \cdot e^{-i\frac{\sin\varphi}{c_w}\omega x_{sn}} \frac{\sin\left[\frac{L}{2}\left(\frac{\sin\varphi}{c_w}\omega - k\right)\right]}{\left(\frac{\sin\varphi}{c_w}\omega - k\right)} \cdot e^{i\left(\frac{\sin\varphi}{c_w}\omega - k\right)x_{sn}} \tag{B.5}$$

$$= A(\omega) \cdot B(\omega, k) \cdot e^{-ikx_{sn}}, \tag{B.6}$$

where $B(\omega, k)$ has been introduced as the transmitter sensitivity,

$$B(\omega, k) = \operatorname{sinc}\left[\frac{L}{2}\left(\frac{\sin\varphi}{c_w}\omega - k\right)\right] \cdot L, \tag{B.7}$$

and

$$\operatorname{sinc}(x) = \frac{\sin(x)}{x}. \tag{B.8}$$

The expression $B(\omega, k)$ allows us to determine the capacity of the probe to excite waves in the solid with a given wavenumber and frequency.

In the same way, we can develop a simple model for the probe acting as a receiver, see Figure B.1b. We consider a guided wave propagating in the solid at frequency ω and wavenumber k. When propagating past the immersion probe the wave applies a pressure load on the fluid in the interval $\left[x_{rn} - \frac{L}{2}, x_{rn} + \frac{L}{2}\right]$. Assuming that the probe can only detect waves radiated at an angle φ into the water, the same term $B(\omega, k)$ as above appears for the receiver sensitivity.

Appendix C

Window functions

This appendix recalls the definition and properties of the window functions used in this thesis. Given here are the equations in order to compute the window coefficients $w(n)$ for discrete windows of length N, taken from Reference [131]. The discrete notation was chosen here since the window functions were utilised with discrete signals (both in space and time).

- *Hanning (or Hann) window*

$$w(n+1) = 0.5 - 0.5\cos\left(2\pi\frac{n}{N-1}\right), \qquad n = 0, 1, \ldots, N-1 \tag{C.1}$$

- *Hamming window*

$$w(n+1) = 0.54 - 0.46\cos\left(2\pi\frac{n}{N-1}\right), \qquad n = 0, 1, \ldots, N-1 \tag{C.2}$$

Both window functions are shown in Figure C.1 in comparison with a rectangular window for $N = 100$. Note that only the Hanning window starts and ends with the value 0. Figure C.2 shows the magnitude of the Fourier transformed window functions in the frequency domain. The Hamming window has a slightly narrower main lobe and an about 14 dB lower first sidelobe than the Hanning window. All its side lobes are below -40 dB and decay slowly with increasing frequency, whereas those of the Hanning window decay more rapidly. For certain applications (such as

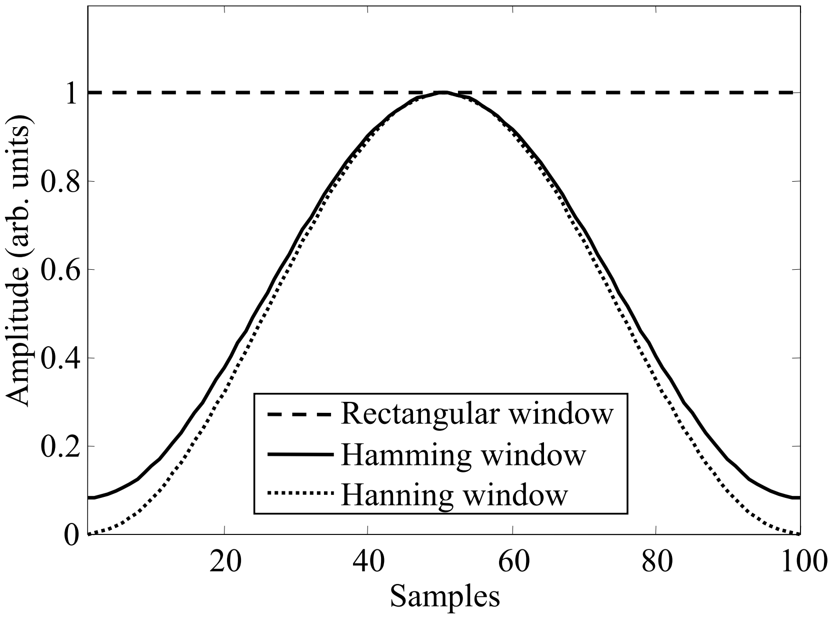

Figure C.1: *Comparison of rectangular, Hamming and Hanning window.*

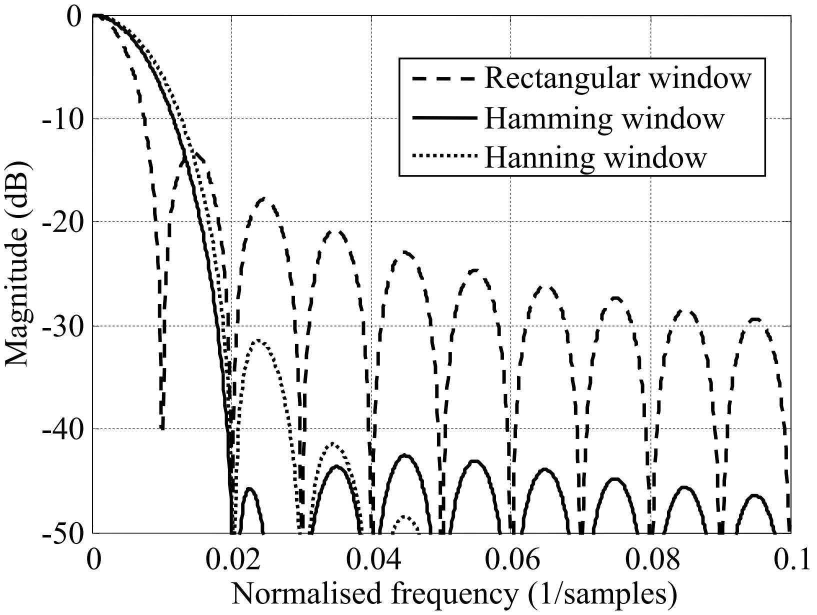

Figure C.2: *Comparison of rectangular, Hamming and Hanning window in the frequency domain.*

apodisation in conjunction with the spatial averaging method, see Section 5.4.3), the low level of sidelobes close to the main lobe is advantageous; in such cases the Hamming window performs better than the Hanning window.

References

[1] D. F. Cannon, K.-O. Edel, S. L. Grassie, and K. Sawley. Rail defects: an overview. *Fatigue Fract Engng Mater Struct*, 26:865–887, 2003.

[2] S. L. Grassie and J. Kalousek. Rolling contact fatigue of rails: characteristics, causes and treatments. In *Proceedings of 6th International Heavy Haul Conference*, pages 381–404, Cape Town, South Africa, 1997.

[3] U. Zerbst, K. Mädler, and H. Hintze. Fracture mechanics in railway applications – an overview. *Engineering Fracture Mechanics*, 72:163–194, 2005.

[4] M. L. Peterson, B. D. Jeffrey, and R. M. Gutkowski. Limitations in size and type of detectable defects in rail flaw inspection. *Insight*, 42(5):306–311, 2000.

[5] K. Sawley and R. Reiff. *Rail Failure Assessment for the Office of the Rail Regulator, UK. An assessment of Railtrack's methods for managing broken and defective rails.* Technical Report P-00-070, Transportation Technology Center, Inc., Pueblo, Colorado, USA, 2000.

[6] R. Pohl, A. Erhard, H.-J. Montag, H.-M. Thomas, and H. Wüstenberg. NDT techniques for railroad wheel and gauge corner inspection. *NDT & E International*, 37:89–94, 2004.

[7] S. L. Grassie. Rolling contact fatigue on the British railway system: treatment. *Wear*, 258:1310–1318, 2005.

[8] G. H. Cope, editor. *British Railway Track. Design, Construction and Maintenance.* The Permanent Way Institution, 6th edition, 1993.

[9] J. Jaiswal. Rail defects & rail steels. In S. L. Grassie and S. Iwnicki, editors, *Third course on vehicle/track interaction*, pages 13–27. VTI Course, JR Solutions, Cambridge, UK, 2001.

[10] G. Thomson and J. Jaiswal. Rolling contact fatigue – a practical track based study. In S. L. Grassie and S. Iwnicki, editors, *Fourth course on vehicle/track interaction*, pages 239–256. VTI Course, JR Solutions, Cambridge, UK, 2002.

[11] R. A. Smith. The wheel-rail interface – some recent accidents. *Fatigue Fract Engng Mater Struct*, 26:901–907, 2003.

[12] Office of Rail Regulation, UK. Train derailment at Hatfield: A Final Report by the Independent Investigation Board, 2006. Available from http://www.rail-reg.gov.uk.

[13] Health & Safety Executive, UK. Train derailment at Hatfield - 17 October 2000, Second HSE Interim report, January 2001.

[14] R. Clark. Rail flaw detection: overview and needs for future developments. *NDT & E International*, 37:111–118, 2004.

[15] G. Pearson. Personal communication, 2006. National Rail Engineer at Network Rail.

[16] J. McNamara and F. Lanza di Scalea. Air coupled ultrasonic testing of railroad rails. *Materials Evaluation*, 60(12):1431–1437, 2002.

[17] F. Lanza di Scalea and J. McNamara. Ultrasonic NDE of railroad tracks: air-coupled cross-sectional inspection and long-range inspection. *Insight*, 45(6):394–401, 2003.

[18] S. Kenderian, B. B. Djordjevic, and R. E. Green. Sensitivity of point- and line-source laser-generated acoustic wave to surface flaws. *IEEE Trans. Ultrason., Ferroelect., Freq. Contr.*, 50(8):1057–1064, 2003.

[19] S. Kenderian, B. B. Djordjevic, D. Cerniglia, and G. Garcia. Dynamic railroad inspection using the laser-air hybrid ultrasonic technique. *Insight*, 48(6):336–341, 2006.

[20] R. S. Edwards, S. Dixon, and X. Jian. Characterisation of defects in the railhead using ultrasonic surface waves. *NDT & E International*, 39:468–475, 2006.

[21] S.-C. Wooh and J. Wang. Laser ultrasonic detection of rail defects. In D. O. Thompson and D. E. Chimenti, editors, *Review of Progress in Quantitative NDE*, volume 21, pages 1819–1826. American Institute of Physics, Melville, New York, 2002.

[22] S.-C. Wooh, J. Wang, and Q. Zhou. Photoacoustic detection of rail discontinuities. *Materials Evaluation*, 60(5):645–650, 2002.

[23] P. Wilcox, B. Pavlakovic, M. Evans, K. Vine, P. Cawley, M. J. S. Lowe, and D. N. Alleyne. Long range inspection of rail using guided waves. In D. O. Thompson and D. E. Chimenti, editors, *Review of Progress in Quantitative NDE*, volume 22A, pages 236–243. American Institute of Physics, Melville, New York, 2003.

[24] J. L. Rose, M. J. Avioli, P. Mudge, and R. Sanderson. Guided wave inspection potential of defects in rail. *NDT & E International*, 37:153–161, 2004.

[25] I. Bartoli, F. Lanza di Scalea, M. Fateh, and E. Viola. Modeling guided wave propagation with application to the long-range defect detection in railroad tracks. *NDT & E International*, 38(5):325–334, 2005.

[26] G. Zumpano and M. Meo. A new damage detection technique based on wave propagation for rails. *International Journal of Solids and Structures*, 43(5):1023–1046, 2006.

[27] P. R. Armitage. The use of low-frequency Rayleigh waves to detect gauge corner cracking in railway lines. *Insight*, 44(6):369–372, 2002.

[28] S. Kenderian, D. Cerniglia, B. B. Djordjevic, G. Garcia, J. Sun, and M. Snell. Rail track field testing using laser/air hybrid ultrasonic technique. *Materials Evaluation*, 61(10):1129–1133, 2003.

[29] F. Lanza di Scalea, P. Rizzo, S. Coccia, I. Bartoli, M. Fateh, E. Viola, and G. Pascale. Non-contact ultrasonic inspection of rails and signal processing for automatic defect detection and classification. *Insight*, 47(6):346–353, 2005.

[30] R. S. Edwards, A. Sophian, S. Dixon, G.-Y. Tian, and X. Jian. Dual EMAT and PEC non-contact probe: applications to defect testing. *NDT & E International*, 39:45–52, 2006.

[31] Lord Rayleigh. On waves propagated along the plane surfaces of an elastic solid. *Proc. London Math. Soc.*, 17:4–11, 1885.

[32] I. A. Viktorov. *Rayleigh and Lamb waves: Physical theory and applications.* Plenum Press, New York, 1967.

[33] V. Domarkas, B. T. Khuri-Yakub, and G. S. Kino. Length and depth resonances of surface cracks and their use for crack size estimation. *Appl. Phys. Lett.*, 33(7):557–559, 1978.

[34] K. G. Hall. Crack depth measurement in rail steel by Rayleigh waves aided by photoelastic visualisation. *Non-Destructive Testing*, 9(3):121–126, 1976.

[35] B. Masserey and E. Mazza. Analysis of the near-field ultrasonic scattering at a surface crack. *J. Acoust. Soc. Am.*, 118(6):3585–3594, 2005.

[36] P. E. Lagasse. Higher-order finite-element analysis of topographic guides supporting elastic surface waves. *J. Acoust. Soc. Am.*, 53(4):1116–1122, 1973.

[37] A. A. Oliner. Waveguides for acoustic surface waves: a review. *Proc. IEEE*, 64(5):615–627, 1976.

[38] A. A. Oliner. *Acoustic surface waves*, volume 24 of *Topics in applied physics.* Springer-Verlag, Berlin Heidelberg, 1978.

[39] V. V. Krylov. Rayleigh waves on smooth surfaces of arbitrary shape. *Sov. Phys. Acoust.*, 25(5):425–428, 1979.

[40] V. V. Krylov. Distinctive characteristics of guided surface-wave propagation in complex topographic structures. *Sov. Phys. Acoust.*, 33(4):407–411, 1987.

[41] H.-S. Tuan and R. C. M. Li. Rayleigh-wave reflection from groove and step discontinuities. *J. Acoust. Soc. Am.*, 55(6):1212–1217, 1974.

[42] D. A. Simons. Reflection of Rayleigh waves by strips, grooves, and periodic arrays of strips or grooves. *J. Acoust. Soc. Am.*, 63(5):1292–1301, 1978.

[43] D. A. Mendelsohn, J. D. Achenbach, and L. M. Keer. Scattering of elastic waves by a surface-breaking crack. *Wave Motion*, 2:277–292, 1980.

[44] Y. C. Angel and J. D. Achenbach. Reflection and transmission of obliquely incident Rayleigh waves by a surface-breaking crack. *J. Acoust. Soc. Am.*, 75(2):313–319, 1984.

[45] D. W. Fitting and L. Adler. Frequency dependent interaction of ultrasonic waves with surface breaking cracks. In P. Höller, editor, *New Procedures in Nondestructive Testing*, pages 203–212, Saarbrücken, 1983. Springer-Verlag.

[46] R. Dong and L. Adler. Measurement of reflection and transmission coefficients of Rayleigh waves from cracks. *J. Acoust. Soc. Am.*, 76(6):1761–1763, 1984.

[47] B. Q. Vu and V. K. Kinra. Diffraction of Rayleigh waves in a half-space. I. Normal edge crack. *J. Acoust. Soc. Am.*, 77(4):1425–1430, 1985.

[48] V. K. Kinra and B. Q. Vu. Diffraction of Rayleigh waves in a half-space. II. Inclined edge crack. *J. Acoust. Soc. Am.*, 79(6):1688–1692, 1986.

[49] S. Zh. Zharylkapov and V. V. Krylov. Scattering of Rayleigh waves by a groove of arbitary depth. *Sov. Phys. Acoust.*, 33(5):509–511, 1987.

[50] A. Klein and H. J. Salzburger. Characterization of surface defects by Rayleigh waves. In P. Höller, editor, *New Procedures in Nondestructive Testing*, pages 193–202, Saarbrücken, 1983. Springer-Verlag.

[51] B. A. Auld, S. Ayter, and M. Tan. Theory of scattering of Rayleigh waves by surface breaking cracks. In *IEEE Ultrasonics Symposium*, pages 384– 390, 1978.

[52] K. Fujii, S. Takeuchi, Y. Okano, and M. Nakano. Rayleigh wave scattering at various wedge corners. *Bulletin of the Seismological Society of America*, 74(1):41–60, 1984.

[53] K. Fujii. Rayleigh wave scattering at various wedge corners: investigation in the wider range of wedge angles.

[54] V. V. Krylov and V. G. Mozhaev. Reflection and transmission of Rayleigh waves in a wedge. *Sov. Phys. Acoust.*, 31(6):457–459, 1985.

[55] V. M. Babich, V. A. Borovikov, L. Ju. Fradkin, V. Kamotski, and B. A. Samokish. Scatter of Rayleigh waves by tilted surface-breaking cracks. *NDT & E International*, 37:105–109, 2004.

[56] M. Hirao, H. Fukuoka, and Y. Miura. Scattering of Rayleigh surface waves by edge cracks: Numerical simulation and experiment. *J. Acoust. Soc. Am.*, 72(2), 1982.

[57] L. J. Bond. A computer model of the interaction of acoustic surface waves with discontinuities. *Ultrasonics*, 17:71–77, 1979.

[58] G. A. Georgiou and L. J. Bond. Studies in ultrasonic wave-defect interaction. In *4th International Offshore Mechanics and Arctic Engineering Symposium*, volume 2, pages 451–460, 1985.

[59] G. A. Georgiou and L. J. Bond. Quantitative studies in ultrasonic wave-defect interaction. *Ultrasonics*, 25:328–334, 1987.

[60] R. J. Blake and L. J. Bond. Rayleigh wave scattering from surface features: wedges and down-steps. *Ultrasonics*, 28:214–228, 1990.

[61] R. J. Blake and L. J. Bond. Rayleigh wave scattering from surface features: up-steps and troughs. *Ultrasonics*, 30(4):255–265, 1992.

[62] W. Hassan and W. Veronesi. Finite element analysis of Rayleigh wave interaction with finite-size, surface-breaking cracks. *Ultrasonics*, 41:41–52, 2003.

[63] C. Pecorari. Scattering of a Rayleigh wave by a surface-breaking crack with faces in partial contact. *Wave Motion*, 33:259–270, 2001.

[64] J.-Y. Kim and S. I. Rokhlin. Surface acoustic wave measurements of small fatigue cracks initiated from a surface cavity. *International Journal of Solids and Structures*, 39:1487–1504, 2002.

[65] D. A. Cook and Y. H. Berthelot. Detection of small surface breaking fatigue cracks in steel using scattering of Rayleigh waves. *NDT & E International*, 34:483–492, 2001.

[66] Ch. Zhang and J. D. Achenbach. Dispersion and attenuation of surface waves due to distributed surface-breaking cracks. *J. Acoust. Soc. Am.*, 88(4):1986–1992, 1990.

[67] C. Pecorari. Rayleigh wave dispersion due to a distribution of semi-elliptical surface-breaking cracks. *J. Acoust. Soc. Am.*, 103(3):1383–1387, 1998.

[68] C. Pecorari. Attenuation and dispersion of Rayleigh waves propagating on a cracked surface: an effective field approach. *Ultrasonics*, 38:754–760, 2000.

[69] C. Pecorari. On the effect of a residual stress field on the dispersion of a Rayleigh wave propagating on a cracked surface. *J. Acoust. Soc. Am.*, 103(1):616–617, 1998.

[70] D. M. Egle and D. E. Bray. Measurement of acoustoelastic and third-order elastic constants for rail steel. *J. Acoust. Soc. Am.*, 60(3):741–744, 1976.

[71] D. E. Bray, M. E. Davis, and L. Reiter. Rayleigh wave dispersion in the cold-worked layer of used railroad rail. *J. Acoust. Soc. Am.*, 64(3):845–851, 1978.

[72] M. Hirao, M. Kyukawa, Y. Sotani, and H. Fukuoka. Rayleigh wave propagation in a solid with a cold-worked surface layer. *Journal of Nondestructive Evaluation*, 2(1):43–49, 1981.

[73] D. S. Grewal. Improved ultrasonic testing of railroad rail for transverse discontinuities in the rail head using higher order Rayleigh (M_{21}) waves. *Materials Evaluation*, 54(9):983–986, 1996.

[74] S. Dixon and S. B. Palmer. Wideband low frequency generation and detection of Lamb and Rayleigh waves using electromagnetic acoustic transducers (EMATs). *Ultrasonics*, 42:1129–1136, 2004.

[75] S. Dixon, R. S. Edwards, and X. Jian. Inspection of rail track head surfaces using electromagnetic transducers (EMATs). *Insight*, 46(6):326–330, 2004.

[76] B. A. Auld. *Acoustic fields and waves in solids*, volume 2. Robert E. Krieger, Malabar, Florida, 2 edition, 1990.

[77] G. S. Kino. *Acoustic waves.* Prentice-Hall, 1987.

[78] J. L. Rose. *Ultrasonic Waves in Solid Media.* Cambridge University Press, Cambridge, UK, 1999.

[79] B. W. Ti, W. D. O'Brien, Jr., and J. G. Harris. Measurement of coupled Rayleigh wave propagation in an elastic plate. *J. Acoust. Soc. Am.*, 102(3):1528–1531, 1997.

[80] A. Folguera and J. G. Harris. Coupled Rayleigh surface waves in a slowly varying elastic waveguide. *Phil. Trans. R. Soc. Lond. A*, pages 1 – 16, 1996.

[81] B. N. Pavlakovic, M. J. S. Lowe, D. N. Alleyne, and P. Cawley. Disperse: A general purpose program for creating dispersion curves. In D. O. Thompson and D. E. Chimenti, editors, *Review of Progress in Quantitative NDE*, volume 16, pages 185–192. American Institute of Physics, Melville, New York, 1997.

[82] D. N. Alleyne and P. Cawley. The interaction of Lamb waves with defects. *IEEE Trans. Ultrason., Ferroelect., Freq. Contr.*, 39(3):381–397, 1992.

[83] Precision Acoustics, Ltd. NPL Absorbing Lining for Ultrasonic Test Tanks, 2003. webpage: http://www.acoustics.co.uk/aptflexf28.htm, accessed 21/11/2003.

[84] A. D. Poularikas and S. Seely. *Signals and Systems.* PWS-KENT, Boston, 2. edition, 1991.

[85] B. Pavlakovic. *Leaky Guided Ultrasonic Waves in NDT.* PhD thesis, Imperial College of Science, Technology and Medicine, London, UK, 1998.

[86] D. N. Alleyne and P. Cawley. Optimization of Lamb wave inspection techniques. *NDT & E International*, 25:11–22, 1992.

[87] D. N. Alleyne and P. Cawley. A two-dimensional Fourier transform method for the measurement of propagating multimode signals. *J. Acoust. Soc. Am.*, 89(3):1159–1168, 1991.

[88] G. F. Miller and H. Pursey. The field and radiation impedance of mechanical radiators on the free surface of a semi-infinite isotropic solid. *Proceedings of the Royal Society of London. Series A, Mathematical and Physical Sciences*, 223(1155):521–541, 1954.

[89] P. Wilcox, M. Evans, O. Diligent, M. Lowe, and P. Cawley. Dispersion and excitability of guided acoustic waves in isotropic beams with arbitrary cross section. In D. O. Thompson and D. E. Chimenti, editors, *Review of Progress in Quantitative NDE*, volume 21A, pages 203–210. American Institute of Physics, Melville, New York, 2002.

[90] L. Pochhammer. Ueber die Fortpflanzungsgeschwindigkeiten kleiner Schwingungen in einem unbegrenzten isotropen Kreiscylinder. *J. Rein. Angew. Math.*, 81:324–336, 1876.

[91] K. Sato. Elastic wave propagation in an infinite bar of elliptical cross section. *Bull. JSME*, 21(152):203–209, 1978.

[92] R. D. Mindlin and E. A. Fox. Vibrations and waves in elastic bars of rectangular cross section. *J. Appl. Mech.*, 27:152–158, 1966.

[93] G. Rosenfeld and J. B. Keller. Wave propagation in elastic rods of arbitrary cross section. *J. Acoust. Soc. Am.*, 55(3):555–561, 1974.

[94] J. A. Morrison. Propagation of high frequency surface waves along cylinders of general cross section. *J. Math. Phys.*, 16(9):1786–1794, 1975.

[95] L. O. Wilson and J. A. Morrison. Propagation of high frequency elastic surface waves along cylinders of general cross section. *J. Math. Phys.*, 16(9):1795–1805, 1975.

[96] J. A. Morrison. High frequency approximations for elastic surface waves propagating along cylinders of general cross section. *J. Math. Phys.*, 17(6):958–963, 1976.

[97] N. J. Nigro. Steady-State Wave Propagation in Infinite Bars of Noncircular Cross Section. *J. Acoust. Soc. Am.*, 40(6):1501–1508, 1966.

[98] W. B. Fraser. Stress wave propagation in rectangular bars. *Int. J. Solids Structures*, 5:379–397, 1969.

[99] W. B. Fraser. Dispersion of elastic waves in elliptical bars. *J. Sound Vib.*, 10(2):247–260, 1969.

[100] K. Nagaya. Stress wave propagation in a bar of arbitrary cross section. *J. Appl. Mech.*, 49:157–163, 1982.

[101] A. Gunawan and S. Hirose. Boundary element analysis of guided waves in a bar with arbitrary cross-section. *Eng. Anal. Bound. Elem.*, 29(10):913–924, 2005.

[102] L. Gavrić. Computation of propagative waves in free rail using a finite element technique. *J. Sound Vib.*, 185(3):531–543, 1995.

[103] L. Gry. Dynamic modelling of railway track based on wave propagation. *J. Sound Vib.*, 195(3):477–505, 1996.

[104] T. Hayashi, W.-J. Song, and J. L. Rose. Guided wave dispersion curves for a bar with an arbitrary cross-section, a rod and rail example. *Ultrasonics*, 41:175–183, 2003.

[105] T. Hayashi, C. Tamayama, and M. Morimasa. Wave structure analysis of guided waves in a bar with an arbitrary cross-section. *Ultrasonics*, 44:17–24, 2006.

[106] V. Damljanović and R. L. Weaver. Propagating and evanescent elastic waves in cylindrical waveguides of arbitrary cross section. *J. Acoust. Soc. Am.*, 115(4):1572–1581, 2004.

[107] I. Bartoli, A. Marzani, F. Lanza di Scalea, and E. Viola. Modeling wave propagation in damped waveguides of arbitrary cross-section. *J. Sound Vib.*, 295(3-5):685–707, 2006.

[108] D. Hitchings. *FE77 User Manual.* Imperial College of Science, Technology and Medicine, London, 1994.

[109] Railtrack plc, UK. Railtrack Line Specification. Track Maintenance Requirements. RT/CE/S/104, June 2000.

[110] P. Wilcox, M. J. S. Lowe, and P. Cawley. The excitation and detection of Lamb waves with planar coil electromagnetic acoustic transducers. *IEEE Trans. Ultrason., Ferroelect., Freq. Contr.*, 52(12):2370–2383, 2005.

[111] B. A. Auld. *Acoustic fields and waves in solids*, volume 1. Robert E. Krieger, Malabar, Florida, 2 edition, 1990.

[112] D. N. Alleyne. *The nondestructive testing of plates using ultrasonic Lamb waves.* PhD thesis, Imperial College of Science, Technology and Medicine, 1991. http://www.imperial.ac.uk/ndt/public/publications/theses.htm.

[113] B. Pavlakovic, D. Alleyne, P. Cawley, and M. J. S. Lowe. Simulation of Lamb wave propagation using pure mode excitation. In D. O. Thompson and D. E. Chimenti, editors, *Review of Progress in Quantitative NDE*, volume 17, pages 1003–1010. American Institute of Physics, Melville, New York, 1998.

[114] R. J. Hallermeier and O. I. Diachok. Simple technique for exciting and probing elastic surface waves. *J. Appl. Phys.*, 41(12):4763–4764, 1970.

[115] H. L. Bertoni and T. Tamir. Characteristics of wedge transducers for acoustic surface waves. *IEEE Trans. Son. Ultrason.*, SU-22(6):415–420, 1975.

[116] W. Zhu and J. L. Rose. Lamb wave generation and reception with time-delay periodic arrays: A BEM simulation and experimental study. *IEEE Trans. Ultrason., Ferroelect., Freq. Contr.*, 46(3):654–664, 1999.

[117] S.-C. Wooh and Y. Shi. Synthetic phase tuning of guided waves. *IEEE Trans. Ultrason., Ferroelect., Freq. Contr.*, 48(1):209–223, 2001.

[118] J. Li and J. L. Rose. Implementing guided wave mode control by use of a phased transducer array. *IEEE Trans. Ultrason., Ferroelect., Freq. Contr.*, 48(3):761–768, 2001.

[119] J. Banchet, R. Sicard, A. Chahbaz, and J. Goyette. Phased array for guided waves and crack detection for airframe structures. In D. O. Thompson and D. E. Chimenti, editors, *Review of Progress in Quantitative NDE*, volume 23A, pages 826–833. American Institute of Physics, Melville, New York, 2004.

[120] P. Cawley, M. J. S. Lowe, D. N. Alleyne, B. Pavlakovic, and P. Wilcox. Practical long range guided wave testing: Applications to pipes and rail. *Materials Evaluation*, 61(1):66–74, 2003.

[121] P. Cawley. Practical long range guided wave inspection - managing complexity. In D. O. Thompson and D. E. Chimenti, editors, *Review of Progress in Quantitative NDE*, volume 22, pages 22–37. American Institute of Physics, Melville, New York, 2003.

[122] B. W. Drinkwater and P. Cawley. An ultrasonic wheel probe alternative to liquid coupling. *Insight*, 36(6):430–433, 1994.

[123] ABAQUS. *ABAQUS - Analysis User's Manual. Version 6.5.* 2004.

[124] R. Y. Chiao and L. J. Thomas. Analytic evaluation of sampled aperture ultrasonic imaging techniques for NDE. *IEEE Trans. Ultrason., Ferroelect., Freq. Contr.*, 41(4):484–493, 1994.

[125] M. Karaman, P.-C. Li, and M. O'Donnel. Synthetic aperture imaging for small scale systems. *IEEE Trans. Ultrason., Ferroelect., Freq. Contr.*, 42(3):429–442, 1995.

[126] R. Sicard, A. Chahbaz, and J. Goyette. Guided Lamb waves and L-SAFT processing technique for enhanced detection and imaging of corrosion defects in plates with small depth-to-wavelength ratio. *IEEE Trans. Ultrason., Ferroelect., Freq. Contr.*, 51(10):1287–1297, 2004.

[127] C. Holmes, B. W. Drinkwater, and P. D. Wilcox. Post-processing of ultrasonic phased array data for optimal performance. *Insight*, 47(2):88–90, 2005.

[128] J. Davies, F. Simonetti, M.J.S Lowe, and P. Cawley. Review of synthetically focused guided wave imaging techniques with application to defect sizing. In D. O. Thompson and D. E. Chimenti, editors, *Review of Progress in Quantitative NDE*, volume 25, pages 142–149. American Institute of Physics, Melville, New York, 2006.

[129] D. J. Buttle, W. Dalzell, and P. J. Thayer. Early warnings of the onset of rolling contact fatigue by inspecting the residual stress environment of the railhead. *Insight*, 46(6):344–348, 2004.

[130] M. Beard. Personal communication. 2002, while he was Research Associate at Imperial College London.

[131] A. V. Oppenheim and R.W Schafer. *Discrete-Time Signal Processing.* Prentice-Hall, 1989.

List of Publications

[P1] D. Hesse and P. Cawley. The potential of ultrasonic surface waves for rail inspection. In D. O. Thompson and D. E. Chimenti, editors, *Review of Progress in Quantitative NDE*, volume 24, pages 227–234. American Institute of Physics, Melville, New York, 2005.

[P2] D. Hesse and P. Cawley. Excitation of surface wave modes in rails and their application for defect detection. In D. O. Thompson and D. E. Chimenti, editors, *Review of Progress in Quantitative NDE*, volume 25, pages 1593–1600. American Institute of Physics, Melville, New York, 2006.

[P3] D. Hesse and P. Cawley. Surface wave modes in rails. *J. Acoust. Soc. Am.*, 120(2):733–740, 2006.

[P4] D. Hesse and P. Cawley. Detection of critical defects in rails using ultrasonic surface waves. In D. O. Thompson and D. E. Chimenti, editors, *Review of Progress in Quantitative NDE*, volume 26, American Institute of Physics, Melville, New York, 2007, in press.

[P5] D. Hesse and P. Cawley. A single probe spatial averaging technique for guided waves and its application to surface wave rail inspection. Submitted to *IEEE Transactions on Ultrasonics, Ferroelectrics, and Frequency Control*, August 2006.

[P6] D. Hesse and P. Cawley. Defect detection in rails using ultrasonic surface waves. Submitted to *Insight*, October 2006.